Droplet Dynamics on Polydimethylsiloxane Brushes

Dissertation

Zur Erlangung des Grades

“Doktor der Naturwissenschaften”

am Fachbereich Chemie, Pharmazie und Geowissenschaften

der Johannes Gutenberg-Universität Mainz

Shuai Li

Geboren in Shijiazhuang, P.R. China

on the recommendation of Prof. Dr. Hans-Jürgen Butt, MPIP

Mainz, 2023

Die vorliegende Arbeit wurde im Zeitraum von September 2019 bis Mai 2023 am Max-Planck-Institut für Polymerforschung in Mainz im Arbeitskreis von Prof. Dr. [redacted] angefertigt.

Tag der Prüfung:

1. Berichterstatter: Prof. Dr. [redacted]

2. Berichterstatter: Prof. Dr. [redacted]

Dissertation an der Universität Mainz (D77)

Abstract

Surfaces with super liquid-repellency properties are critical in many industrial and domestic applications because of their low lateral adhesion towards water, ice, snow, and microorganisms. Attributed to their excellent liquid repellency, superhydrophobic surfaces and lubricant-infused surfaces (where lubricant liquid is infused into texted substrates) have attracted considerable attention over the past few decades. As an alternative, polymer brushes, which consists of one-end-fixed polymer chains on substrate, are also demonstrated to have low sliding angles. Due to the non-fluorinated and more liquid-like characteristics, polydimethylsiloxane (PDMS) brushes is one promising type of polymer brushes among others, e.g. perfluoropolyether brushes and alkyl brushes. This thesis describes droplet dynamics on PDMS brushes and its potential applications in water harvesting, anti-icing, droplet manipulation, condensation heat transfer, and slide electrification.

First, I describe a novel strategy to reduce the water/ice lateral adhesion on PDMS brushes by introducing organic vapor, e.g. toluene vapor, in the surrounding environment. The vapor makes PDMS brushes polymer chains more liquid-like thus it exhibits lower sliding angles for water droplets. The evidence of such flexible layer is obtained using atomic force microscopy. The condensation experiments in the presence of toluene vapor shows the greatly reduced departure droplet sizes, at which sizes water droplets start to slide on the vertically oriented surface. The significantly increased water collection rate indicates its strong potential in the water harvesting applications. Further measurements show that the vapor lubrication can also be used for droplet manipulation and anti-icing applications.

To explain the mechanism for vapor lubrication, I conduct contact angle measurements on three different hydrophobic surfaces (including PDMS brushes) in different vapor environment (n-hexane, toluene, cyclohexane, air, dimethyl sulfoxide, tetrahydrofuran, and ethanol). In water-

soluble vapors, a substantial decrease is observed in contact angles (θ). The contact angles are explained well by Young's equation, $\cos\theta = (\gamma_{SV} - \gamma_{SL}) / \gamma_{LV}$, where γ_{SV}, γ_{SL}, γ_{LV} denotes the solid-vapor, solid-liquid, and liquid-vapor interfacial surface tension. The decrease of θ is attributed to the vapor induced change in the interfacial tensions. However, the low contact angle hysteresis (difference between advancing and receding contact angle) on PDMS surfaces in saturated n-hexane and toluene vapor cannot be explained by Young's equation. The observation supports the hypothesis that these vapors adsorb into the PDMS and form a lubricating layer.

Next, I investigate the condensation heat transfer performance on PDMS brushes by using ethanol-water mixtures. The purpose of the mixture is to optimize the surface tension and latent heat of vaporization. On PDMS brushes, all mixtures show a low contact angle hysteresis of less than 10°. So it is highly possible that condensate will form discrete droplets (dropwise condensation) instead of a covering liquid film (filmwise condensation) on the surface. The condensation measurements in microscale show that the droplet nucleation and growth are substantially enhanced by mixing water and ethanol. The further heat transfer measurements show that the thermal performance is greatly enhanced by more than one order of magnitude when compared to heat transfer coefficient of filmwise condensation. The transition from dropwise to filmwise condensation is also successfully delayed when compared to that on fluorinated surface.

It is well known that water droplets running down a hydrophobic surface become positively charged and leave behind a negative surface charge. Finally, I study this spontaneous charge separation on lubricant-infused PDMS brushes by measuring the charge of continues water drops sliding over the surface. On a fluorinated hydrophobic surface or PDMS brushes the charge per drop decreases with the increased drop number. However, on lubricant-infused PDMS brushes, the charge per drop starts from 0, then it increases. After reaching a maximum value, the charge per drop decreases before reaches a stable value. Such interesting phenomenon is due to the

depletion process of the lubricant on the surface, where the surface conductivity is changed during this process. The investigation here provides a fundamental understanding of drop charge on lubricant-infused surfaces. I hope this may contribute to the applications in the further step.

The projects highlighted the significant role of droplet dynamics and polydimethylsiloxane brushes surface in applications such as anti-icing, drop manipulation and condensation heat transfer.

Zusammenfassung

Superhydrophobe Oberflächen kommen in vielen industriellen und täglichen Anwendungen zum Einsatz. Grund hierfür ist ihre geringe Seitliche Adhäsion gegenüber Wasser, Eis, Schnee, Mikroorganismen, etc. Aufgrund ihrer ausgezeichneten flüssigkeitsabweisenden Eigenschaften haben superhydrophobe Oberflächen und lubricant-infused Oberflächen (bei denen eine Gleitmittelflüssigkeit in texturierte Substrate eingebracht wird) in den letzten Jahrzehnten große Aufmerksamkeit auf sich gezogen. Eine Alternative sind Polymerbürsten, die aus an einem Ende fixierten Polymerketten auf einem Substrat bestehen und nachweislich einen geringen Gleitwinkel aufweisen. Aufgrund ihrer nicht fluorierten und eher flüssigkeitsähnlichen Eigenschaften sind Bürsten aus Polydimethylsiloxan- Bürsten (PDMS- Bürsten) eine vielversprechende Art von Polymer-Bürsten neben anderen, z. B. Perfluorpolyether-Bürsten und Alkyl-Bürsten.Diese Arbeit beschreibt wie sich Flüssigkeitstropfen auf PDMS-Bürsten bewegen und potentielle Anwendungen in den Bereichen Wassergewinnung, Vereisungsschutz, Tropfenmanipulation, Kondensations-Wärmeübertragung und Elektrifizierung von Folien.

Zunächst beschreibe ich eine neuartige Strategie zur Verringerung der Wasser/Eis-Seitenhaftung auf PDMS-Bürsten. Diese gelingt durch organischen Lösemittel-Dampf in der Umgebung, z.B. Toluol-Dampf. Der Dampf verändert die Flexibilität der Polymerketten der PDMS-Bürsten. Dadurch können sich Wassertropfen leichter bewegn und gleiten bereits bei geringer Neigung der Oberfläche ab. Mit der Hilfe der Rasterkraft-Mikroskopie können diese Veränderung der PDMS-Bürsten untersucht werden. Die Kondensationsexperimente in Gegenwart von Toluol-Dampf zeigen, dass die Größe der ablaufenden Wasser-Tröpfchen stark reduziert und die Wassersammelrate deutlich erhöht wird. Weitere Messungen zeigen, dass die „Dampfschmierung“ auch für die Tropfen-Manipulation und *anti-icing*-Anwendungen genutzt werden kann.

Um den Mechanismus der Dampfschmierung zu erklären, habe ich Kontaktwinkelmessungen an drei verschiedenen Oberflächen (einschließlich PDMS-Bürsten) in verschiedenen Dampfumgebungen (n-Hexan, Toluol, Cyclohexan, Luft, Dimethylsulfoxid, Tetrahydrofuran und Ethanol) durchgeführt. In wasserlöslichen Dämpfen konnte ich Abnahme des Kontaktwinkels (θ) beobachtet. Die Kontaktwinkel lassen sich gut mit der Youngschen Gleichung $\cos \theta = (\gamma_{SV} - \gamma_{SL}) / \gamma_{LV}$, erklären, wobei γ_{SV}, γ_{SL}, γ_{LV} die Grenzflächenspannung Fest-Dampf, Fest-Flüssig und Flüssigkeit-Dampf bezeichnen. Die Abnahme von θ ist auf die dampfinduzierte Änderung der Grenzflächenspannungen zurückzuführen.Diese Abnahme lässt sich durch eine dampfinduzierte Änderung der Grenzflächenspannungen erklären. Die sehr geringe Kontaktwinkelhysterese (Unterschied zwischen fortschreitendem und zurückweichendem Kontaktwinkel) auf PDMS-Oberflächen in gesättigtem n-Hexan- und Toluol-Dämpfen kann jedoch nicht durch eine Änderung der Grenzflächenspannungen erklärt werden. Diese Beobachtung stützt die Hypothese, dass diese Dämpfe durch die PDMS-Bürsten adsorbiert werden und so eine Gleitschicht bilden.

Als Nächstes untersuche ich die Leistung der Kondensationswärmeübertragung auf Oberflächen, die mit PDMS-Bürsten beschichtet waren. Dabei verwendete ich ein Ethanol-Wasser-Gemisch, um Oberflächenspannung und latente Verdampfungswärme zu optimieren. Auf PDMS-Bürsten weisen alle Mischungen eine geringe Kontaktwinkelhysterese von weniger als 10° auf. Es ist also gut möglich, dass das Kondensat auf der Oberfläche diskrete Tröpfchen (tropfenweise Kondensation) statt eines deckenden Flüssigkeitsfilms (filmweise Kondensation) bildet. Die Kondensationsmessungen im Mikromaßstab zeigen, dass die Keimbildung und das Wachstum der Tropfen durch das Mischen von Wasser und Ethanol deutlich verbessert werden kann. Die Wärmeübertragungsmessungen zeigen, dass die thermische Leistung im Vergleich zum Wärmeübertragungskoeffizienten der filmweisen Kondensation um mehr als eine Größenordnung verbessert wird. Der Übergang von der tropfenweisen zur filmweisen Kondensation wird im Vergleich zur fluorierten Oberfläche ebenfalls erfolgreich verzögert.

Es ist bekannt, dass Wassertropfen, die eine hydrophobe Oberfläche herablaufen, sich positiv aufladen und eine negative Oberflächenladung zurücklassen. Diese spontane Ladungstrennung habe ich an Oberflächen untersucht, die mit PDMS-Bürsten beschichtet und mit einem Öl infiltriert waren (*lubricant-infused* PDMS-Bürsten). Normalerweise nimmt bei einer Serie von Tropfen die Ladung der Tropfen mit zunehmender Tropfenzahl ab. Auf den *lubricant-infused* PDMS-Bürsten beginnt die Ladung bei 0 und nimmt dann mit steigender Tropfenzahl zu. Nach Erreichen eines Höchstwertes nimmt die Ladung der Tropfen wieder ab, bis die Tropfenladung sättigt. Dieses Phänomen führe ich auf eine Verarmung des Öls zurückzuführen. Während dieses Prozesses ändert sich die Oberfläche-Leitfähigkeit. Die hier durchgeführten Untersuchungen liefern ein grundlegendes Verständnis der Tropfenladung auf *lubricant-infused* PDMS-Bürsten.

Die Projekte haben die bedeutende Rolle der Tropfendynamik und der Polydimethylsiloxan-Bürsten in Anwendungen wie Vereisungsschutz, Tropfenmanipulation und Kondensations-Wärmeübertragung aufgezeigt.

Table of Contents

Abstract I

Zusammenfassung V

Table of Contents IX

1. Introduction 1

2. Fundamentals 5

2.1 Contact Angle Phenomena on Surfaces 5

2.1.1 Equilibrium Contact Angle 5

2.1.2 Advancing/Receding Contact Angles 7

2.2 Superhydrophobic surfaces 8

2.2.1 Preparation Methods 9

2.2.2 Applications 10

2.3 Lubricant-Infused Surfaces 12

2.3.1 Preparation Methods 13

2.3.2 Applications 14

2.4 PDMS brushes 15

2.4.1 Preparation Methods 15

2.4.2 Applications 17

3. Vapor Lubrication for Reducing Water and Ice Adhesion on PDMS Brushes[§] 19

3.1 Introduction 20

3.2 Experimental 22

3.3 Results and Discussion 25

3.4 Conclusions 34

3.5 Appendix I 35

4. Organic Vapors Influence Water Contact Angles on Hydrophobic Surfaces[§] 41

4.1 Introduction 42

4.2 Results and Discussion 44
4.3 Conclusion.....51
4.4 Appendix II 52
5. Enhanced Condensation Heat Transfer of Binary Liquids on PDMS Brushes[§] 59
5.1 Introduction.....60
5.2 Experimental 62
5.3 Results and Discussion 64
5.4 Conclusions.....75
5.5 Appendix III 75
6. Spontaneous Charging of Drops on Lubricant-Infused PDMS Brushes[§].....89
6.1 Introduction.....90
6.2 Experimental 91
6.3 Results and Discussion 94
6.4 Conclusions.....101
6.5 Appendix IV.....102
7. Conclusion 105
References 109
Acknowledgements.....133
Curriculum Vitae 135

1. Introduction

Wetting is a common phenomenon in nature and our daily lives. It is characterized by the liquid film on the surface. In opposite, if the surface is not wetted by the liquid, spherical drops are formed on the surface. This is attributed to the low solid surface tension. Based on the principle of minimum energy, a contact angle is formed at three-phase contact line. Using three interfacial surface energies (solid-solid, solid-liquid, liquid-vapor), Young's equation[1] was introduced to describe the contact angle. However, the equation is only valid for equilibrium contact angle. When a drop slides on the surface, advancing and receding contact angle have to be considered. The two contact angles refers to the contact angle forming at three-phase contact line in the front and back side, respectively. The difference between advancing and receding contact angle refers to contact angle hysteresis, which characterizes the drop mobility on the surface. Contact angle hysteresis is essential because many applications reply on the fast removal of drops on the surface.

In **Chapter 2**, I introduced firstly the Young's equation, Wenzel model and Cassie-Baxter model, [2-5] and concepts of advancing/receding contact angles on flat and structured surfaces. On flat surface, equilibrium contact angle is described by Young's equation. On structured surface, Young's equation is invalid and the apparent contact angle depends on the solid surface tension and surface roughness. Wenzel model and Cassie-Baxter model were introduced to describe the different drop states on structured surface. In the Wenzel state, the liquid completely penetrates into the surface structures. While in Cassie-Baxter state, drop only stays on top of the structure, thus the water-solid contact area is small. For advancing and receding contact angles, the two common methods are introduced: sessile drop method and tilted plate method. [6-17] Sessile drop method involves drop inflation/deflation on the surface, while tilted plate method involves drop sliding on the surface. Advancing/receding contact angles and contact angle hysteresis can be detected from the captured video.

In the following, two representative surfaces (superhydrophobic surfaces[18-20] and lubricant-infused surfaces[21-23]) are introduced due to their significance in industry and our daily lives. Superhydrophobic surfaces usually have an apparent water contact angle of more than 150°. Some even have the low contact angle hysteresis of less than 5°. These surfaces exhibit good self-cleaning property that water drops sliding on the surface also takes away the contamination, e.g. dust or small particles. However, under high pressure or high humid environment, drops are not able to maintain Cassie-Baxter state thus superhydrophobicity is lost. One possible method to solve the problem is to infuse lubricant within the structures. It results in lubricant-infused surfaces. Due to the lower surface tension of lubricant, and the thin layer between drop and substrate, water exhibits low sliding angles on lubricant-infused surfaces. One problem is lubricant-infused surfaces suffer from depletion problem that lubricant is consumed when drops slide off the surface. For applications, the shortcomings would lead to a significantly decreased efficiency.

An alternative candidate that exhibits low water sliding angles is polydimethylsiloxane (PDMS) brushes coatings.[24-27] They consist of flexible polymer chains with one side covalently bonded to the substrate and the other side free in the air.[28, 29] With such unique chemical structure, the PDMS brushes exhibit low sliding angels for various liquids, including water and other low-surface-tension liquids. The mobility of water drops on PDMS brushes is even comparable to that of superhydrophobic surfaces. Moreover, the PDMS brushes coating is stable, easy to prepare, scalable to any substrate, and environmental-friendly. Thus it is important to better understand droplet dynamics on PDMS brushes and bring it forward to the applications. In **Chapter 3**, I developed a strategy to further reduce the water/ice lateral adhesion on PDMS brushes by introducing organic vapor. The low lateral adhesion towards water drops on PDMS brushes is attributed to the flexible polymer chains, which can repel drops easily. In the presence of organic vapor, the brushes are more flexible, thus it can greatly further reduce the drop lateral adhesion

on PDMS brushes. Using vapor lubrication, I also presented its potential in many aspects, e.g. water collection, anti-icing, and drop manipulation.

However, Behrooz Khatir and Kevin Golovin[30] pointed out that the low drop lateral adhesion can be explained simply the change in the interfacial energies by vapor. To find out which effect contributes how strongly, in **Chapter 4**, I measured contact angles of water drops on three hydrophobic surfaces in different vapors (including water-soluble vapors, water-insoluble vapor, and air) and compared it with theoretical values, which are obtained from Young's equation. The results show that the decrease of mean contact angles in water-soluble vapors can be explained by vapor-induced change in the interfacial energies. However, the low contact angle hysteresis on PDMS surfaces in water-insoluble vapors cannot be explained by Young's equation. These results support my hypothesis of vapor lubrication in PDMS brushes.

Because PDMS brushes show advantages when compared to superhydrophobic surfaces and lubricant-infused surfaces, e.g. better stability and durability. In **Chapter 5**, I investigated the condensation heat transfer performance of ethanol-water mixtures on PDMS brushes coated silicon substrate. The coating is able to repel ethanol-water mixtures at any ratio, while the liquid properties, e.g. surface tension, latent heat of vaporization, can be optimized. With this strategy, we found that the condensation heat transfer coefficient can be enhanced 10 times when compared to that on an uncoated silicon surface. Furthermore, the critical heat flux which determined dropwise-to-filmwise transition was also enhanced when compared to that on a traditional fluorinated surface.

Despite of the depletion, lubricant-infused surfaces are still one of the promising surfaces in many fields, e.g. enhanced condensation, drag reduction, and bubble transportation. In **Chapter 6**, I studied slide electrification of water drops on lubricant-infused PDMS brushes, which was not explored before. The charging effect of water drops on lubricant-infused PDMS brushes is significantly different from that on PDMS brushes or hydrophobic surfaces without lubricant. In

series of drops, the charge per drop first increases with drop number, the decreases, and after a minimum saturates on lubricant-infused surfaces. We attributed this phenomenon to the lubricant depletion because the saturated charge on the PDMS brushes with and without lubricant are similar. The results here provide the new insight of slide electrification on lubricant-infused surfaces and I hope it contributes to better understand slide electrification.

2. Fundamentals

2.1 Contact Angle Phenomena on Surfaces

2.1.1 Equilibrium Contact Angle

When depositing a liquid drop on a solid surface, the liquid can either form a hemispherical drop or a thin film on it. The first case is usually characterized by the contact angle (θ) of a given liquid on the surface. As shown in **Figure 2.1a**, contact angle is geometrically defined as the angle formed by three interfaces: solid-vapor, solid-liquid, and liquid-vapor interfaces. For an ideal solid surface that is perfectly flat, rigid and chemically homogeneous, the equilibrium/static contact angle is given by Young's equation: [1]

$$\cos\theta = (\gamma_{SV} - \gamma_{SL}) / \gamma_{LV}, \qquad \text{(Equation 2.1)}$$

where γ_{SV}, γ_{SL} and γ_{LV} are the interfacial tensions between solid-vapor, solid-liquid, and liquid-vapor. For a surface with $\theta > 90°$ towards water (oil), it is usually called hydrophobic (oleophobic) surface and it has good water (oil) repellency; in the case of $\theta < 90°$, the surface is called hydrophilic (oleophilic).

On structured surfaces, the roughness plays an important role in the drop contact angle. Two models, Wenzel model[2, 3] and Cassie-Baxter model[4, 5] were developed to demonstrate the drop state on structured surface (**Figure 2.1b**). In the Wenzel state, the liquid completely penetrates into the surface structures. Thus, the real contact area of the drop-solid is much larger than that on a flat surface. In this case, the apparent contact angle on the rough surface can be described as:

$$\cos\theta_w = r\cos\theta, \qquad \text{(Equation 2.2)}$$

where θ_w is the apparent contact angle in Wenzel State, and r is the roughness factor, which is defined as the ratio of the true surface area to the apparent surface area (r = 1 for a smooth

surface, $r > 1$ for a structured surface). The Wenzel equation predicts that, roughness amplifies the drop contact angle when compared to the flat surface. When increasing the surface roughness, the apparent contact angle is larger (smaller) for $\theta > 90°$ ($\theta < 90°$) and the surface is more hydrophobic (hydrophilic). Notably, the equation is only applicable when the liquid fully penetrates into the surface structure.

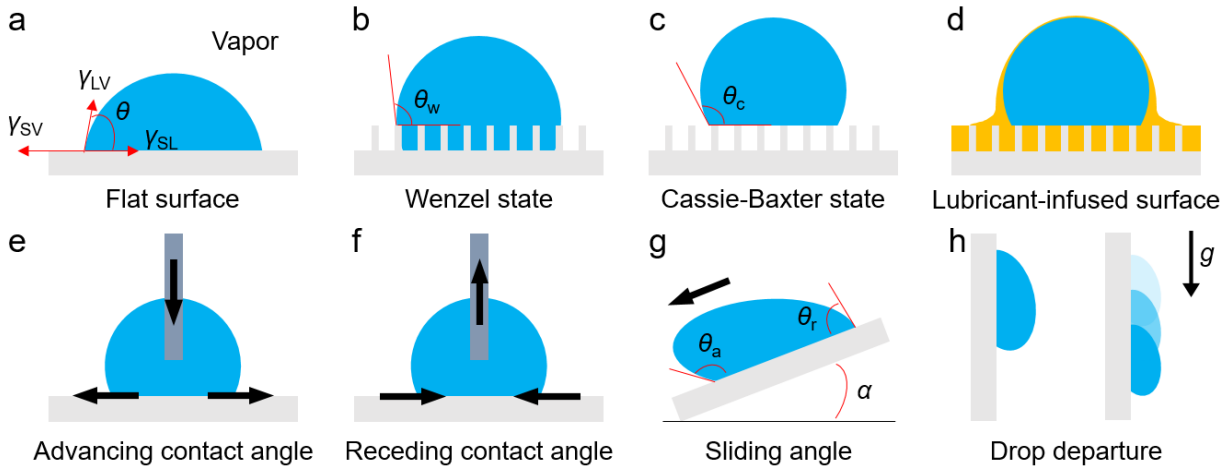

Figure 2.1 The schematic shows the contact angles on a flat surface (a), a structured surface in the Wenzel (b) and Cassie-Baxter (c), and lubricant-infused surface (d). Schematic of two common methods to measure advancing and receding contact angles: sessile drop method (e,f) and the tilted plate method (g). (h) Drops with different sizes slide off vertically placed surfaces.

When the structured surface has low solid surface tension, the liquid does not fill the gap between the protrusions of the surface. In that case, liquid drop is in a Cassie-Baxter state, anther equation was developed: [31, 32]

$$\cos\theta_c = \varphi_s(1+\cos\theta) - 1. \qquad \text{(Equation 2.3)}$$

Here, φ_s is the solid fraction of the contacting area. The apparent contact angle increases with the decreased φ_s. The low value of φ_s makes the surface more hydrophobic (oleophobic). When φ_s approaches 0, the contact angle becomes ≈180°, this is extremely hydrophobic (oleophobic). Therefore, reducing the liquid-solid contact is one efficient method to achieve the super liquid

repellency. However, φ_s cannot reach 0 in reality, but can only be reduced to approach 0 at some specific cases. For example, on a hot plate, [33, 34] or inside a low pressure chamber, [35] a water drop is held up by the underlying vapor layer. Due to gravity, water drop jumps on the surface. In other cases, e.g. droplet pressure, impact, or vibration, [36-40] Cassie-Baxter state is also not stable, partial or total Wenzel state occurs. To solve this problem, lubricant is filled into the structure. The resulted surfaces are called "lubricant-infused surfaces". [22, 41] The lubricant has to be immiscible with the drop and usually has lower surface tension. Thus the lubricant reduce the solid surface tension and make liquid drops more mobile. When depositing a liquid drop on lubricant-infused surfaces, the drop sits on the lubricant and a meniscus is formed by the lubricant at the three-phase contact line (**Figure 2.1d**). [42-44]

2.1.2 Advancing/Receding Contact Angles

When considering a drop slide on a solid surface, the angles formed at the three-phase contact line differ from that in the equilibrium/static state. The contact angle in the front side of the drop, the advancing contact angle (θ_a), is larger than that in the back side, which is the receding contact angle (θ_r). [45-47] The different between these two contact angles is called contact angle hysteresis. [48, 49] It denotes the drop mobility on the surface and reflects the surface characteristics, e.g. surface roughness and chemical heterogeneity. The lower the contact angle hysteresis, the more easily drops slide on the surface. The contact angle hysteresis can be measured using any technique that detects the advancing and receding contact angles. [50-62] The most common two are the sessile drop method and tilted plate method. [6-17] In the sessile drop method, the drop volume is gradually increased and decreased by a syringe. When increasing (decreasing) the drop volume, the contact line advances (recedes) on the surface and the advancing (receding) contact angle can be detected (**Figure 2.1e,f**). In the tilted plate method, the surface is tilted gradually until the gravitational driving force is high enough that the drop slide on the surface. Right before the moment when drop starts to slide, the advancing (front side) and receding (back

side) contact[63] angle is measured (**Figure 2.1g**). The tilted angle when a drop starts to slide on the surface is called sliding angle (α). When tilted angle equals to α, the lateral adhesion force equals to the lateral component of the gravitational force. Therefore, the sliding angle can be obtained theoretically by: [14, 15, 63, 64]

$$\sin\alpha = \frac{wk\gamma_{LV}}{mg}(\cos\theta_r - \cos\theta_a). \qquad \text{(Equation 2.4)}$$

Here, w is the width of the contact area of the drop, γ_{LV} is the liquid surface tension in the drop and $k \approx 1$ is a geometrical factor, which depends on the shape of the drop, m is the mass of the drop, and $g = 9.81\ m{\cdot}s^{-2}$ is the gravitational acceleration. The drop width of the contact area and drop mass are related to the drop volume. Thus the equation reveals that the sliding angle is influenced by the drop volume, receding and advancing contact angles. In opposite, if the tilted angle is fixed (**Figure 2.1h**), the drop volume is highly affected by the receding and advancing contact angle. The maximum drop volume at which droplet starts to slide off the surface is called departure droplet volume, and the corresponding radius (diameter) is called departure droplet radius (diameter). Departure droplet radius is an essential parameter in many applications, e.g. condensation heat transfer, water harvesting. It influences the departure process and later re-nucleation and re-growth processes involved in the condensation.

2.2 Superhydrophobic surfaces

Superhydrophobic surfaces[18-20] are usually defined as surfaces with an apparent water contact angle of more than 150° (**Figure 2.2a**). Superhydrophobic surfaces that have low sliding angles for water exhibit good self-cleaning effect that, the contamination can be washed away easily. Ever since their introduction, superhydrophobic surfaces have been attracted more and more attention and some are found to show application potentials in many areas, e.g. anti-icing surfaces, [24, 65-68] drag reduction, [69-72] and enhanced heat transfer. [73-76] The superhydrophobic surfaces are inspired initially from natural plants, [18, 77] e.g. lotus leaf, rice leaf, taro leaf, and watermelon. The

most well-known one is the lotus leaf, which has been regarded as a symbol of purity since thousands of years ago. Even in the Northern Song Dynasty (960-1127) from china, there is a poem by Dunyi Zhou writing, “An emblem of purity and truth, the lotus springs from mud and yet it stays pure and untainted”. However, the mechanism of behind this phenomenon is not clearly unsolved until the introduction of scanning electron microscopy. [78, 79] By scanning the lotus leaf’s surface, people directly see its rough structured surface: microscale nubs (distance ≈30 μm) covered with roughed epicuticular wax crystalloids (much smaller scale). Besides the structure, the self-cleaning property is also attributed to the low-surface-tension chemical components (-C-H-, -C-O-) on top of the leaf’s structure. As introduced in Section 2.1.1, if the surface tension is high, water drops show Wenzel state on the surface.

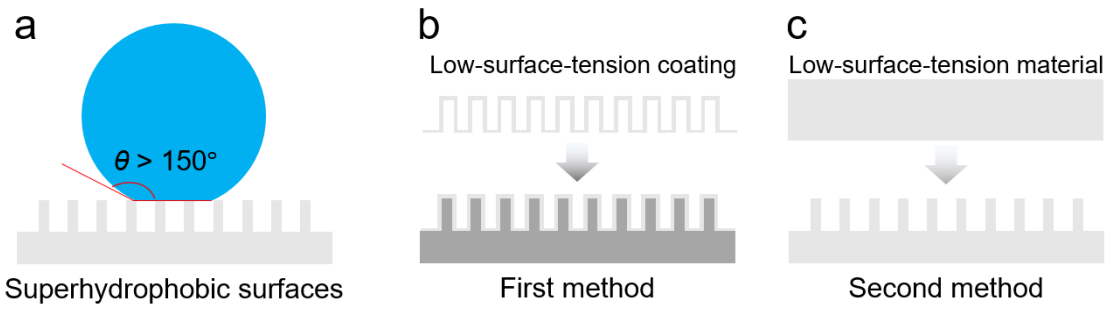

Figure 2.2 (a) The schematic shows the equilibrium Contact Angle contact angle on superhydrophobic surfaces. (b, c) Preparation methods for superhydrophobic surfaces. First method: combination of structure and low-surface-tension coatings. Second method: constructing micro/nano structures on hydrophobic materials.

2.2.1 Preparation Methods

On the basis of the investigations on lotus leaf, two types of approaches are developed to prepare artificial superhydrophobic surfaces with self-cleaning property. The first one is the combination of structure and low-surface-energy coatings (**Figure 2.2b**). In 1967, Dettre et al[80] fabricated superhydrophobic surfaces by coating 1,1,2-trichlor-1,2,2-trifluorethan on several structured surfaces. The structures were fabricated by pressing or rapidly peeling the mesh from the polymer

(polyethylene, polypropylene). Beforehand, polymers were heated to temperatures slightly below their softening point. The advancing contact angle on the porous polyethylene surface reached 171°. The second method is to make micro and/or nanostructure structured surface using hydrophobic materials (**Figure 2.2c**). In 1996, researchers from Kao Corporation[81] used a dip-coating method to coat a thick alkylketene dimer layer (100 μm) on the glass slide. It results in a fractal alkylketene dimer surface. Water showed a contact angle of 174°. Afterwards, more and more methods have been developed to prepare surface with superhydrophobicity and self-cleaning property, e.g. wet chemical reaction, [19, 82-86] lithography, [87-91] chemical vapor deposition, [92-96] plasma etching, [97] crystallization control, [98] polymerization reaction, [99] layer-by-layer, [100] etc. [101] However, the structured surfaces rely on the low fraction between the contact area with liquid and the whole surface area, which is fragile and highly susceptible to abrasion. To solve this problem, Wang et al[102] recently fabricated a robust surface by combining nanostructure for water repellency and microstructure for protection. The microstructure is an interconnected surface frame and acts as armour that protecting the highly water-repellent and mechanically fragile nanostructures from abrasion. The water contact angle on the surface reached ~170°, and sliding angle reached ~2°. Even after 1000 abrasion cycles, the sliding angle was still ~10°, showing the excellent mechanical stability of the armoured superhydrophobic surface.

2.2.2 Applications

Ice and snow adhesion and accumulation on exposed equipment surfaces causes many serious problems in cold areas, e.g. Iceland, Norway, Finland, Canada, Russia, and America. One promising method is to coat these surfaces with a suitable superhydrophobic layer, due to the reduced contact fraction towards liquids/solids. One advantage is superhydrophobic surfaces can reduce the ice formation from impinging droplets. It is attributed to the reduced contact time and the increased nucleation energy barrier. [65, 103-108] Alizadeh et al[107] compared the nucleation rate of water on hydrophobic and hydrophilic surfaces. It was found that when the contact area was

increased from 10 mm^2 to 20 mm^2, the nucleation rate increased by 10 orders of magnitude. Cao et al[65] reported that by pouring supercooled water (-20°C), ice formed instantly on uncoated aluminum substrate. In opposite, although it built up from the bottom edge (no coating), ice did not form directly on coated aluminum. Mishchenko et al[104] investigated the behavior of impacting droplets (-5°C to 60°C) on different cooled and tilted substrates (surface temperature: -30°C to 20°C tilted angle: 30°). It was found that droplets could fully retract before freeze on superhydrophobic surface at surface temperatures above −25°C, while ice was observed on a flat hydrophobic surface. The other advantage is that ice block exhibit low lateral adhesion on superhydrophobic surfaces. The two common methods for ice lateral adhesion measurement is shearing an ice block using a force probe, or removing the ice block using centrifugal force. Wang et al[109] reported that the ice lateral adhesion on a perfluorodecyltriethoxysilane-coated structured aluminum surface was only 13% of that on an uncoated superhydrophobic substrate. Kulinich et al[66, 110] found that with the decreased contact angle hysteresis from 70° to 10°, the ice lateral adhesion strength was reduced 80%.

The other attractive applications for superhydrophobic surfaces are those involving condensation.[26, 111] For example, the condensation heat transfer performance effectively influences the thermal efficiency of the steam cycle, which plays an important role in producing electricity all over the world.[75] Considering condensation, dropwise and filmwise condensation are two different condensation modes. In one case, the cooled surface is not wetted during condensation that discrete droplets form on the surface. That is called “dropwise condensation”. In the case that condensate forms a liquid layer on the surface, which is called “filmwise condensation”. Because the liquid layer increases the thermal resistance for condensation, dropwise condensation is much more efficient to the filmwise condensation. The efficiency is characterized by heat transfer coefficient ($kW \cdot m^{-2} \cdot K^{-1}$), which is the ratio between heat flux ($kW \cdot m^{-2}$) and subcooling (K). Heat flux means the amount of the heat transferring during condensation, while the subcooling means

the temperature difference between vapor and surface. In principle, hydrophobic surfaces are sufficient to sustain dropwise condensation. However, it was found that on a superhydrophobic surface, condensed droplets could not only slide off the surface, but also jump away from the surface. [112] It was attributed to the released surface energy. [113] With such jumping effect, the condensation heat transfer efficient was increased by 30% as compared to conventional dropwise condensation. However, droplet jumping motion only occurs at low subcooling (<2K), because nano-droplets nucleate in the micro-defects at high subcooling, which promotes flooding. To improve the jumping effect, Yang et al[114] fabricated a three-dimensional copper nanowire networks, which can maintain droplet jumping motion at higher subcoolings (2K - 28K). A 100% higher heat transfer coefficient on 3D superhydrophobic nanowire networks was achieved as compared with dropwise condensation on hydrophobic surface. At high subcoolings, however, superhydrophobic surfaces face the problem that partial/total filmwise condensation occurs eventually. To delay the dropwise-to-filmwise transition, Lu et al[115] constructed hydrophilic microchannels on superhydrophobic silicon nanowires. With the sacrifice of the partial condensation area, dropwise condensation was more stable on the other areas at higher subcoolings. By rational design of the ration between hydrophobic and hydrophilic areas, a more than 100% enhancement of heat transfer coefficient was achieved when compared to the state-of-the-art superhydrophobic surfaces.

2.3 Lubricant-Infused Surfaces

Superhydrophobic surfaces exhibit good water repellency due to the trapped air within structures (Cassie-Baxter state). However, the Cassie-to-Wenzel transition can be triggered by pressure, impact, or vibrations. [36-40, 116-118] One method to solve this problem is filling the structures with lubricant (**Figure 2.1d**). Such surfaces are called “lubricant-infused surfaces” or “slippery liquid-infused porous surface”. [21-23] It is inspired by Nepenthes pitcher plants, where its peristome’s microstructure can entrap some water to create a thin lubricant layer, thus the insects fall off to

pitcher's pockets. [119, 120] The concept of lubricant-infused surfaces, where micro- and nanostructures are used to lock the infused lubricant, is different from that of lotus effect. Because of the locked lubricant oil on top of the surface, liquid drops don't contact with the substrate directly. Instead, a thin lubricant layer holds up the drop. Thus lubricant-infused surfaces usually exhibit very low contact angle hysteresis towards various simple and complex liquids, e.g. water, hexane, and blood. [21-23, 121] Due to the mobile lubricant, the coating is also self-repairing. Lubricant-infused surfaces have attracted much attention ever since they were introduced because of its potential applications in, e.g. fluid transport, medicine, and antifouling materials.

2.3.1 Preparation Methods

The design criteria of lubricant-infused surfaces is described as following: [122-125] (1) the lubricant is stable and fully wettable within the substrate, (2) the lubricant is immiscible with the test liquid; (3) the substrate is easier to be wetted by the lubricant instead of test liquid. Following these rules, preparation of lubricant-infused surfaces is quite straightforward: constructing structures on the substrate and then infusing suitable lubricant. The methods for constructing structures can be same as those for superhydrophobic surfaces. Lubricant have many species, including Krytox lubricant, [126-141] Fluorinert liquid, [43, 142-145] Fomblin lubricant, [146-150] ionic liquids, [143, 151-154] and silicon[55, 155-161] and other oils. [162-167] The most used lubricant are Krytox lubricant and silicon oil, the component is perfluoropolyether and linear polydimethylsiloxane, respectively. They both have been used as lubricant for mechanical equipment for a long time, and have the advantage of low surface tension, low vapor pressure, and chemical inertness.

Recently, researchers also found that lubricant-infused surfaces can be prepared on flat surfaces. [168-174] Instead of structure, they use thin monolayers (several nanometers) to retain the lubricant on the surface. Due to intermolecular interactions, a thin lubricant layer can be formed on the surface. For example, Ingber et al[168] prepared flexible molecular layer of perfluorocarbon by immersing the substrates in a solution (5% v/v tridecafluoro-1,1,2,2-tetrahydrooctyl trichlorosilane

in anhydrous ethanol). Afterwards, the substrates were dip-coated in perfluorodecalin to form lubricant layers. The results showed that the sliding angles of blood drops can be significantly decreased (from more than 90° to less than 1°) by the combination of thin flexible layer and lubricant. The strategy can be applied to different substrate, e.g. polycarbonate, polyethylene, polyimide, glass, and titanium. The coating also showed good anti-blood property by significantly reduce the fibrin clot and adherent platelets.

2.3.2 Applications

Due to the mobile lubricant, ice block is easy to be removed on lubricant-infused surfaces. Subramanyam et al[175] reported that the ice lateral adhesion strength on a lubricant-infused surface is only 1/3 and 1/10 of that on an octadecyltricholosilane-coated and uncoated flat silicon substrate, respectively. Kim et al[130] investigated the anti-ice and anti-frost properties by cooling different surfaces at -2°C in high humid (60%) environment. After 100 minutes, more than 99% of fluorinated aluminum substrate was covered by ice while it was only 20% on lubricant-infused aluminum. The ice formation on lubricant-infused surface was mainly attributed to the edge effect.

The condensation of low-surface-tension liquids is crucial in many applications, e.g. refrigeration[176], natural gas processing[177] and power generation[178]. Because of the unique property to repel low-surface-tension liquids, lubricant-infused surfaces are promising to enhance the condensation heat transfer of these liquids, e.g. ethanol, hexane, toluene. Rykaczewski et al[141] reported that lubricant-infused surfaces can successfully sustain dropwise condensation for several low-surface-tension liquids, e.g. toluene, octane, hexane, and pentane. These liquids all exhibited filmwise condensation on unimpregnated superhydrophobic surface. However, lubricant-infused surfaces exhibited poor durability because of lubricant depletion. [179] To improve the stability, Sett et al[180] found that with proper lubricant selection (Krytox 1525), the time for steady dropwise condensation could be elongated to 7 hours.

2.4 PDMS brushes

As shown in **Figure 2.3a**, PDMS brushes consists of repeating siloxane groups (-O-Si-O-). One side of these polymer chains is attached to the substrate, while the other side is "free" in the air. The glass transition temperature of PDMS is -127°C, [29, 181] thus its polymer chains are highly mobile through rotational and/or bending motions. Usually, the contact angle hysteresis of water or low-surface-tension liquids e.g. ethanol, on PDMS brushes is less than 5°.[29]

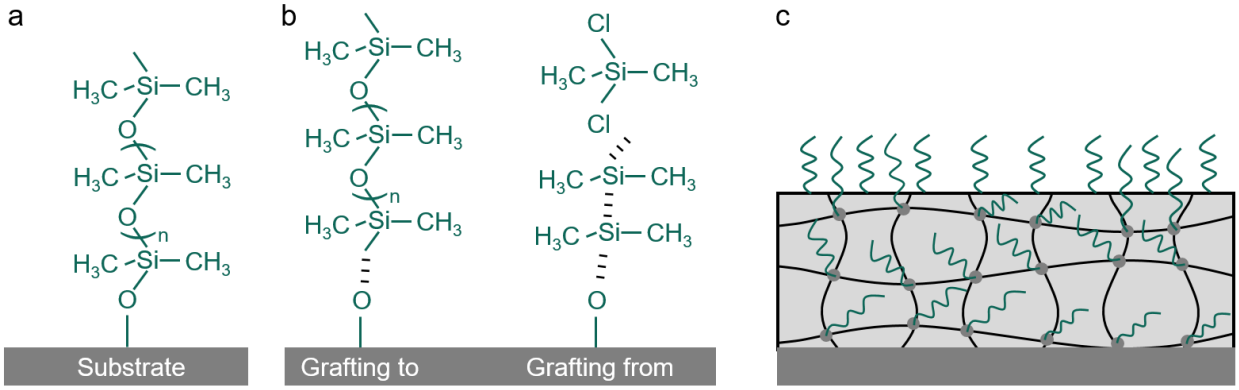

Figure 2.3 (a) Schematic showing chemical composition and structure of a single PMDS polymer chain. (b) Preparation methods for PDMS monolayer: grafting to using high-molecular-weight PDMS polymers and grafting to using monomers. (c) Schematic showing one example for PDMS thick coating. PDMS brushes are grafted within the whole thick coating.

2.4.1 Preparation Methods

Depending on the thickness, two types of PDMS brushes are fabricated. One is only few nanometer thick and the other one usually has a micrometer thickness. In the following, the representative methods for preparing these two types of PDMS brushes are summarized.

The PDMS monolayer can be prepared through either the "grafting to" or "grafting from" methods (**Figure 2.3b**). The "grafting to" method is straightforward, usually no catalyst needed, but time-consuming. It involves the chemical reaction of a linear PDMS polymer chains with the substrate. The substrate needs to be functionalized either simply by oxygen plasma for hydroxyl groups, [182-

[184] or complicatedly by spin-coating for epoxy or other groups. [185] Then PDMS is grafted onto the substrate by covering the surface by PDMS liquid, under high-temperature (100 °C) or ultraviolet light environment. The reaction may happen both at the end and in the middle of the PDMS chain, however, it is always to be believed that PDMS brushes are grafted on the substrate. Without heating or other external effort, PDMS could also be grafted onto the hydroxyl-activated substrates. However, the process is slow, may take more than 24 hours at room temperature. [184] The process is universal and applicable to most linear PDMS chemicals, e.g. trimethylsilyl-, hydrogen-, thiol, amino-, or vinyl- terminated PDMS through rational design. [186, 187]

The “grafting from” method involves the polycondensation of reactive monomers on the substrate. It is a fast method, but may need catalyst, depending on the reactivity of the monomers. If using chlorine-terminated siloxane, e.g. dimethyldichlorosilane, [188] 1,3-dichlorotetramethyldisiloxane, [189] the chlorines spontaneously react with water molecules. It results in a hydroxyl-terminated siloxane and hydrochloric acid, which acts as a catalyst for polymer chains growth via polycondensation. [190, 191] Therefore, PDMS monolayer can be formed on the surface without catalyst in few minutes. For the less-reactive monomers, e.g. dimethyldimethoxysilane, [192, 193] viny-terminated PDMS, [194] catalyst (acid, Pt) is required to start the polymerization. The reaction depends on the specific chemicals, ranging from few seconds to several days.

PDMS monolayer is only few nanometer thick. Although it exhibits low water sliding angle, PDMS monolayer is easy to be damaged and has poor durability in applications. To make the coating more durable, thick coatings with PDMS brushes on the surface are designed and fabricated (**Figure 2.3c**). The PDMS polymers can be interspersed into the entire coating matrix so PDMS brushes can be refreshed after damage, e.g. abrasion or scratches. As long as the coating material remains on the substrate, PDMS brushes is alive and the coating retains its water-repellency. Liu et al[195] prepared a polyurethane-PDMS coating by “copolymerization” method, using hexamethylene diisocyanate trimer, PDMS-grafted polyol, and polyol. PDMS brushes

spontaneously form on the surface of the polyurethane film during coating formation owing to the self-stratification of PDMS. Due to the internal structures, the coating exhibited good wear tolerance. After 1920 cycles with a cotton-fabric-wrapped probe, the water contact angle on the surface only decreased from 103° to 100°. PDMS brushes can also be grafted onto the particles or elastomer matrix. The only principle is to make sure that only one end of the PDMS brushes chains are covalently attached. So mono-functional PDMS, [195-197] e.g. monochlorocarbonyl-terminated, monoepoxy-terminated, and monoaminopropyl-terminated PDMS, are always used during preparation of thick coatings. If more than 2 positions are attached on the coating, the PDMS polymer chains will lose its liquid-like property.

2.4.2 Applications

The liquid-like characteristics of PDMS brushes allow for reduced interfacial adhesion and broad applications in anti-contamination towards both liquids and solids. It has been reported that PDMS brushes can effectively repel various single/complex liquids, e.g. Krytox-101 (surface tension: 17 $mN{\cdot}m^{-1}$), pentane (surface tension: 16 $mN{\cdot}m^{-1}$), FC-72 (surface tension: 10 $mN{\cdot}m^{-1}$), crude oil, urine, corrosive agents, liquid food, and ink. [190, 198-205] Therefore, PDMS brushes show strong potential applications in enhancing condensation heat transfer of low-surface-tension liquids. Recently, Rabbi et al[202] demonstrated that PDMS brushes can sustain dropwise condensation of ethanol, hexane, and pentane. The heat transfer coefficient of ethanol condensation on PDMS brushes showed more than 200% enhancement, when compared to that of filmwise condensation. For anti-solid properties, Zhao et al[206] reported that an ice block (1 cm × 1 cm × 2 cm) easily slid off the PDMS brushes coated silicon wafer, relying on its own weight. The ice lateral adhesion strength of the ice block is 0.3 kPa, which is 3 orders of magnitude lower than a typical fluorinated surface.

PDMS brushes also show additional advantages when compared to the state-of-the-art superhydrophobic surfaces and lubricant-infused surfaces. Superhydrophobic surfaces exhibit

low lateral adhesion towards liquids/solids, however, they require micro/nano structures and also low-surface-tension coatings, e.g. fluorocarbon. PDMS brushes only require a flat substrate. Meanwhile, it is also demonstrated that PDMS brushes showed better antifouling property than fluorocarbon coatings on a flat surface. [207] Chen et al[208] demonstrated that under same condition, $CaSO_4$ scale was hardly observed on PDMS brushes, while on fluorinated surface, the scale formation is 4.8×10^{-3} mg·cm^{-2}. Wu et al[205] reported that after 1 day of incubation, PDMS brushes exhibited significantly reduced fouling, e.g. staphylococcus aureus, escherichia coli. Recently, Zhang et al[190] demonstrated that the friction coefficient of a load (weight: 10.2 kg) on PDMS brushes was 0.019, which is 4.5 % and 34.5% of that on a pure silicon substrate, and a lubricant-infused surface, respectively. Friction coefficient is a dimensionless value which characterizes the difficulty of liquid/solid sliding on the surface. The lower the friction coefficient, the easier the liquid/solid slides.

3. Vapor Lubrication for Reducing Water and Ice Adhesion on PDMS Brushes§

Fast removal of small water drops from surfaces is a challenging issue in heat transfer, water collection or anti-icing. Polydimethylsiloxane (PDMS) brushes show good prospects to reach this goal because of their low lateral adhesion to liquids. To further reduce adhesion of water drops, here, we expose the surface to the vapor of organic solvents such as toluene or n-hexane. In the presence of such vapors, water drops slide at lower tilt angle and move faster. It is mainly caused by the physisorption of vapor and swelling of the PDMS brushes, which serves as a lubricating layer. Enhanced by the toluene vapor lubrication, the limit departure volume of water drop on PDMS brushes decreases by one order of magnitude compared to that in air. As a result, the water harvesting efficiency in toluene vapor increased by 65%. We further demonstrate benefits of vapor lubrication in drop manipulation and de-icing via the gravity of ice itself.

---

§ This chapter is a slightly modified version of the following article: [209]

Li, S., Hou, Y., Kappl, M., Steffen, W., Liu, J., and Butt, H.-J., Vapor Lubrication for Reducing Water and Ice Adhesion on Poly(dimethylsiloxane) Brushes. Adv. Mater. **2022**, 34(34): 2203242.
Copyright © 2022 The Authors. Advanced Materials published by Wiley-VCH GmbH, under the terms of the Creative Commons CC BY license.

Author Contributions: Li, S., Liu, J., and Butt, H.-J. designed the research and experiments. Li, S. and Liu, J. carried out the surface fabrication. Li, S. and Kappl, M. conducted the force spectroscopy experiments. Li, S. and Hou, Y. designed the condensation chamber for applications. Li, S., Hou, Y., Liu, J., Steffen, W., and Butt, H.-J. wrote the manuscript. All authors have given approval to the final version of the manuscript.

3.1 Introduction

Facilitating the sliding of liquid drops from solid surfaces is critical to keep windows transparent, enhance heat and mass transfer efficiency, [26, 111, 210-212] or inhibit ice deposition. [24, 41, 213, 214] Strategies of regulating morphology and chemistry of surfaces are developed to achieve low lateral adhesion of sessile drops on surfaces. By constructing micro and/or nanoscale structures with coating of low-surface-energy chemicals, superhydrophobic surfaces exhibit low contact angle hysteresis for water. [215, 216] Water drops placed on superhydrophobic surfaces trap an air layer underneath. In this state, called the Cassie state, drops ball up and assume an almost spherical shape. The real contact area between the drop and such surface is much lower than the apparent contact area. However, the surfaces tend to fail to repel water under pressure or condensed water formed at high-humidity conditions because no Cassie-state is formed. [76] An alternative is to infuse porous nanostructures with a second liquid, which is immiscible with the drop. Such lubricant-infused surfaces show low lateral adhesion for liquids with a broad range of surface tensions as well as solids. [41, 42, 217] However, lubricant is depleted by gravitational drainage, evaporation or sliding drops, which leads to the loss of the surfaces' low-lateral-adhesion performance. [125, 218] Consequently, in order to realize the surfaces with both low liquid adhesion and long-term serviceability, the stability of the lubricant layer is a critical problem needs to be overcome. [125, 213, 219]

An alternative of low-lateral-adhesion surfaces is to covalently attach flexible macromolecule brushes onto smooth substrate, e.g., polydimethylsiloxane (PDMS) brushes. With a small barrier of internal rotation of the -O-Si-O- bond, PDMS backbone are highly flexible. [220-222] The PDMS chains with one free side and high mobility make the brush layer demonstrate a liquid-like lubrication effect. Since the other side is covalently linked to the substrate the brush is not depleted by the applied liquids. However, comparing to superhydrophobic surfaces and lubricant-infused surfaces, the PDMS brushes still show a higher lateral adhesion to drops. [223]

To reduce lateral adhesion of sessile drops one needs to reduce the contact angle hysteresis, which is the difference between the advancing θ_a and the receding contact angles θ_r. The force required to move a drop laterally is given by[224]

$$F = w\gamma_L k(\cos\theta_r - \cos\theta_a) \quad \text{(Equation 3.1)}$$

Here, w is the width of the contact area of the drop, γ_L is the surface tension of the liquid in the drop and $k \approx 1$ is a geometrical factor, which depends on the shape of the drop. To achieve low sliding angles and reduce the gravitational force needed for drops to slide, the difference between advancing and receding contact angles should be as small as possible. The lateral adhesion of water on the PDMS brushes can be further reduced and slide velocities increased via tethering liquid by the layer.[156,157] However, it's still a challenge to realize a durable liquid-tethered layer on PDMS brushes.

Here, we developed a strategy to reduce the adhesion of drops to PDMS brushes by exposing the surface to an organic solvent vapor. The brushes physically adsorb the vapor molecules because of the free energy of mixing between PDMS and solvent.[225] Thus, the thickness of the brush layer increases, which we confirmed later using Atomic Force Microscope (AFM) measurements.[226,227] As a result, the brushes become more flexible and water drop on such surface presents a lower sliding angle. With lower lateral adhesion, we found further benefits of the surface in promoting smaller drop departure radius, higher water collection rate, water drop manipulation, and lower ice adhesion. Ice adhesion also serves as a model for clathrate adhesion. Clathrates are a major problem in the oil and gas industry because they tend to block pipelines. We strong indicates that clathrates behave similar to pure ice with respect to adhesion.[228]

3.2 Experimental

Fabrication of PDMS brushes and fluorinated surface: The PDMS brushes were synthesized as described in the literature.[188] The silicon wafers (Silicon Materials Inc, P type, <1 0 0> orientation) were washed in hexane (98%, Sigma) and ethanol (99.5%, Sigma) with ultrasonication for 5 min, respectively. Then the substrates were treated with an oxygen-plasma (Diener Electronic Femto, 120W, 6 $cm^3 \cdot min^{-1}$ oxygen flow rate) for 5 min. Afterwards, the substrates were immersed in 40 mL toluene (with saturated water) mixed with 1.4 mL dimethyldichlorosilane. After reacting for 0.5 h, the substrates were rinsed with toluene to remove the residues and dried with nitrogen. Glass cover slips (precision cover slips, Carl Roth GmbH + Co. KG, 24×60×0.17 mm) were coated in a similar way. The fluorinated surface was prepared as described in the following. The PDMS brushes by “grafting to” method is synthesized as following: A drop of silicon oil was deposited on the clean silicon surface, before put in the oven at 92°C for 24 hours. Afterwards, it was cleaned by hexane and water. The 1H,1H,2H,2H-perfluorodecyl-trimethoxysilane (PFDTS) was prepared as following: after oxygen plasma treatment as before, silica wafers were put into a vacuum desiccator with 20 µL PFDTS added in the bottom. Chemical vapor deposition was lasted for 12 h. Finally, the substrates were heated in an oven at 120°C for 2 h.

Contact angles: Advancing and receding contact angles were measured using a goniometer (OCA35, Dataphysics) when water volume was gradually ($1 \mu L \cdot s^{-1}$) increased from 10 µL to 20 µL and decreased from 10 µL to 20 µL, respectively. The contact angles of water in toluene vapor were measured in a sealed chamber, in which toluene was used to generate saturated vapor. Each value was repeated for more than 6 times. All the experiments including the measurements below were conducted in atmospheric pressure without further statement.

Sliding angle: The sliding angles were measured by the goniometer (OCA35, Dataphysics). A water drop (1, 3, 5, 10, 20 µL) was pipetted on the surface. Then the stage was started to rotate

at a slow speed. The angle where the drop started to slide on the surface was recorded as sliding angle. Each result was repeated more than 3 times.

Sliding velocity: The sliding velocity of water drops on PDMS brushes at a certain tilt angle was measured via analyzing the motion of the sliding drops recorded with a digital camera. For the test of water sliding with an added toluene drop, a toluene drop was placed right next to a water drop on a tilted PDMS-coated silicon wafer, the drops immediately coalesced followed by toluene forming a wetting ridge around the water drop. The motions of 10 μL water drops on tilted PDMS brushes at α = 5° and 10° were recorded. The drop motions were then recorded for further analysis. Each result was repeated more than 3 times.

Confocal laser scanning microscopy: A water drop (5 μL) and a toluene drop (5 μL) were deposited and allowed to coalesce on a glass surface coated by PDMS brushes. The glass coverslip coated by PDMS brushes was mounted in the sample holder. The three phase contact area was observe with a confocal laser scanning microscope, Leica (Carl Zeiss, Jena, Germany) equipped with a C-Apochromat 40/1.2 W water-immersion objective. For excitation, two argon laser fiber-coupled to the microscope were used (488 nm and 633 nm). Atto 488 and disperse blue 14 were used as dyes for water and toluene, respectively. Each measurement was conducted more than 3 times.

AFM measurements: We used a Multi-Mode atomic force microscopy (Bruker) in force spectroscopy mode to characterize the brush thickness in the air, in the presence of toluene vapor and liquid using a liquid cell. AFM silicon cantilevers (OLTESPA-R3 from Olympus) with a nominal spring constant of ≈2 $N \cdot m^{-1}$ and a nominal tip radius of 7 nm were used. The scan rate was 1 Hz and the scan range was set to 100 nm resulting in a scan speed of 100 $nm \cdot s^{-1}$. Deflection sensitivity of the cantilevers was determined by taking cantilever deflection vs. piezo position curves on a pristine silicon wafer before every experiment. Raw cantilever deflection (in detector voltage) vs. piezo position data were recorded with a grid of 10 by 10 points on an area of 0.5×0.5

μm^2. These raw data were converted to force vs. distance curves using the measured deflection sensitivity to obtain cantilever deflection in nanometers, multiplying cantilever deflection with the nominal spring constant to obtain force, and by subtracting cantilever deflection from piezo position to obtain distance.

Condensation measurements: The departure size of drops and water harvesting performance were characterized from condensation experiments conducted in a custom-built device (**Figure S3.1a**, **Appendix I**). Two separate vapor flows controlled by two mass flow controllers (FMA-A2208, Omega) were used to vary the concentration of toluene and water vapor inside a chamber. The vapors were obtained by bubbling nitrogen through water or toluene, respectively. The sample was fixed on a vertical copper block. The copper block was cooled by a Peltier element. Once condensed water drops reached a certain critical size, they slide off the surface driven by gravity. [210, 229] The subcooling was controlled at ≈10K throughout the experiments. A Sony alpha 7RIII camera was employed to record videos. Departure droplet radius were calculated by comparing several time-lapsed images before and after departure process. Volume of collected water was calculated by a sum of the sliding drops according to the videos.

Ice lateral adhesion measurements: Anti-icing measurements were conducted in a custom-built chamber with cooling system (**Figure S3.1**, **Appendix I**). A 50 µL water drop was deposited on the surface, then the surface was cooled down to -25 °C to freeze the water drop. The force was continually recorded by a force gauge (PCE-DFG N 200) when the ice was pushed slowly at a speed of 60 $\mu m \cdot s^{-1}$. The lateral adhesion force corresponds to the force when the ice moved on the surface (**Figure S3.2**, **Appendix I**). The ice adhesion strength is defined as the adhesion force divided by the contact area (diameter: 5mm). Thus, ice adhesion strength is in Pa (**Figure 3.4f**).

3.3 Results and Discussion

To synthesize PDMS brushes, [188] oxygen plasma treated silicon wafers were immersed in a dimethyldichlorosilane-toluene solution (0.3 M), where the toluene is saturated with water. After 30 min, the substrate was coated with PDMS brushes. X-ray photoelectron spectroscopy proved the successful grafting of PDMS brushes because of the existence of the -O-Si$(CH_3)_2$-O- (≈102.5 eV) besides SiO_2 (≈103.5 eV) from silicon wafer (**Figure S3.3**, **Appendix I**). As schematically shown in **Figure 3.1a**, PDMS brushes tend to demonstrate a state that, one side of the PDMS chains is covalently attached on the substrate and the other side is free. As a result, the water sliding angle and contact angles on PDMS brushes do not change even after ultrasonically clean in toluene (**Figure S3.4**, **Appendix I**). The surface indeed shows low contact angle hysteresis against various liquids with different surface tensions, e.g. ethanol, toluene, dimethyl sulfoxide, etc. (**Figure S3.5**, **Appendix I**). The brush layer thickness (measurement details given below) was ≈4 nm with the surface roughness being lower than 1 nm (**Figure S3.6**, **Appendix I**). The layer thickness increases proportional to the grafting density Γ and the molecular mass of the PDMS chains M_w according to $L = \Gamma M_w/\rho$; here, ρ is the density of PDMS. Unfortunately, we cannot yet determine Γ and M_w independently. In air saturated with water (at 20 ± 2 °C), the surface is hydrophobic (**Figure 3.1b**) with advancing and receding contact angles for water of θ_a = 106° ± 1° and θ_r = 102° ± 1°, respectively.

Then we exposed the PDMS brushes to nitrogen gas with saturated water (to reduce the evaporation of water drop) and saturated vapor (at 20 ± 2 °C, atmospheric pressure) of organic liquids which are not miscible with water, e.g. toluene, n-hexane. The vapor molecules are adsorbed and dissolved in the PDMS brushes (schematic showing in **Figure 3.1a**). As a result of the physisorbed vapor molecules, the brushes swell. In addition, the advancing contact angle decreased to 102° ± 1°, while the receding contact angle (101° ± 1°) changed little (**Figure 3.1b**). The resulted contact angle hysteresis of water in the presence of vapor decreased to 1°, while it

was 4° in air. Furthermore, we found that the sliding ability of water drop is highly dependent on the applied vapor (**Figure 3.1c**). In the air and ethanol vapor, a water drop (10 μL) pinned at a tilted angle α = 3°. In contrast, in the presence of toluene and n-hexane vapors, water drops start moving rapidly at this tilt angle. The vapor of hexane and toluene works as lubrication to accelerate the drop sliding.

To investigate the effect of different solvent vapor on the lubrication performance, we measured sliding angles of water drop with volume of 5 μL and 10 μL in air and vapors of n-hexane, toluene, cyclohexane (CYC), tetrahydrofuran (THF), dimethyl sulfoxide (DMSO), and ethanol (**Figure 3.1d**). The presence of the vapor drastically changes the lateral adhesion of water drops. All vapors reduce the sliding angle, except for ethanol. The lubricating effect of the solvent vapor roughly correlates with the difference of solubility between solvent and PDMS (**Figure S3.7**, **Appendix I**).[230] The lower the difference in solubility parameter, the lower the lateral adhesion of water drops. We speculate that the increase in contact angles hysteresis is also related to the miscibility of ethanol with water. The little amount of ethanol absorbed in the PDMS layer will be sucked up by the water drop. Thus, when the drop recedes it leaves behind a ”dry” PDMS brush while at the front the PDMS brush still contains some ethanol and is still lubricated. The high contact angle hysteresis (θ_{CAH} = 11° ± 1°) of water in ethanol vapor leads to an increase in the lateral adhesion (**Figure S3.8**, **Appendix I**). According to Equation 3.1, the adhesion force of a 10 μL water drop on PDMS brushes in ethanol vapor is estimated to be 49 μN, which is much higher than the value in air, 11 μN. As a result, water drops show a bad mobility on PDMS brushes when in ethanol vapor. Moreover, on a low grafting density PDMS brushes, the vapor lubrication effect is also significant. The vapor lubrication decreased the water sliding angle from 10° to 2°, the contact angles hysteresis from 7° to 1° (**Figure S3.9**, **Appendix I**).

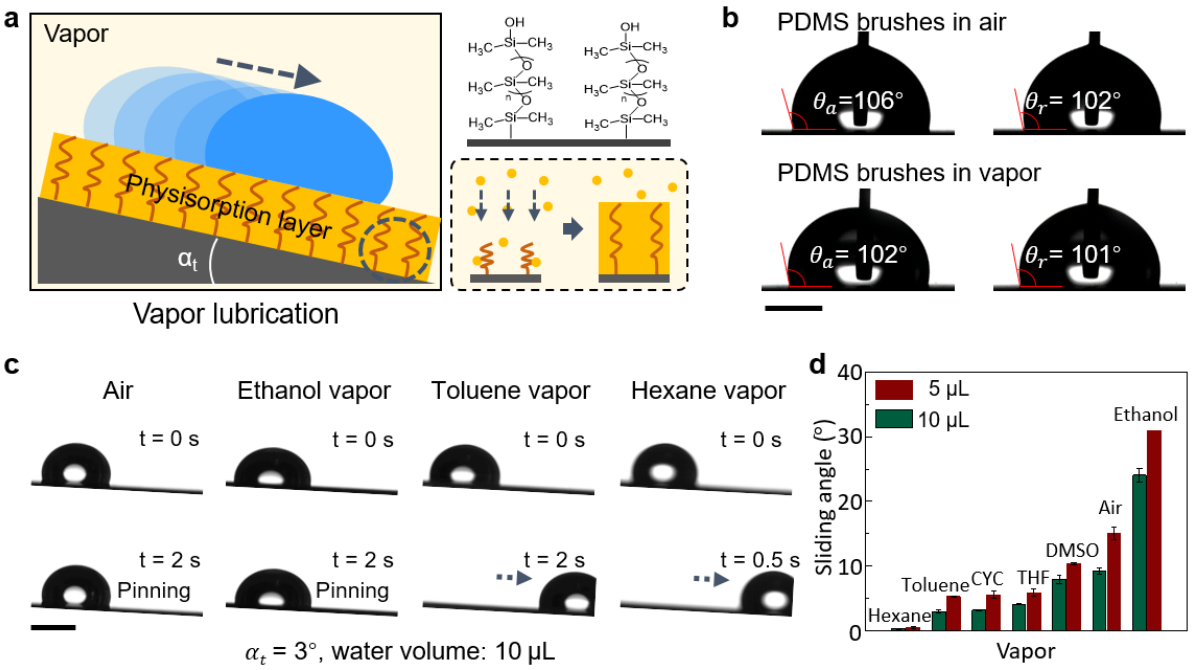

Figure 3.1 Vapor lubrication on PDMS brushes. (a) Schematic of a water drop (blue) on a tilted surface which is coated with PDMS brushes (brown) in the presence of vapor (orange) and adsorbed lubricant layer. The adsorbed vapor leads to a swelling of the PDMS brushes. α_t refers to the tilted angle of the surface. PDMS brushes are not drawn to scale. (b) Advancing contact angle and receding contact angle of a water drop on PDMS brushes in air and vapor environment, respectively. Scale bar: 2 mm. (c) Sliding of water drop (10 μL) on a tilted PDMS brush surface (α_t = 3°) in air and saturated vapors of ethanol, toluene, and hexane. Scale bar: 2 mm. (d) Sliding angles of water drops (5 and 10 μL) on PDMS brushes in various vapors, e.g. hexane, toluene, cyclohexane (CYC), tetrahydrofuran (THF), dimethyl sulfoxide (DMSO), air, and ethanol. All data are presented in mean ± standard deviations.

To further investigate the lubricating effect of organic solvent vapors, we concentrate on toluene as a representative. We characterized the motion of water drops on tilted PDMS brushes in air, vapor, and with an added toluene drop (**Figure 3.2a**). Air or vapor saturated with water or water and toluene were utilized for inhibiting liquid evaporation. For the test of water sliding with an added toluene drop, a toluene drop was placed right next to a water drop on a horizontal PDMS-coated silicon wafer, the drops immediately coalesced followed by toluene forming a wetting ridge around the water drop. [231, 232] The motions of 10 μL water drops on tilted PDMS brushes at α_t =

10° in three environments (**Figure 3.2b**) show that: in air, water drops were pinned on the surface; once assisted by toluene, the water drops slide easily and rapidly on the surface. The reason is that the sliding angles (**Figure 3.2c**) decreased once toluene was introduced. For 1 μL water drop as an example, the sliding angle on PDMS brushes in the presence of air, toluene vapor, and with a toluene drop of ≈40°, ≈12°, ≈2°, respectively. When increasing the volume of the toluene drop from 1 μL to 10 μL, the sliding angle only showed a slight decrease from 2° to 1°, which is primarily caused by the increased volume of the coalesced drop.

A vapor-induced change in sliding angle was also observed on other surfaces (**Figure 3.2c**). For example, on a wafer coated with PFDTS, the sliding angle for 10 μL water drops was 40°. It decreased to 27° from air to saturated toluene vapor. The reduced effect is caused since a real lubricating layer is missing. With an added 10 μL toluene drop on the PFDTS coated surface, the sliding angle of water decreased to ≈14°.

The displacement (d') of the water drops (10 μL) on PDMS brushes in toluene vapor and assisted by a toluene drop (3 μL) were very similar (**Figure 3.2d**). The displacement changes linearly with time (t) in both cases, which is independent with the size of water drop (**Figure S3.10**, **Appendix I**). The drops reached a steady state velocity within less than 0.1 s. The slopes reflect the sliding velocity of water drop, where $v = d'/t$. Therefore, water drops sliding in toluene vapor has much closed velocity compared to that with a toluene drop. We systematically measured the sliding velocities of water drops of different volume on PDMS surfaces assisted by different amounts of toluene ($V_{toluene}$) at tilt angles of α_t = 10° (**Figure 3.2e**). The water drops obtained higher mobility on PDMS brushes in toluene vapor when compared to that in air, especially in high water volume region. The sliding velocity of water drop changes from 0.3 mm·s^{-1} in air to 10 mm·s^{-1} in toluene vapor and to 25 mm/s when V_{water} = 10 μL. It suggests that vapor lubrication has reduced the lateral adhesion of water drops compared to that in air, even though it is still not as good as that assisted by toluene drops.

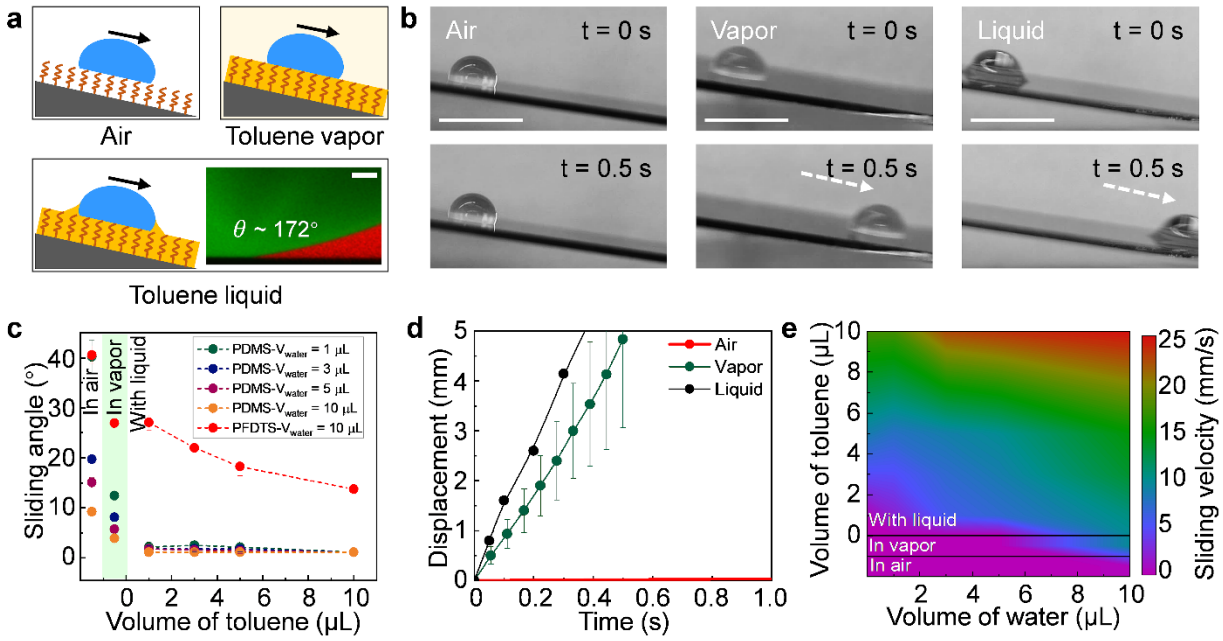

Figure 3.2 The sliding dynamics of the water drop on PDMS brushes in various conditions. (a) Schematics illustrate the sliding characteristics of water drops on tilted PDMS brushes in air, vapor, and with an added toluene drop. PDMS brushes are not drawn to scale. Inset: Image taken by confocal microscopy showing the interface between water, toluene and the surface. (b) Images showing the sliding of water drop (10 μL) on the surface in three environments with α_t = 10°. Scale bar: 2 mm. (c) Sliding angles of water drop (1 μL, 3 μL, 5 μL, and 10 μL) on PDMS brushes in air, toluene vapor and with a toluene drop (1 μL, 3 μL, 5 μL, and 10 μL). (d) Displacement of a sliding water drop in different conditions. (e) Velocities of water drop (V_{water} = 10 μL) on PDMS brushes (α_t = 10°) in three surroundings. The diagram was established based on the measured points. All data are presented in mean ± standard deviations.

To verify the PDMS brushes can be swelled by the adsorbed vapor, we measured the brush thickness by atomic force microscopy (AFM). The thickness of PDMS brushes was deduced from force curves monitored during the tip approach (**Figure 3.3a**). [233] When the AFM tip gets into contact with the PDMS layer, it is wetted by the PDMS. As a result, capillary forces pull the tip towards the substrate until it contacts the hard substrate (**Figure 3.3d**). The same capillary attraction pulls the tip downwards in the presence of the toluene vapor. In this case the cantilever

is bend so much that the spring force balances the capillary force (**Figure 3.3b**). For this reason the tip does not immediately jump into contact with the hard substrate. Once the tip is in contact with the hard substrate it follows the up-and-down movement of the sample stage of the AFM. We take the jump distance as a measure of the thickness of the brush layer. It is, however, only an estimate because of two effects. First, the jump may occur slightly before the tip touches the brush surface because of van der Waals attraction. Second, since the PDMS chains are covalently attached to the Si wafer, some chains may still remain between tip and substrate even at a high force. While the first effect leads to a larger jump distance, the second effect reduces the jump distance.

When fully submerging the brush and tip in toluene, the tip gradually approached the substrate from a distance of 7.7 nm without a jump (**Figure S3.11**, **Appendix I**). We did not detect a clear interface between toluene liquid and toluene-PDMS brushes mixture.

By comparing force curves in air and toluene vapor, we obtained direct evidence that the PDMS brush swells in toluene vapor and the layer thickness increases (**Figure 3.3c-g**). In air, the tip moves at a negative force over a few nanometers until it touches the substrate, indicating a PDMS brushes layer of several nanometers (**Figure 3.3c** and **d**). In toluene vapor, the tip undergoes a longer distance at negative force due to the swelling PDMS brushes layer (**Figure 3.3e** and **f**). After measuring the thickness of PDMS brushes at 100 positions for each condition, average values of the brush thickness were obtained (**Figure 3.3g** and **Figure S3.12**, **Appendix I**). The brush thickness changed from 4.4 ± 0.4 nm in air to 10.8 ± 1.6 nm in toluene vapor.

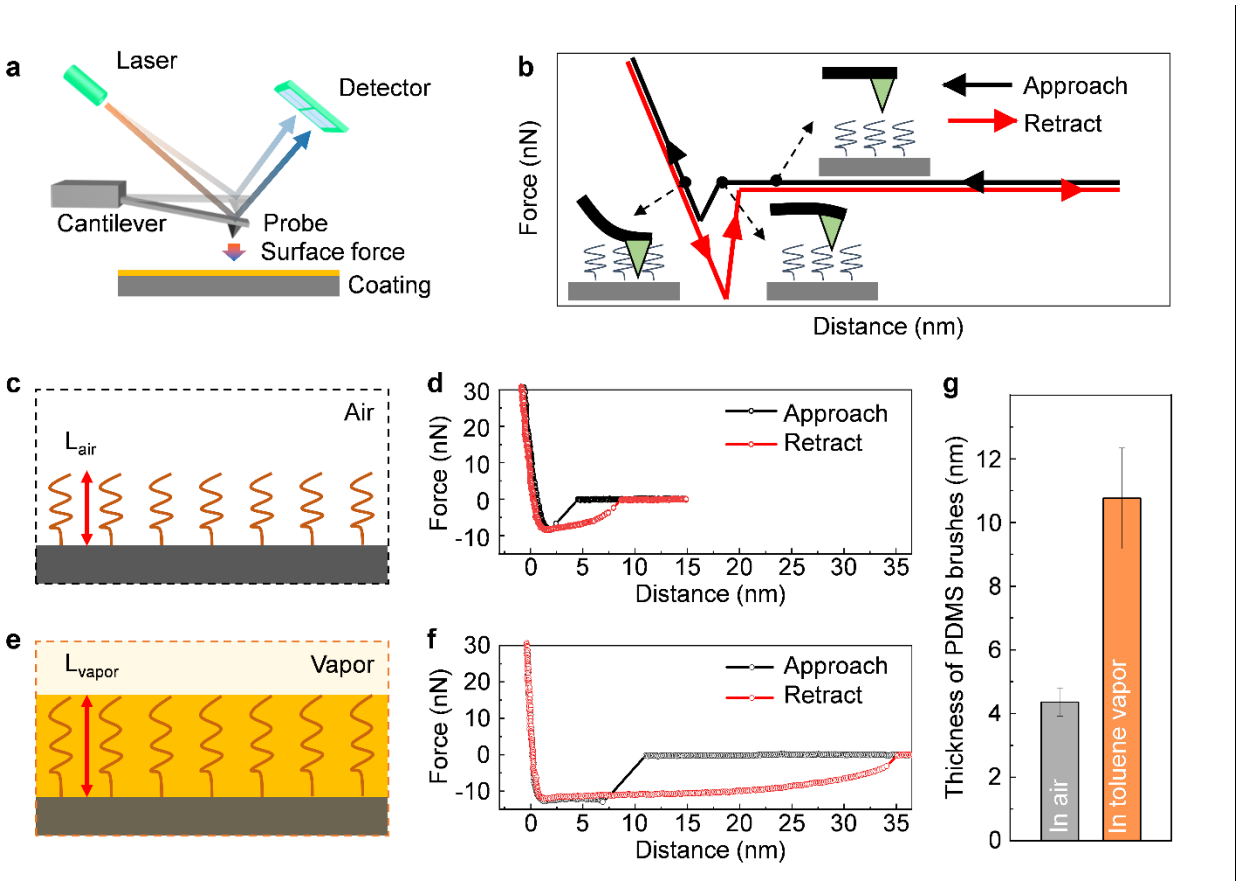

Figure 3.3 Characterization of the thickness of PDMS brushes. (a) Schematic illustration of an AFM system for surface force measurement. (b) Schematic illustrates the state of the AFM cantilever and tip corresponding to the force curve. (c) Schematic image showing the state of PDMS brushes in air, and d) representative force curves measured by the AFM for PDMS brushes in air. PDMS brushes are not drawn to scale. (e) Schematic image showing the state of PDMS brushes in toluene vapor, and (f) representative force curves measured by the AFM for PDMS brushes in toluene vapor. (g) The thickness of the PDMS brushes layer in air and toluene vapor. All data are presented in mean ± standard deviations.

Accelerating drop departure from surfaces even for small drops is essential for enhancing liquid condensation and heat transfer. [26, 111, 114, 210, 211] To test the condensation rate, we used a custom-built chamber (**Figure S3.1a**, **Appendix I**) to cool the PDMS brushes at 11 ± 1 °C. A stream of humid nitrogen gas (mass flow rate: 5 L·min^{-1}) with toluene vapor (details given in Experimental) was input for condensation. Condensed water drops slid at a smaller size assisted by toluene on a vertical PDMS brushes (**Figure 3.4a**). As a result, the average drop departure radius in toluene

vapor was 0.21 ± 0.02 mm, which is less than half of that on PDMS brushes in air (0.44 ± 0.04mm) (**Figure 3.4b**). A water harvest test shows that water collection efficiency in toluene vapor was improved (**Figure 3.4c**). According to the final size of condensed droplets obtained from the video, we calculated the total volume of collected water by a spherical drop model and thus its mass. The linearly growing mass of collected water implies constant water harvesting rates for surfaces in both conditions. Compared with the case in air, the water collection rate in toluene vapor increased by ≈65%, which is ≈700 $g \cdot m^{-2} \cdot h^{-1}$. It is the small departure droplet radius in toluene vapor led to an early shedding of water drops from the surface and thus more room for newly condensing drops.

Vapor can also be used to control the motion of drops.[234, 235] A 20 μL water drop was placed onto a 3° tilted PDMS brushes surface (**Figure 3.4d**). In air, it pinned without sliding (t < 1.5 min). When exposed to toluene vapor, the drop started to move on the surface (t = 1.5 min). After stopping the toluene vapor input, the water drop pinned again on the surface (t = 2 min). The sliding process can be repeatedly controlled by the appearance or disappearance of toluene vapor.

In addition to reducing the liquid lateral adhesion, toluene vapor also reduced ice adhesion to PDMS brushes (**Figure 3.4e-g**). The ice (50 μL) was formed after depositing a water drop on the PDMS brushes and cooling the surface. In air, the ice stickled to the surface even when turning it vertically without moving under its own weight. However, in the presence of toluene, the ice detached from the surface within 0.5 s. This decreased ice adhesion is mainly caused by the lubrication of the toluene vapor adsorbed by the PDMS brushes layer. The lateral ice adhesion strength was further quantified by a typical ice-adhesion characterization system (**Figure S3.1b**, **Appendix I**).[213, 236 67, 237] As shown in **Figure 3.4g**, the ice adhesion strength of 35 ± 7 kPa was obtained on the surface in air. Once introducing toluene vapor, the adhesion strength decreased below 5 kPa. The absolute number of the adhesion force should not be overrated. Since the force

transducer applies the force at a certain height, also vertical forces are exerted which may influence the result.

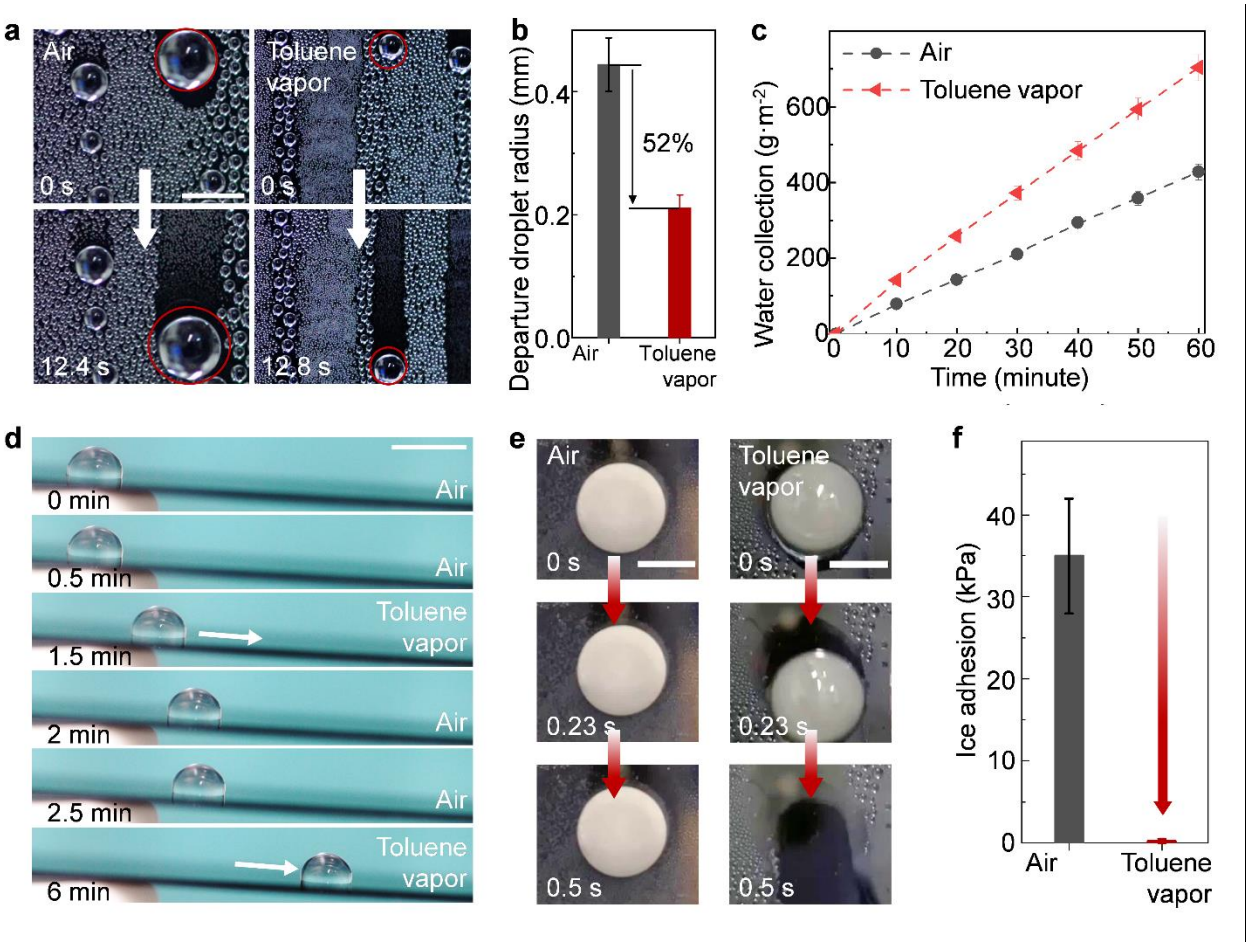

Figure 3.4. Applications of vapor lubrication. a) Photographs showing the departure of drops on PDMS brushes in air and toluene vapor. Scale bar: 1 mm. b) Departure size of condensed water on PDMS brushes in air and toluene vapor. c) The evolution of collected water during condensation with and without toluene vapor. d) Time-lapsed photographs showing the controlled motions of water drop (20 µL) on the tilted PDMS brushes (α_t = 3°). Scale bar: 5 mm. e) Photographs showing the motion of an ice drop (150 µL) on PDMS brushes in air and in toluene vapor environment. Scale bar: 5 mm. f) The lateral ice adhesion strength of a frozen water drop (50 µL) on PDMS brushes in air and in toluene. All data are presented in mean ± standard deviations.

For practical applications, the strategy to use a vapor to form a lubricating layer is only applicable in closed chambers. Otherwise the vapor molecules which are adsorbed by the PDMS brushes

would evaporate to the open environment. A possible application, where this condition is fulfilled is to coat the inside of pipelines with PDMS brushes coating. The aim is to prevent ice/hydrate formation and blocking of the pipeline. Natural gas consists of methane in addition to small amounts of other alkanes. Specifically, the methane inside the pipe would be adsorbed by the PDMS brushes and would act as a lubricant, thus the surface would be easier to repel ice. This is the similar case as we demonstrated here using toluene. Because of the low lateral adhesion, the ice/hydrate would be easily removed by the moving fluid.

3.4 Conclusions

In summary, we demonstrated how the lateral adhesion of water and ice to PDMS brushes can be reduced by the exposure to organic vapors. As confirmed by AFM, vapor molecules are adsorbed into the PDMS, swell the brushes and form a lubricating layer. Using vapor adsorption, the sliding angle for water drops can be reduced, and the slide velocity of water drops increases, leading to its wide potential applications. With the departure volume of water drops being reduced by an order of magnitude with the assistance of toluene vapor, the water collection efficiency of condensing water drops was increased by ≈65% when compared to air. Furthermore, drop mobility can be manipulated by the presence of vapor. In the presence of organic vapor, the PDMS brushes show strong anti-icing properties by significantly reducing the lateral adhesion of ice. This provides a strategy to help solving the freezing-induced block of natural gas pipelines in winter.

3.5 Appendix I

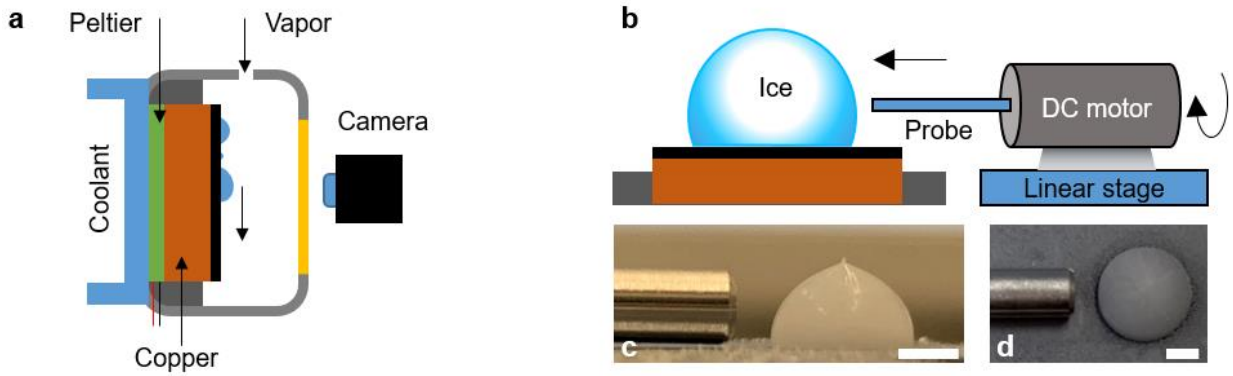

Figure S3.1 (a) The custom-built chamber for condensation measurements with a subcooling of 10 K. (b) Schematic setup for ice lateral adhesion measurements at -25 °C. Side image (c) and top image (d) of probe-to-water contact. Scale bar: 2 mm. Water drops of 50 µL were deposited on the surface and frozen. Then, a force probe (sensitivity of 0.01 N, contact point: less than 0.5 mm above the surface) is driven toward the ice drop at 60 µm·s^{-1} until the ice drops completely detached from the surface. Force curves were collected continuously, and the ice lateral adhesion strength is obtained by dividing the maximum forces by the contact area.

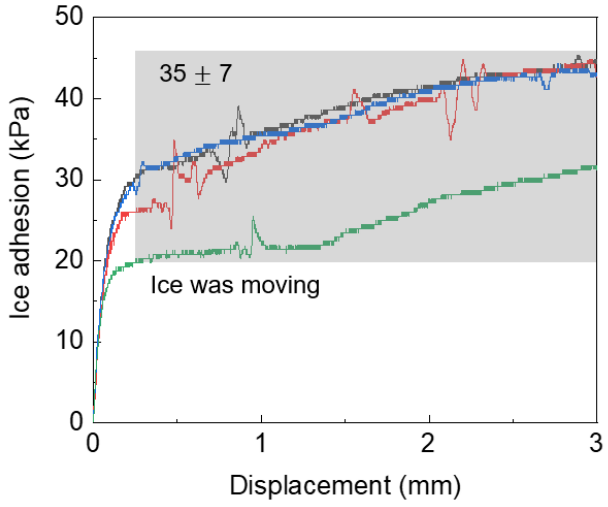

Figure S3.2 Representative curve for ice lateral adhesion measurement without vapor environment. The ice lateral adhesion strength is defined as the adhesion force divided by the contact area.

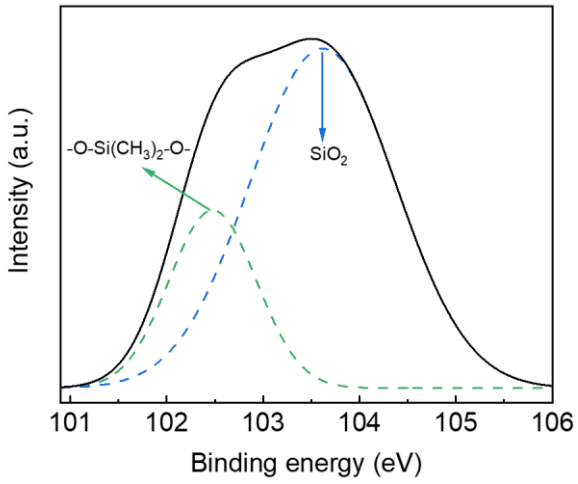

Figure S3.3 Si 2p peaks (black line) measured by X-ray photoelectron spectroscopy of the PDMS brushes on a silicon wafer.

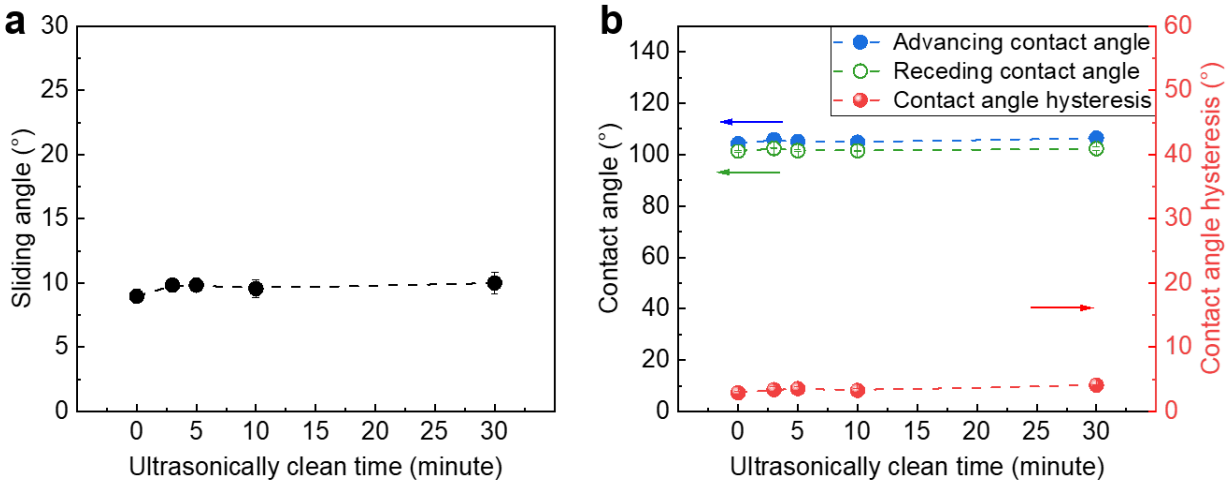

Figure S3.4 Sliding angle (a) and contact angles (b) of water on PDMS brushes after ultrasonically clean in toluene for different times: 3, 5, 10, 30 mintues.

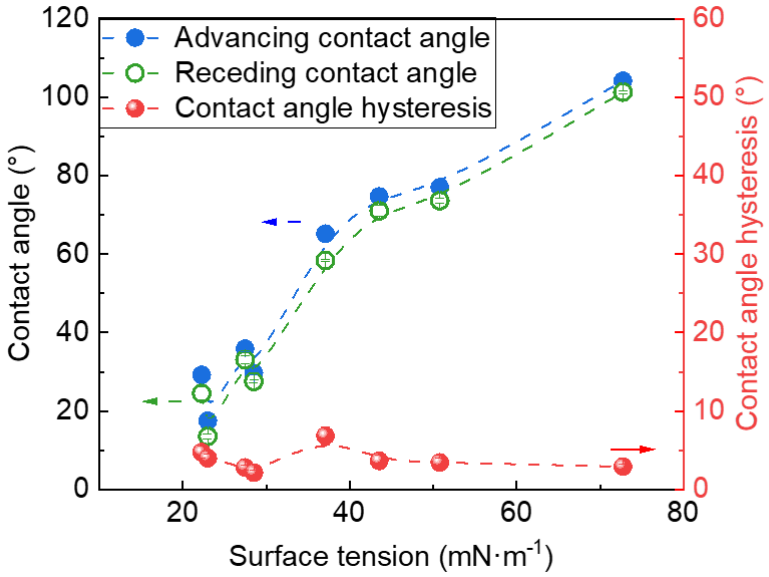

Figure S3.5 Advancing and receding contact angles of various liquid drops on PDMS brushes. Room temperature: 22 °C. The surface tensions of these liquids are as following: Ethanol: 22.4 $mN \cdot m^{-1}$, isopropanol: 23.0 $mN \cdot m^{-1}$, hexadecane: 27.5 $mN \cdot m^{-1}$, toluene: 28.5 $mN \cdot m^{-1}$, dimethylformamide: 37.1 $mN \cdot m^{-1}$, dimethyl sulfoxide: 43.5 $mN \cdot m^{-1}$, diiodomethane: 50.8 $mN \cdot m^{-1}$, and water: 73.6 $mN \cdot m^{-1}$.

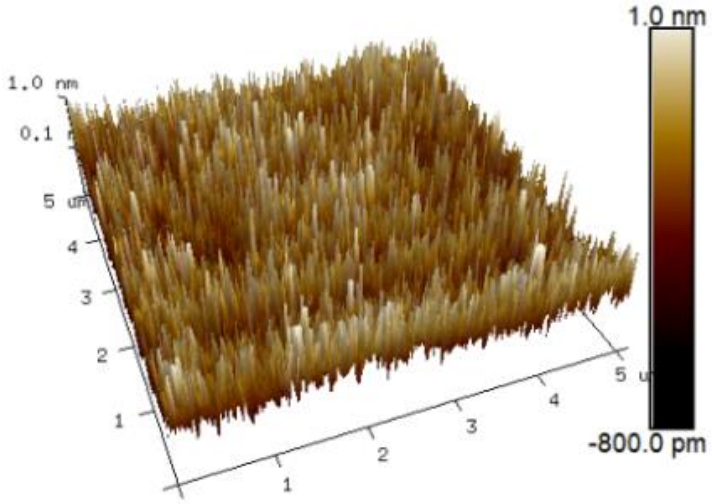

Figure S3.6 AFM image of PDMS brushes on a silicon wafer, the roughness of the surface is ≈1nm.

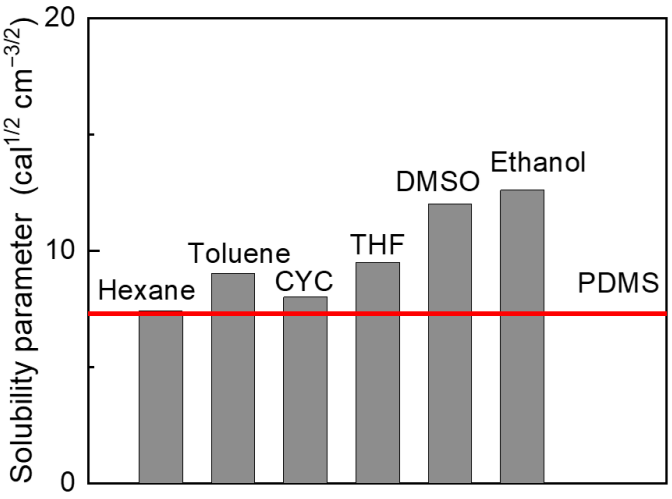

Figure S3.7 Solubility parameter of PDMS brushes, and various solvent, e.g. hexane, toluene, CYC, THF, DMSO, and ethanol.

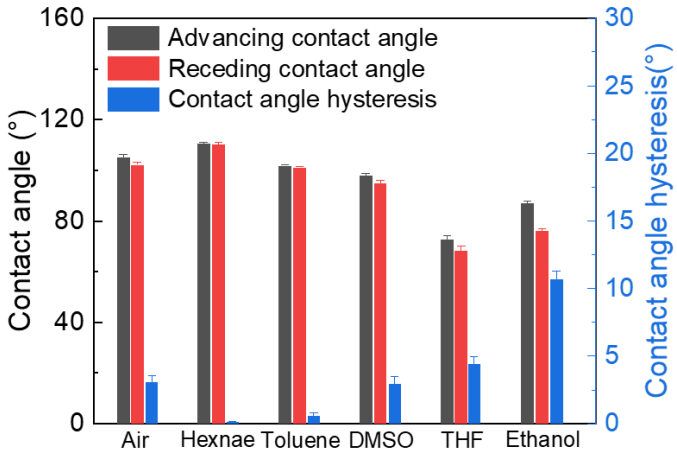

Figure S3.8 Advancing and receding contact angles of water drops on PDMS brushes in different vapor environment: air, hexane, toluene, DMSO, THF, and ethanol.

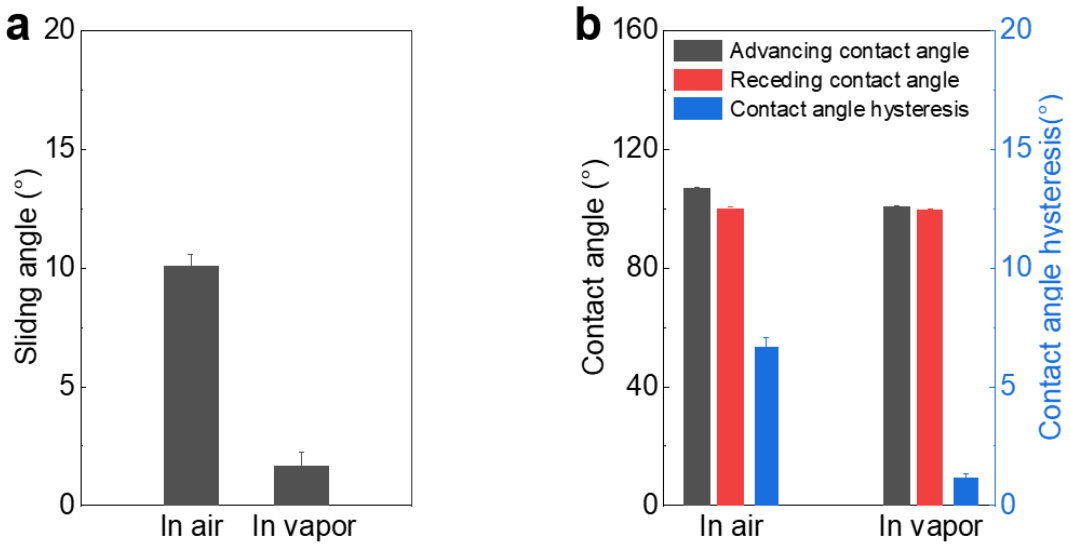

Figure S3.9 Sliding angle (a) and contact angles (b) of water on PDMS brushes by "grafting to" method in air and in toluene vapor environment.

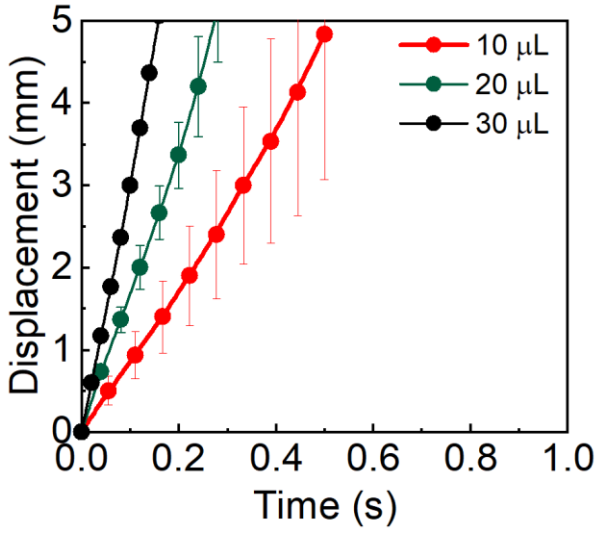

Figure S3.10 Displacement of a sliding water drop (1 μL, 20 μL, and 30 μL) in toluene vapor environment on PDMS brushes.

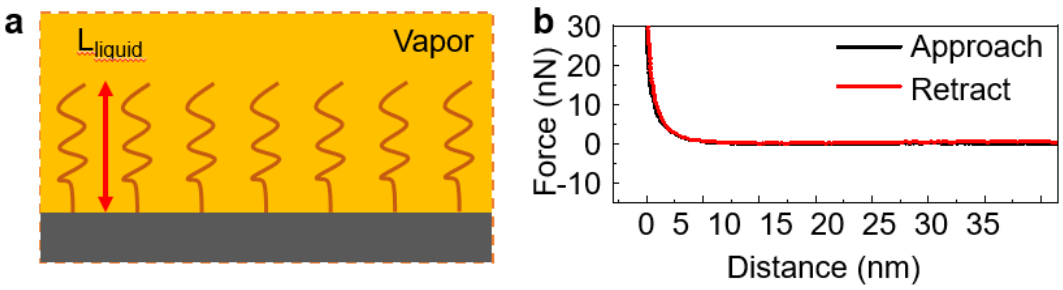

Figure S3.11 Schematic illustration shows the state of PDMS brushes in toluene liquid (a), and representative force curves measured by the AFM (b).

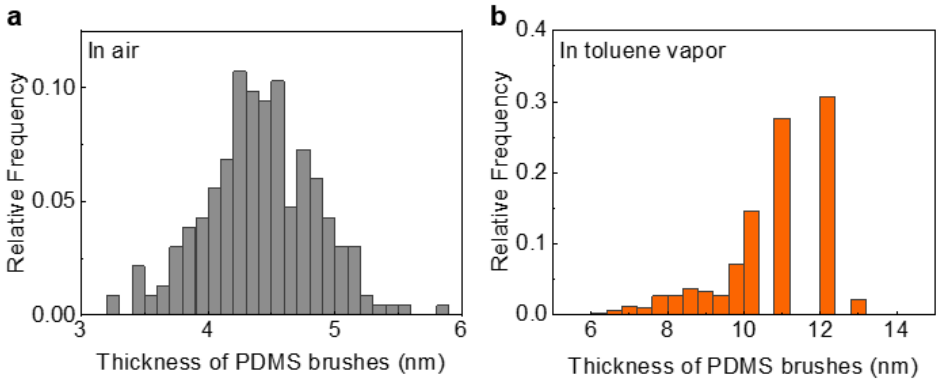

Figure S3.12 (a) Thickness distribution of PDMS brushes in air. (b) Thickness distribution of PDMS brushes in toluene vapor.

4. Organic Vapors Influence Water Contact Angles on Hydrophobic Surfaces§

Fast removal of water drops from solid surfaces is important in many applications such as on solar panels in rain, in heat transfer and for water collection. Recently, a reduction in lateral adhesion of water drops on polydimethylsiloxane (PDMS) brush surfaces after exposure to various organic vapors is reported. It is attributed to the physisorption of vapor and swelling of the PDMS brushes. Behrooz Khatir and Kevin Golovin pointed out that a change in the interfacial energies by vapor adsorption could also have caused low drop adhesion. To find out which effect contributes how strongly, we measured contact angles of water drops on three hydrophobic surfaces in different vapors. In water-soluble vapors, a substantial decrease is observed in contact angles. This decrease can indeed be explained by a vapor-induced change in the interfacial tensions. The very low contact angle hysteresis on PDMS surfaces in saturated n-hexane and toluene vapor cannot be explained by a change in interfacial tensions. The observation supports the hypothesis that these vapors adsorb into the PDMS and form a lubricating layer. We hope these findings help to solve fundamental problems and contribute to applications, such as anti-icing, heat transfer, and water collection.

---

§ This chapter is a slightly modified version of the following article: [238]

Li, S., Butt, H.-J., Organic Vapors Influence Water Contact Angles on Hydrophobic Surfaces. Adv. Mater. **2023**: 2301905. Copyright © 2023 The Authors. Advanced Materials published by Wiley-VCH GmbH, under the terms of the Creative Commons CC BY license.

Author Contributions: Li, S., Butt, H.-J., designed the research and experiments. Li, S. conducted the experiments. Li, S., Butt, H.-J., wrote the manuscript. All authors have given approval to the final version of the manuscript.

4.1 Introduction

The introduction of Young's equation (**Figure 4.1a**) started a quantitative treatment of contact angle phenomena. Young's equation predicts the equilibrium contact angle from interfacial surface energies[1, 239]: $\gamma_{LV} \cos\theta = \gamma_{SV} - \gamma_{SL}$. Here, γ_{LV}, γ_{SV} and γ_{SL} are the liquid-vapor, solid-vapor and solid-liquid interfacial energies, respectively. It can be derived by a force balance: In equilibrium the horizontal forces acting on the contact line need to balance. Despite the fact that Young's equation[64, 240-245] is widely used, little research has been carried out to analyze the effect of the vapor. Boyd and Livingston[240] in 1942, and later Ward and Wu [246] in 2007 pointed out that the adsorption of vapor to the free solid surface is supposed to change contact angles because of the reduction in γ_{SV}. In 1988, Yekta-Fard and Ponter[247] measured no change in water contact angles of water drops on Teflon when they are exposed to the vapor of cyclohexane, decane, or undecane. Several authors[248-251] studied the change of the surface tension of water due to the adsorption of organic vapors.

In many natural phenomena and industrial applications, the sliding of drops on surface is important, such as coatings, [252] energy conversion, [253] and water harvesting, [254] or for glasses or windscreens in rain. In these cases, one needs to discriminate between advancing θ_a and receding contact angles θ_r. The difference between the two is called *contact angle hysteresis*. It can be caused by surface heterogeneity, roughness or adaptation. [8, 255] Contact angles hysteresis is important because it determines the friction force of sessile drops: $F = k\gamma_{LV} w (\cos\theta_r - \cos\theta_a)$. [64, 224, 256] Here, $k \approx 1$ is a shape factor and w is the width of the contact area between drop and solid surface.

Despite remarkable developments, the mechanism for drop mobility on surfaces is far from being understood nor controlled. In this respect, surfaces coated with PDMS brushes have attracted great interest because of their low contact angle hysteresis. [189, 193] In a recent paper, we demonstrated that the contact angle hysteresis of water drops on PDMS-coated surfaces is

further reduced, when the system is exposed to toluene vapor.[209] We explained the effect by the lubricating action of the vapor being adsorbed in the PDMS layer. This hypothesis was supported by an increase of layer thickness in toluene vapor detected by atomic force microscopy. That polymer brushes adsorb solvent vapors is indeed known.[257]

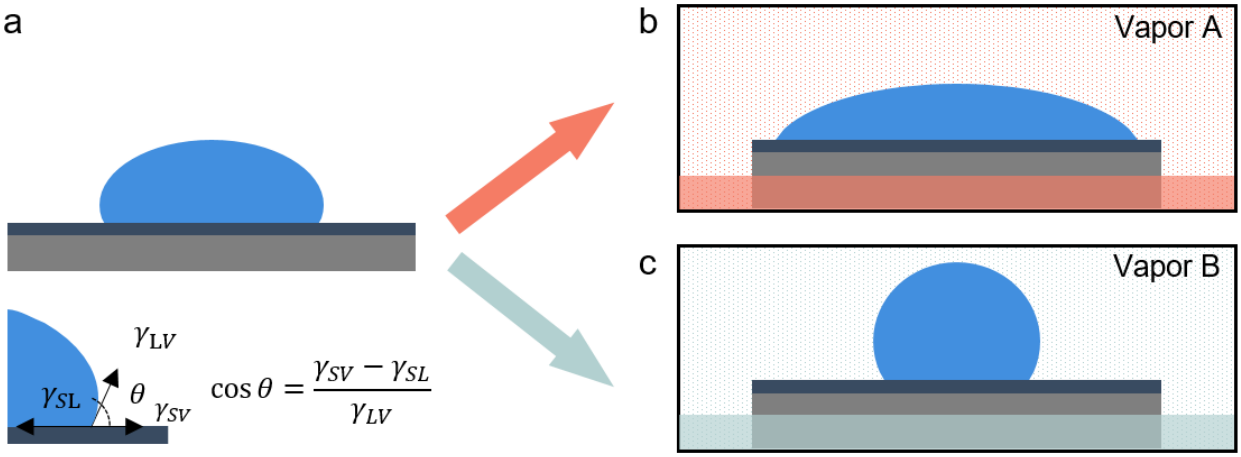

Figure 4.1. (a) Schematic of a sessile water drop on a solid surface and Young's equation. (b, c) Schematically showing a possible change of contact angles after exposing the surface to different vapors.

Khatir and Golovin commented that the same reduction in contact angle hysteresis can be explained simply by a change in γ_{LV}, γ_{SV} and γ_{SL}.[30] As a result, the force balance at the contact line and the contact angles change. It is indeed known, that when exposing water to the vapor of an organic liquid, its surface tension changes due to adsorption and enrichment of the organic molecules.[248, 258-260] That vapor adsorbs to the free solid surface and may decrease γ_{SV} is also known.[240] The comment motivated us to study more in general the effect of organic vapors on contact angles and contact angle hysteresis of water drops on hydrophobic surfaces. We try to answer three questions: How do water contact angles change in different organic vapors (**Figure 4.1b,c**)? Can these changes be explained by changes of the interfacial energies? Can a change in γ_{LV}, γ_{SV} and γ_{SL} explain the low contact angle hysteresis observed on PDMS in *n*-hexane, cyclohexane, and toluene vapor?

4.2 Results and Discussion

To answer the questions, we measured the water contact angles on various hydrophobic surfaces in different vapor environments. As representatives, we choose three hydrophobic surfaces (**Figure S4.1**, **Appendix II**); all surfaces were made as described in the literature: [209, 261] (1) PDMS -coated silicon wafers. Briefly, PDMS was grafted by immersing the silicon wafer into a solution which contained 40 mL toluene (with saturated water) and 1.4 mL dimethyldichlorosilane. (2) PFDTS (1H,1H,2H,2H-perfluorodecyltrimethoxysilane)-coated silicon wafers. PFDTS was coated using a chemical vapor deposition method, by putting silicon wafers into a vacuum desiccator (30 mbar) with 20 µL 1H,1H,2H,2H-perfluorodecyltrimethoxysilane added in the bottom for 3 h. (3) Teflon AF(amorphous fluoropolymer) on gold was prepared by dip coating; the sputter-coated gold glass slides were withdrawn from the solution (1 wt% Teflon AF1600 in perfluorotributylamine) at a constant speed of 10 $mm \cdot min^{-1}$. See **Appendix II** for preparation details. To suppress electrostatic effects, all substrates have a high dielectric permittivity or a conductive layer underneath. The root-mean-square surface roughness of all surfaces as measured by atomic force microscopy was less than 1 nm. As vapors we used *n*-hexane, cyclohexane (CYC), toluene, dimethylsulfoxide (DMSO), ethanol, and tetrahydrofuran (THF). DMSO, ethanol, and THF are miscible with water. *n*-Hexane, CYC, and toluene are immiscible and only dissolve to a low concentration in water; the saturation concentrations are 9.5 ppm, 55 ppm, and 515 ppm, respectively. [262-265]

To measure water contact angles in vapor environment, we used a goniometer (OCA 35, DataPhysics Instruments) equipped with a custom-made closed metal chamber (**Figure S4.2**, **Appendix II**), where two glass windows are inserted for visualization. The solvent was inserted at the bottom of the chamber. Inside the chamber, the surface was mounted in a way that it did not get into direct contact with the liquid solvent. The chamber was sealed for more than 10 minutes before conducting contact angle measurements to generate a stable vapor atmosphere.

Videos of sessile drops in side view were recorded when changing water volume gradually (1 $\mu L \cdot s^{-1}$) between 5 and 20 µL using a motorized Hamilton syringe. Advancing and receding contact angle were determined by fitting an ellipse model to the contour images.

When exposing water drops to vapor of cyclohexane or toluene, the advancing and receding contact angles did not change significantly (**Figure 4.2a**). In hexane they increased slightly (≈4°). When using soluble vapors the contact angles decreased. The higher the saturation vapor pressure the more the contact angles decreased (**Table 4.1**). For example, the advancing contact angles on a PDMS surface in hexane vapor and air were 110° and 106°, respectively, while it was only θ_a^v = 87 and 73° in ethanol and THF vapor, respectively.

To answer the second and third questions, we measured the surface tension of water in different vapors using the pendent drop method (DSA100E, Krüss). [266, 267] To generate a saturated vapor environment, the liquid was inserted at the bottom of a custom-made closed metal chamber (**Figure S4.2**, **Appendix II**). After waiting 10 min to reach saturation, a hanging water drop was introduced and imaged in side view. Real-time results were obtained every second by fitting the drop shape with the Laplace equation with the density of water using a built-in program. We report the water's surface tension 2 min after placing the drop into the chamber (**Table 4.1**). 2 min is the same time delay as used for contact angles measurements.

The surface tensions of water drops in ethanol, THF, and DMSO vapors vapor decreased to 37 $mN \cdot m^{-1}$, 36 $mN \cdot m^{-1}$, and 58 $mN \cdot m^{-1}$, respectively. These values are lower than the ones in *n*-hexane, cyclohexane, and toluene vapors, which were 67 $mN \cdot m^{-1}$, 69 $mN \cdot m^{-1}$, and 63 $mN \cdot m^{-1}$, respectively. The low effect in DMSO vapor is attributed to the low saturation vapor pressure of DMSO.

Table 4.1. Liquid and vapor properties at room temperature (23 °C ± 2 °C). [268-271]

	Saturated vapor pressure (kPa)	γ_{LV} of pure liquid ($mN \cdot m^{-1}$)	γ_{LV} in the vapor after 2 min ($mN \cdot m^{-1}$)	Hansen solubility parameters ($cal^{1/2} \cdot cm^{-3/2}$)
Water	3.17	72	72 ± 1	23
n-Hexane	20.4	18	67 ± 1	7
Cyclohexane	13.0	26	69 ± 1	8
Toluene	3.79	28	63 ± 1	9
DMSO	0.08	43	58 ± 2	13
Ethanol	7.91	22	37 ± 4	13
THF	21.6	26	36 ± 1	10

To answer the second question, we first analyze which effect a change of γ_{LV} has, by keeping all other interfacial energies constant. Which contact angle is expected, if γ_{LV} changes from the value in air to the one measured in vapor while keeping γ_{SV} and γ_{SL} constant? To answer this question, we compare the experimental mean contact angles (**Figure S4.3**, **Appendix II**) with contact angles predicted by Young's equation. "Mean" contact angles refers to the mean of the cosines: $\cos\theta = (\cos\theta_a + \cos\theta_r)/2$. In a strict sense Young's equation is only valid in equilibrium. Thus, we assume that the mean contact angle is an approximation for the equilibrium value. Applying Young's equation to the mean contact angle in a vapor leads to $\cos\theta = (\gamma^v_{SV} - \gamma^v_{SL})/\gamma^v_{LV}$, where the superscript "v" indicates "vapor". Assuming that $\gamma^v_{SV} - \gamma^v_{SL} = \gamma^{air}_{SV} - \gamma^{air}_{SL}$, having measured γ^v_{LV}, and with Young's equation applied to the mean experimental contact in air, θ^{air}, we obtain an expected mean contact angle $\cos\theta_{theo} = \frac{72\ mN \cdot m^{-1}}{\gamma^v_{LV}} \cos\theta^{air}$.

The expected mean contact angles (**Figure 4.2b**) agree with measured contact angles (**Figure 4.2a and S4.3**) for *n*-hexane, cyclohexane and toluene within the error of our measurements. This agreement is not surprising, considering that the contact angle were not much affected by the

vapor. Substantial deviations were, however, observed for the soluble vapors ethanol and THF. Plotting the difference between the expected and measured contact angles (**Figure 4.2c**) shows that the measured contact angles tended to be lower than the expected contact angles. In particular, in THF vapor, the measured contact angles were 10 - 23° lower than the calculated ones. Thus, a change from γ_{LV} = 72 mN·m^{-1} to the value measured in vapor γ_{LV}^{v} cannot explain the observed changes in mean contact angles for soluble vapors. We conclude that for soluble vapors the solid-vapor and/or the solid-liquid interfacial energies change upon exposition to the vapor.

To be able to describe the changes in mean contact angles, we need to take into account a change of $\gamma_{SV} - \gamma_{SL}$. In particular, the water-soluble vapors indicate that we need to consider a change of the interfacial energy γ_{SL} due to the enrichment of DMSO, ethanol, or THF at the solid-liquid interface. How big does this difference between $\gamma_{SV} - \gamma_{SL}$ in air and vapor need to be to account for the observed change in contact angles? To estimate this difference, we calculate:

$$\Delta(\gamma_{SV} - \gamma_{SL}) \equiv \left(\gamma_{SV}^{v} - \gamma_{SL}^{v}\right) - \left(\gamma_{SV}^{air} - \gamma_{SL}^{air}\right) = \gamma_{LV}^{v} \cos\theta^{v} - 72\ \text{mN·m}^{-1} \cdot \cos\theta^{air}. \qquad \text{(Equation 4.1)}$$

Here, θ^{v} is the experimental mean contact angle in a specific vapor. On the left side of equation 4.1, all parameters were determined experimentally. As shown in **Figure 4.2d**, $\Delta(\gamma_{SV} - \gamma_{SL})$ in all vapors are positive (except *n*-hexane). Specifically, in ethanol and THF, the value of $\Delta(\gamma_{SV} - \gamma_{SL})$ reaches more than 20 mN·m^{-1}. It is highly unlikely that $\gamma_{SV}^{v} > \gamma_{SV}^{air}$, because a spontaneous adsorption of vapor to the solid surface should decrease the solid-vapor interfacial energy. [240, 246] For this reason, we believe that this increase in $\Delta(\gamma_{SV} - \gamma_{SL})$ is mainly caused by an adsorption of dissolved vapor molecules to the solid-liquid interface, resulting in a decrease of γ_{SL}.

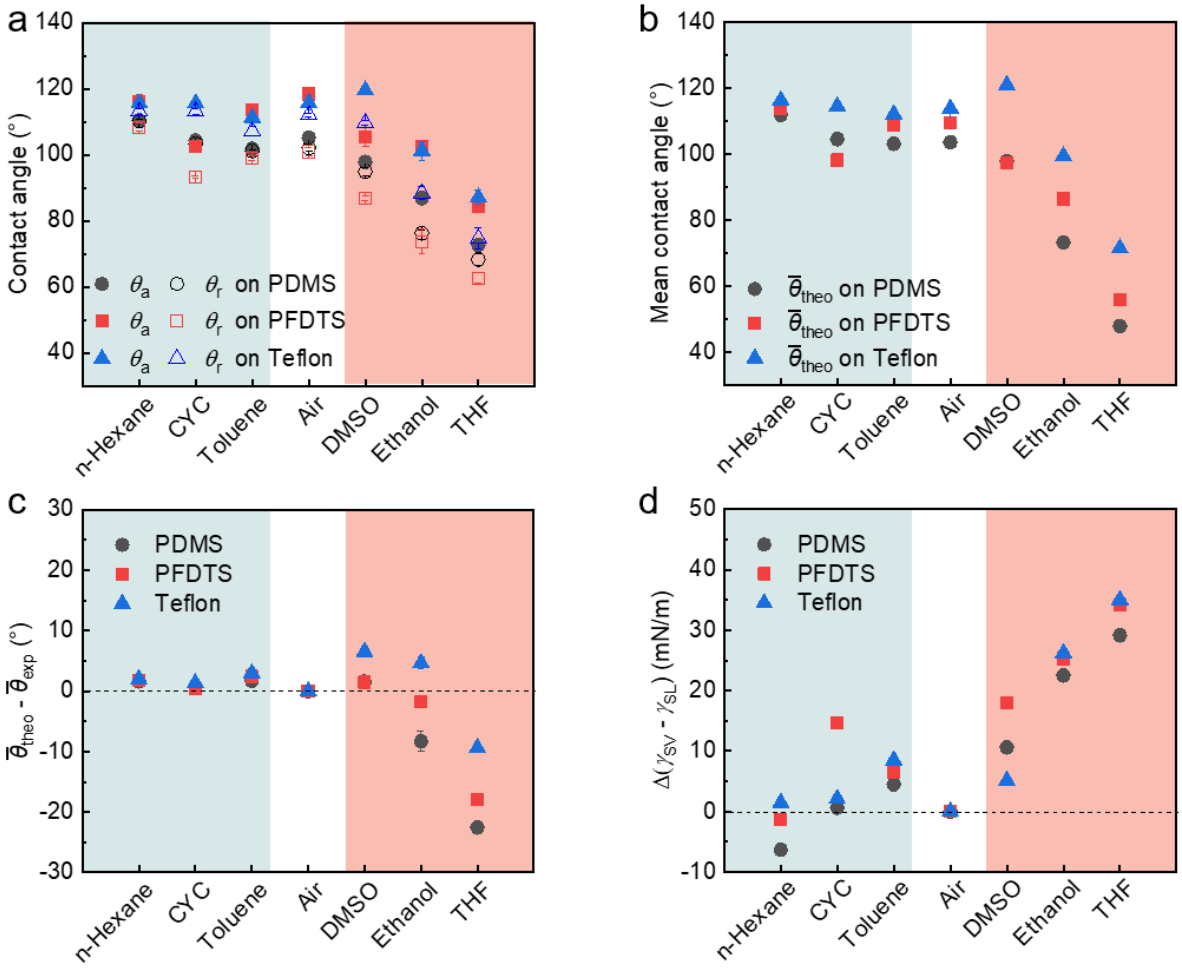

Figure 4.2: Contact angles of water on PDMS-coated surfaces, PFDTS-coated surfaces, and Teflon films in different vapors: *n*-hexane, CYC, toluene, air, DMSO, ethanol, and THF. (a) Experimental advancing θ_a and receding θ_r contact angles. (b) Theoretical mean contact angles calculated with $\cos\theta_{theo} = \frac{72\ mN\cdot m^{-1}}{\gamma^{v}_{LV}}\cos\theta^{air}$. Here, γ^{v}_{LV} is the surface tension of water in the respective vapor and on the respective surface. θ^{air} is the measured mean contact angle in air of the same surface. (c) Difference of expected contact angle (assuming $\gamma^{v}_{SV} - \gamma^{v}_{SL} = \gamma^{air}_{SV} - \gamma^{air}_{SL}$) and the experimental value in the respective vapor and on the respective surface, $\theta_{theo} - \theta_{exp}$. (d) Change of $\gamma_{SV} - \gamma_{SL}$ between in different vapor environment and in air. Green and red shadows denote results in water-soluble vapor and water-insoluble vapor, respectively.

To answer the third question, we investigate contact angle hysteresis in air $\Delta\theta^{air} = \theta^{air}_a - \theta^{air}_r$ and vapor $\Delta\theta^{v} = \theta^{v}_a - \theta^{v}_r$. Here, θ^{air}_a and θ^{air}_r are the measured advancing and receding contact angles

in air. θ_a^v and θ_r^v are the respective contact angles in vapor. Contact angle hysteresis depends on the vapor (**Figure 4.3a, Table S4.1** in **Appendix II**). For the water-soluble vapors, $\Delta\theta^v$ showed a trend to be higher than in air. For the nonsoluble vapors the measured contact angle hysteresis $\Delta\theta^v$ tended to be lower than in air. In particular on the PDMS surfaces much lower contact angle hysteresis was observed than in air.

In an attempt to explain the changing contact angle hysteresis by changing interfacial energies we apply Young's equation locally. We assume that the interfacial energies *close to the contact line* need to be inserted into Young's equation and that the interfacial energies are different for the advancing and receding sides. The assumption of local validity of Young's equation is supported by the fact that just before the drop starts to slide the forces acting on the contact line on the front and rear side are balanced. With this assumption we estimate the "expected" advancing and receding contact angles in the vapor phase $\theta^v_{a,\,theo}$ and $\theta^v_{r,\,theo}$ from the respective advancing and receding contact angles measured in air, θ_a^{air} and θ_r^{air}, by

$$\cos\theta^v_{a,\,theo} = \frac{\gamma_L^{air}\cos\theta_a^{air} + \Delta(\gamma_{SV} - \gamma_{SL})}{\gamma^v_{LV}}, \qquad \text{(Equation 4.2)}$$

$$\cos\theta^v_{r,\,theo} = \frac{\gamma_L^{air}\cos\theta_r^{air} + \Delta(\gamma_{SV} - \gamma_{SL})}{\gamma^v_{LV}}. \qquad \text{(Equation 4.3)}$$

To derive these equations we reason that at the advancing side

$$\cos\theta^v_{a,\,theo} = \frac{\gamma^v_{SV} - \gamma^v_{SL}}{\gamma^v_{LV}} = \frac{\gamma^{air}_{SV} - \gamma^{air}_{SL} + \Delta(\gamma_{SV} - \gamma_{SL})}{\gamma^v_{LV}} = \frac{\gamma_L^{air}\cos\theta_a^{air} + \Delta(\gamma_{SV} - \gamma_{SL})}{\gamma^v_{LV}} \qquad \text{(Equation 4.4)}$$

Here, the interfacial energies in the first two equations refer to the ones close to the advancing contact line. We can write a similar equation for the receding side, assuming that to derive equation 4.3 the interfacial energies close to the receding contact line need to be considered.

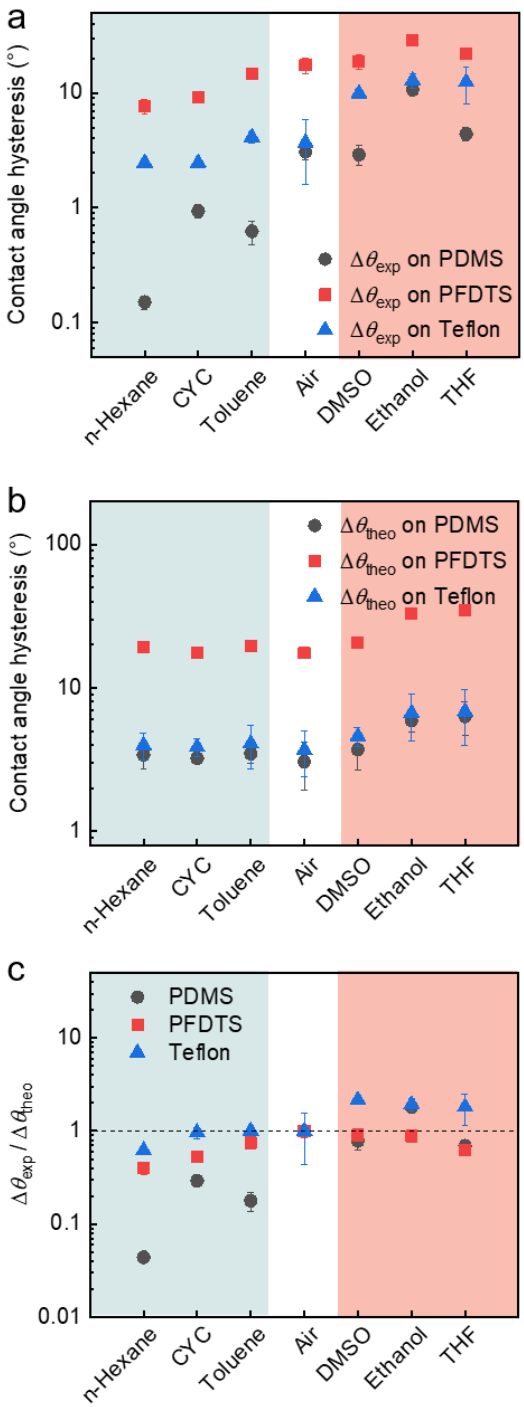

Figure 4.3: Contact angle hysteresis obtained on PDMS-coated surfaces, PFDTS-coated surfaces, and Teflon films. (a) Experimental contact angle hysteresis $\Delta\theta_{exp}$. (b) Theoretical contact angle hysteresis $\Delta\theta_{theo}$ calculated with equation 4.2 and 4.3. (c) Ratio of experimental contact angle hysteresis to theoretical values $\Delta\theta_{exp}/\Delta\theta_{theo}$. Green and red shadows denote results in water-soluble vapor and water-insoluble vapor, respectively.

With equation 4.2 and 4.3 we calculate the expected contact angle hysteresis in vapor (**Figure 4.3b**) and compared it to experimental results (**Figure 4.3c**). Experimental values for the contact angle hysteresis deviated substantially from the calculated values (**Table S4.2** in **Appendix II** for details). For the water-insoluble vapors, the contact angle hysteresis tends to be lower than theoretical values. In particular for the PDMS surfaces, the observed contact angle hysteresis was 71 - 96% lower than the theoretical ones. We attribute these low $\Delta\theta_{exp}$ values to the lubricating effect of the vapor. Vapor is absorbed in the PDMS and lubricates the motion of the contact line.[223, 272] We conclude, that the change of interfacial energies cannot explain the change of contact angle hysteresis. Physisorption into the PDMS plays an important role. This hypothesis is supported by the correlation of $\Delta\theta_{exp}$ with the difference of Hansen solubility parameters[230, 271, 273-277] between the vapor and the PDMS coating ($\Delta\delta = \delta_V - \delta_{PDMS}$). Originally developed to decide if a substance is soluble in another, it has also been successfully applied to indicate the uptake of solvents by PDMS.[230] The lower the difference between Hansen parameters the more vapor adsorbs in the PDMS brush and the lower the contact angle hysteresis become.

4.3 Conclusion

Water advancing and receding contact angles do not change significantly for vapors, which are immiscible with water. In contrast, for soluble vapors we detected a substantial decrease of contact angles. This decrease can be explained by an adsorption of dissolved molecules to the solid-liquid interfaces and the resulting reduction of γ_{SV}. Thus, in accordance with Khatir and Golovin, a change in the mean contact angle can be explained by vapor-induced changes in the interfacial energies. However, the observed decrease in contact angle hysteresis on PDMS cannot be explained by changes in γ_{LV}, γ_{SL}, and γ_{SV}. We attribute them to an uptake of vapor by the PDMS and the formation of a lubricating layer. Our findings are directly relevant to situations

where droplets occur such as water collection, heat transfer, and power generation applications. The insight that background vapor influences drop contact angles may open new avenues for drop manipulation.

4.4 Appendix II

Sample preparation

Three types of surfaces were prepared. (1) PDMS coating on silicon wafers was prepared as described in [188, 209]. After washing ultrasonically in hexane and ethanol, the silicon wafers (Silicon Materials Inc, P type, 100 orientation) were cleaned by oxygen plasma (Diener Electronic Femto, 120W, 6 cm·3 min^{-1} oxygen flow rate) for 5 min. Then, the substrates were immersed in 40 mL toluene (with saturated water) mixed with 1.4 mL dimethyldichlorosilane. After 30 minutes, the wafers were washed with toluene and dried with nitrogen. (2) PFDTS coating on silicon wafers was prepared by chemical vapor deposition. After clean silicon wafers as described before, the wafers were placed into a vacuum desiccator, which contained 20 µL 1H,1H,2H,2H-perfluorodecyltrimethoxysilane at the bottom. Afterwards, the desiccator was evacuated to less than 50 mbar, then closed. After a reaction time of 3 hours, the wafers were taken out and washed by ethanol. (3) Teflon coating on gold was prepared by first cleaning glass slides (Microscope Slides, Epredia) by solvent and plasma as described before[261]. Then 5 nm chromium (to improve adhesion) and 30 nm gold was sputtered onto the glass slides, respectively. To coat Teflon on gold, the substrates were immersed in 1 wt% Teflon AF1600 in perfluorotributylamine (Sigma-Aldrich) for 10 s before withdrawn from the solution at a constant speed of 10 mm·min^{-1}. Afterwards, the substrates were annealed at 160 °C in vacuum for 24 h.

Surface characterization

The morphology/surface roughness of all three hydrophobic surfaces were imaged using an Atomic Force Microscope (JPK Nanowizard 4) in the QI™ mode. Cantilevers (OLTESPA) with a

nominal spring constant of 2 $N \cdot m^{-1}$ and a nominal tip radius of 7 nm were used. The root-mean-square surface roughness was determined on areas of 1 × 1 μm^2.

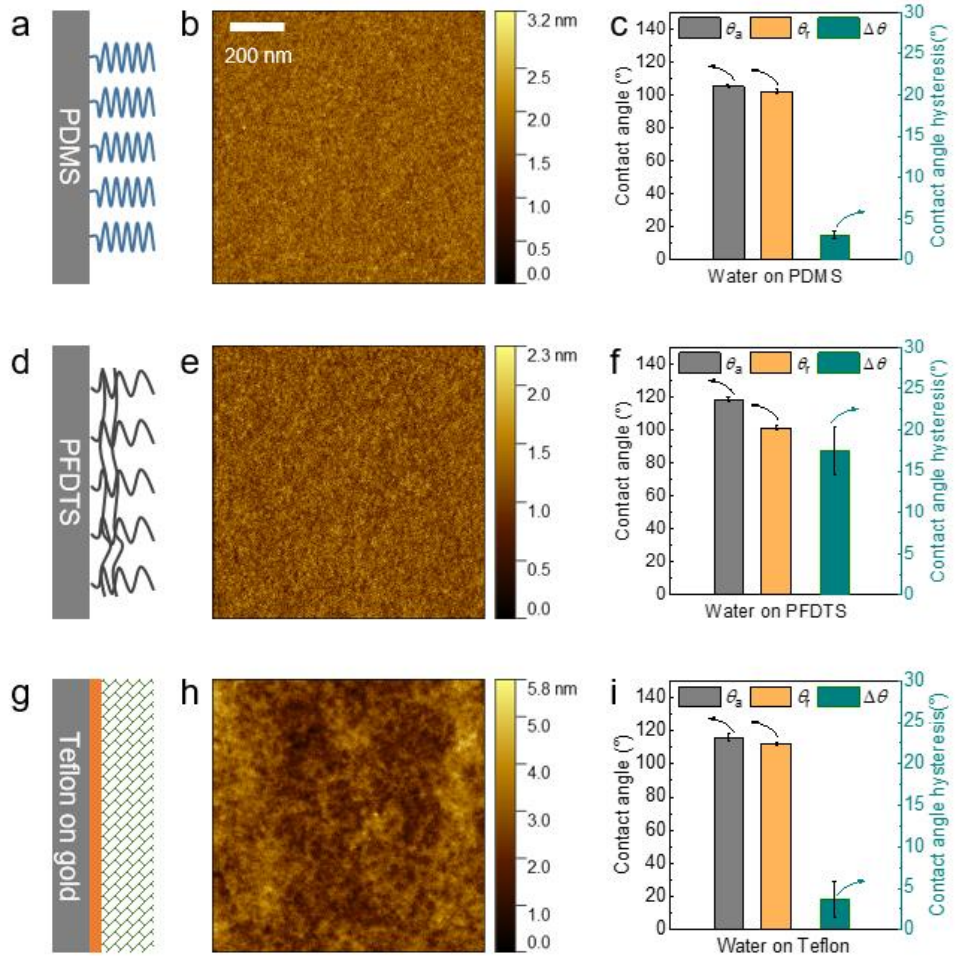

Figure S4.1. Surfaces characterization. Schematic images (a, d, g), AFM images (b, e, h), and water contact angles (c, f, i) for PDMS surface, PFDTS surface, and Teflon surface on gold, respectively.

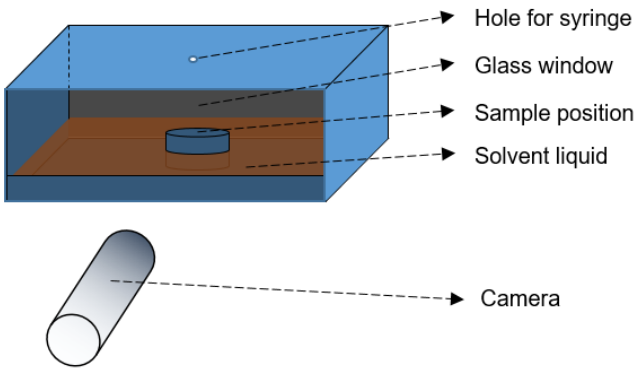

Figure S4.2. Schematic of the chamber for contact angle measurement.

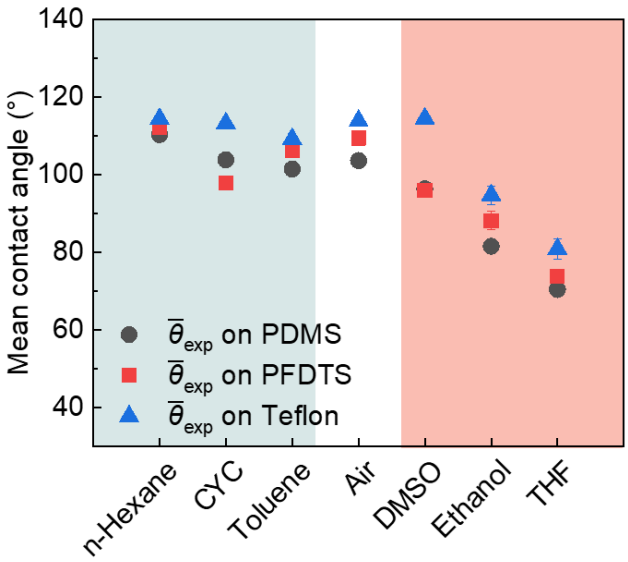

Figure S4.3. Experimental mean contact angles calculated with $\cos\ \theta = (\cos\theta_a + \cos\theta_r)/2$.

Table S4.1. Experimental results obtained on PDMS-coated surfaces, Teflon films and PFDTS coated surfaces. θ_a and θ_r are the water advancing and receding contact angles, respectively.

	PDMS		Teflon		PFDTS	
Vapor	θ_a	θ_r	θ_a	θ_r	θ_a	θ_r
n-hexane	110°± 1°	110°± 1°	116° ± 1°	113° ± 1°	116° ± 2°	108° ± 1°
Cyclohexane	104°± 1°	103°± 1°	116° ± 1°	113° ± 1°	103° ± 1°	93° ± 1°
Toluene	102°± 1°	101°± 1°	111° ± 2°	107° ± 1°	114° ± 1°	99° ± 1°
Air	106° ± 1°	102°± 1°	116° ± 2°	112° ± 1°	118° ± 2°	101° ± 1°
DMSO	98°± 1°	95°± 1°	120° ± 1°	110° ± 1°	106° ± 3°	87° ± 1°
Ethanol	87°± 1°	76°± 1°	101° ± 3°	88° ± 2°	103° ± 1°	74° ± 4°
THF	73°± 1°	68°± 2°	87° ± 2°	75° ± 3°	84° ± 2°	63° ± 2°

Table S4.2. Theoretical contact angles on PDMS-coated surfaces, Teflon films and PFDTS coated surfaces.

	PDMS		Teflon		PFDTS	
Vapor	$\theta_{a,\,theo}$	$\theta_{r,\,theo}$	$\theta_{a,\,theo}$	$\theta_{r,\,theo}$	$\theta_{a,\,theo}$	$\theta_{r,\,theo}$
n-hexane	112°± 1°	109°± 1°	116°± 1°	112°± 1°	122°± 1°	103°± 1°
Cyclohexane	105°± 1°	102°± 1°	115°± 1°	111°± 1°	107°± 1°	89°± 1°
Toluene	103°± 1°	100°± 1°	111°± 1°	107°± 1°	116°± 1°	97°± 1°
Air	105°± 1°	102°± 1°	115°± 1°	112°± 1°	118°± 1°	101°± 1°
DMSO	98°± 1°	95°± 1°	117°± 1°	112°± 1°	106°± 1°	86°± 1°
Ethanol	85°± 1°	79°± 1°	98°± 1°	92°± 2°	105°± 1°	72°± 2°
THF	74°± 1°	68°± 1°	84°± 1°	78°± 1°	90°± 1°	56°± 1°

5. Enhanced Condensation Heat Transfer of Binary Liquids on PDMS Brushes§

Enhancing heat transfer efficiency by liquid condensation plays a critical role in recovering and utilizing low-grade heat. However, overall heat transfer efficiency is commonly limited by the inefficient vapor-liquid phase transition flux and enthalpy during liquid condensation. Here, we report that by introducing driblets of water into the phase-change process of ethanol on a liquid-like polydimethylsiloxane (PDMS) brush surface, the heat transfer coefficient is significantly enhanced, in particular, by more than one order of magnitude compared to the pure ethanol condensation. Such enhanced thermal performance is primarily due to the elaborate balance between promoting condensation, i.e., nucleation and growth, and increasing latent heat by regulating components of water and ethanol, as well as the rapid droplet removal by condensing on the PDMS brushes. Note that the more stabilized dropwise condensation of the binary liquids, retained by accelerating the droplet coalescence velocity, beyond filmwise condensation ensures its significant effectivity under high heat flux.

---

§ This chapter is a slightly modified version of the following article:

Li, S., Diaz, D., Kappl, M., Butt, H.-J., Liu, J., and Hou, Y., Enhanced Condensation Heat Transfer by Water/Ethanol Binary Liquids on Polydimethylsiloxane Brushes. Droplet. **2022,** 1(2): 214-222.
Copyright © 2022 The Authors. Published by John Wiley & Sons Australia, Ltd.

Author Contributions: Li, S., Butt, H.-J., Liu, J., and Hou, Y. designed the research and experiments. Li, S. conducted all the experiments without further statement. Li, S. and Diaz, D. carried out the coalescence velocity of droplets. Li, S., Kappl, M., Butt, H.-J., Liu, J., and Hou, Y., wrote the manuscript. All authors have given approval to the final version of the manuscript.

5.1 Introduction

Vapor condensation is a ubiquitous phenomenon in nature and also an essential process in many industrial applications, e.g. heat pipes, [278, 279] air conditioning, [202, 280] and power generation. [281] Enhancing the condensation performance of liquids would significantly improve the overall thermal efficiency, leading to global energy savings. Dropwise condensation on a solid surface, during which discrete mobile droplets form and are easily shed from the surface by gravity, is a favorable way to improve heat transfer efficiency. [212, 282, 283] To accelerate such a process, a high vapor-liquid phase transition flux on solid surfaces is required, which is commonly achieved by promoting droplet nucleation, growth, and departure (**Figure 5.1**). The rapid droplet departure promotes the overall heat transfer rate by reducing the thermal barrier associated with condensate and clearing the surface for droplet re-nucleation. [26, 111] Besides that, reducing the surface tension of liquids is an efficient approach commonly used to promote condensation. [178, 284-288] However, the condensation of low-surface-tension liquids is typically characterized by the formation of a liquid film that entirely covers the condensing surface since these liquids wet most solid materials with a low contact angle. The liquid film results in high thermal resistance and slows the condensate departure, thereby decreasing the heat transfer coefficient.

In recent years, intensive research has focused on developing advanced omniphobic materials, such as lubricant-infused surfaces[179, 180, 289] and flexible polymer brush coatings, [141, 188, 290] on which dropwise condensation of various liquids is demonstrated. For the common low-surface-tension liquids (e.g., ethanol, hexane, and toluene), the thermal performances of dropwise condensation on omniphobic surfaces are superior to those of filmwise condensation. However, efficient heat transfer requires not only rapid droplet nucleation and departure, but also a high enthalpy of condensation (i.e., latent heat of vaporization). For low-surface-tension liquids, the low latent heat of vaporization and thermal conductivity greatly limit the thermal performance of phase change (**Figure S5.1, Appendix III**). The condensation heat transfer coefficient of ethanol,

a representative low-surface-tension liquid (with surface tension of 22.8 $mN \cdot m^{-1}$), was only 10-20 $kW \cdot m^2 \cdot K^{-1}$, as much as 30% to 70% lower than that of pure water. [178, 289, 290] Therefore, displaying high vapor-liquid phase transition flux and stable dropwise condensation on a solid surface while balancing the vaporization latent heat are dominant for improving heat transfer efficiency.

In this work, we report a significant heat transfer enhancement by introducing a small portion of water into the condensation process of ethanol on an omniphobic PDMS brush surface. The binary liquids increased the latent heat without diminishing the low-surface-tension properties of condensate, therefore gaining the advantages of high nucleation density, fast growth rate, and rapid droplet shedding. In addition, the binary liquids accelerated the relaxation of coalescing droplets, which effectively stabilized the dropwise condensation under high heat flux. As a result, the binary condensation of ethanol-water mixtures achieved an 1800% higher heat transfer coefficient on the PDMS brush surface when compared with the ethanol condensation. Our experimental results reveal a previously unnoticed correlation between droplet coalescence hydrodynamics and the optimal thermal performance of low-surface-tension liquids, which can shed more light on the phase change process and associated heat transfer applications.

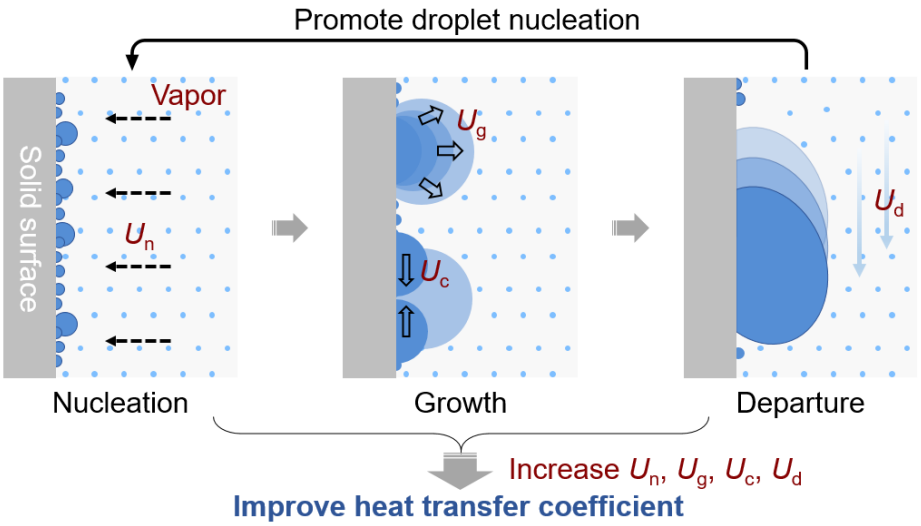

Figure 5.1 Overview of factors promoting heat transfer coefficient. U_n, U_g, U_c, U_d respectively represent the rate of liquid nucleation, growth, coalescence, and departure on a solid surface.

5.2 Experimental

Surface Preparation. PDMS brushes: Silicon wafers (Silicon Materials Inc, P type, <1 0 0> orientation) were ultrasonicated in toluene (98%, Sigma) and ethanol (99.5%, Sigma) for 5 minutes, respectively, and dried with nitrogen. Then the substrates were cleaned with oxygen-plasma (Diener Electronic Femto, 120W, 6 $cm^3 \cdot min^{-1}$ oxygen flow rate) for 5 minutes and immersed in a mixture of 40 mL toluene (with saturated water) and 1.4 mL dimethyldichlorosilane. After 0.5 h, the substrate was taken out, washed with toluene and dried with nitrogen.

Fluorinated surface: Silicon wafers were washed ultrasonically for 5 minutes with toluene and ethanol, as described above. Afterwards wafers were treated with 120 W oxygen-plasma for 5 minutes before being placed into a vacuum desiccator with ≈20 µL of 1H, 1H, 2H, 2H-perfluorodecyltrimethoxysilane added in the bottom of the desiccator. Then the desiccator was evacuated to ≈10 mbar. The reaction lasted for 12 h. Finally, the substrates were heated in an oven at 120°C for 2 h before further experiments were undertaken.

Droplet Mobility on Surfaces. The measurements were conducted using a contact angle goniometer (OCA35, Dataphysics). Advancing and receding contact angles were determined by increasing and decreasing the droplet volume between 10 and 20 µL at the rate of 1 $\mu L \cdot s^{-1}$. Sliding angles were determined with a tilt speed of $1° \cdot s^{-1}$. The videos and contact angles were recorded continuously by a commercially available program (SCA). The sliding velocity of liquid droplets on tilted PDMS brushes were determined from the corresponding videos. Each result was repeated more than 3 times.

Condensation. Condensation experiments were conducted in a well-sealed chamber with vapor inlet and outlet (**Figure 5.2a**). The test sample was attached on a cooper plate with thermally conductive paste (OMEGA, OT-201-2). Saturated vapor was controlled by a mass flow controller (OMEGA, FMA-A2208, 0-5 $L \cdot min^{-1}$). The chamber was filled with nitrogen before injecting the

desired vapor. After the chamber was filled with vapor for 10 min, the surface was cooled down by a Peltier element until a specific subcooling was reached (≈10 K). Surface temperature was measured by a thermistor. Videos were recorded using a camera (Ueye, UI-2240SE-C-HQ) attached on a microscope. Droplet characteristics were analyzed from recorded videos with Image J.

For measurements of coalescence time, the chamber was placed vertically. A high-speed camera (Photron, FASTCAM Mini UX100) was used to record the video at 4000 fps for image analysis.

Condensation Heat Transfer Measurement. Condensation heat transfer measurements were conducted in a custom-made setup, which consisted of a vapor generator, a condensation chamber, a chiller for cooling the substrate, a vacuum pump with a cold trap, and a camera. The vapor generator was heated by a heat plate. A magneton in liquids ensured a well-mixed ethanol-water mixture. Temperature (OMEGA, PT100) and pressure (Vacuum Gauges, Pfeiffer, CCR362) inside the condensation chamber were measured in real-time throughout the measurement.

Condensing surfaces were mounted via thermally conductive paste (OMEGA, OT-201-2) on copper plate vertically placed in the condensation chamber. Two thermistors (OMEGA, PT100) attached to the condensing surface were utilized to measure the temperature of the substrate. A chilled water bath (Julabo, F25) was used to dissipate the heat from the condensing surface. A flow meter (MPM, FT-210) was used to measure the speed of the cooling water, and two thermistors (OMEGA, PT100) were used to measure the temperature of the inlet and outlet of the water. All these data were monitored and recorded by a data acquisition system in a LabVIEW program. A vacuum pump (Vacuubrand, RC5 Chemistry Hybrid Vacuum Pump) was integrated to pump down the experimental system to vacuum conditions (P_v < 10 Pa) before the condensation chamber was filled with the desired vapor. Then, the condensation chamber was degassed more than 3 times. The liquids in vapor generator were boiled for more than 30 minutes to remove the non-condensable gas before conducting the experiments. A camera (Sony Alpha

7R III) was used to monitor the characteristics of droplets on surfaces during heat transfer measurements.

5.3 Results and Discussion

When condensing the mixture of water and ethanol on the solid surface (**Figure 5.2a**), the ethanol concentration in the binary liquids determines the thermophysical properties and influences the heat and mass transfer rate during binary condensation. **Figure 5.2b** plots the variation of surface tension, nucleation energy barrier, and latent heat of vaporization for the condensate against the volume fraction of ethanol φ_e in the binary condensate. We measured the surface tension of binary condensate by Dataphysics tensiometer, and estimated the nucleation energy barrier of binary liquids using the classical nucleation theory (see theoretical calculation in **Appendix III**). [111, 291-293] The increased φ_e reduced the liquid surface tension and the nucleation energy barrier, which enhanced the nucleation rate in the condensation process. However, the trade-off for the nucleation enhancement of binary liquids was the reduction in latent heat of vaporization. This conflict implies that the efficient heat transfer of binary condensation necessitates sensitive tuning of the ethanol concentration to achieve the optimal balance between the enhanced nucleation and the high latent heat of vaporization. For convenient description here, BL-70, BL-80, and BL-90 are used to denote the binary liquids with φ_e = 70%, 80%, and 90%, respectively.

To decrease the interfacial thermal resistance of condensate, we used an omniphobic surface coated with polydimethylsiloxane (PDMS) brushes (**Figure 5.2c**) to ensure the dropwise condensation of binary liquids. [188, 193] The PDMS brushes consist of polymer chains of repeating siloxane groups (-O-Si$(CH_3)_2$-O-), which were covalently grafted onto a silicon substrate. To prepare the PDMS brushes, the O_2 plasma-treated silicon substrates were immersed into water-saturated toluene with dichlorodimethylsilane. After 30 minutes, the surface was uniformly coated by PDMS polymer brushes with a thickness of ≈4 nm. The prepared PDMS brushes exhibit great

durability even after ultrasonic washing for 30 minutes (**Figure S5.2**). Because of the high flexibility and low surface roughness of the siloxane chains (see AFM data in **Figure S5.3**), [28, 29] the PDMS coating showed excellent repellency against the binary liquids with extremely low surface tension (see contact angle data in **Table 5.1**). All the binary liquids exhibited a contact angle hysteresis of less than 6° on the PDMS brushes (**Figure S5.4a**). The low contact angle hysteresis results in a low lateral adhesion force F on the surface, which can be calculated by [294-296]

$$F = w\gamma_L k(\cos\theta_r - \cos\theta_a) \quad \text{(Equation 5.1)}$$

where k, w, γ, θ_r, θ_a denote the dimensionless factor, droplet contact width, surface tension of the liquid, receding and advancing contact angle, respectively.

As the surface tension and contact angle hysteresis determine the droplet adhesion force, the mobility of binary liquids on PDMS brushes was enhanced by increasing φ_e (**Figure 5.2d, S5.3b**). Compared with pure water, BL-90 demonstrated ≈25% less of adhesion force, which was only 5.9 μN. Therefore, a 3 μL droplet of BL-90 moved with an average velocity of ≈10.5 mm·s^{-1} on the PDMS brushes with a tilted angle θ_t = 40°, which was ≈5 times faster than that of a 5 μL water droplet (**Appendix III**, **Figure S6**). We also measured the droplet mobility of binary liquids on the hydrophobic surface coated with 1H,1H,2H,2H-perfluorodecyltrichlorosilane (PFDTS). Although the surface energy of PFDTS coating was lower than PDMS brushes, the droplet of binary liquids showed a larger contact angle hysteresis (≈25°) and higher lateral adhesion force (≈30 μN) on the hydrophobic surface (**Figure S5.4b**). These results suggest that the PDMS brushes favor the rapid transport of binary liquid, which can decrease the interfacial thermal resistance during binary condensation.

Table 5.1. Advancing contact angle and receding contact angle of binary liquids on PDMS brushes.

Ethanol in condensate, φ_e (vol%)	0	70	80	90	100
Advancing contact angle (°)	104 ± 1	52 ± 1	48 ± 1	45 ± 1	29 ± 2
Receding contact angle (°)	101 ± 1	46 ± 1	43 ± 1	39 ± 1	25 ± 2

The condensation dynamics of binary liquids on the PDMS brushes were first characterized in a custom-made chamber coupled with optical microscopy (**Figure S5.6**). Nitrogen gas flow carried the saturated binary vapor into the chamber with a stabilized flow rate at ≈1 $L \cdot min^{-1}$. The surface temperature was adjusted using a Peltier element with circulating cooling water, and the subcooling between the saturated vapor and surface was maintained at ≈10 K for the experiments here. The video of condensation was recorded by a camera (Ueye, UI-2240SE-C-HQ) for further analysis.

At the initial stage, the binary liquids condensed with high droplet number density due to the low nucleation energy barrier (**Figure 5.2b,e, S5.6a**). [111, 297, 298] At t = 0 s (**Figure 5.2e**), the droplet density of BL-90 was 1.4 ×109 m^{-2}, which was one order of magnitude higher than that of water. As condensation time increased, the number density of pure water droplets remained stable, whereas the density of the binary condensate decreased continuously (**Figure S5.7a**, e.g., for BL-90, it dropped to 3.6 ×107 m^{-2} at t = 300 s). The considerable variation of droplet number density can be explained by the rapid droplet growth and frequent coalescence during binary condensation, which was also indicated by the time evolution of droplet radius shown in **Figure 5.2f**. The average radius of condensing droplets follows the equation of $r = \rho \cdot t^{\alpha}$, where t is the condensation time, and α is the power law exponent representing the droplet growth mechanism. [211, 299, 300] During the first 300 s, α for the binary liquids was ≈0.7 and for water was ≈0.3. The small α for water condensation suggests that most of the water droplets grow independently without

coalescence in the first 300 s. [301, 302] By contrast, the droplets of binary liquids coalesce much more frequently due to the narrow droplet spacing and small contact angle, thus leading to the rapid growing radius and large α in the droplet growth model.

Figure 5.2g shows the volume of sliding droplets on the condensing surface as a function of ethanol concentration φ_e in the binary liquids. For the omniphobic PDMS surface, the sliding volume of condensing droplets decreased with increasing φ_e, which was consistent with the results of sessile droplet sliding tests (**Figure 5.2d**). The low lateral adhesion force enables BL-90 rapidly slide off the PDMS brushes at a volume of 6×10^{-11} m^3, which was ≈90% less than that of water. As a comparison, the droplet sliding volume on the hydrophobic PFDTS surface was independent to φ_e. Although the sliding volume of pure water droplets was comparable on both hydrophobic and omniphobic surfaces, the low-surface-tension binary liquids slid more efficiently on the PDMS brushes. The rapid liquid transport, therefore, reduces the interfacial thermal resistance associated with condensing droplets on the surface.

The measurements of droplet number density and radius enable us to estimate the condensation rate and heat flux during the first 300 s of the experiment (see details in **Figure S5.7**). The results show that the condensation heat flux of binary liquids did not monotonically rise with the increasing ethanol concentration. Specifically, BL-90, rather than pure ethanol, showed the highest condensation rate. At t = 300 s, the total condensate weight of BL-90 was 6.4×10^{-9} kg, which was 35% higher than that of pure ethanol. Despite the extremely high nucleation density, pure ethanol is not ideal for achieving efficient condensation because the small contact angle limits the volume of individual droplets. This phenomenon indicates that the appropriate mix of water and ethanol is essential to enhance the condensation heat transfer, which should not rely solely on either the high latent heat of vaporization (e.g., water) or the increased nucleation rate (e.g., ethanol).

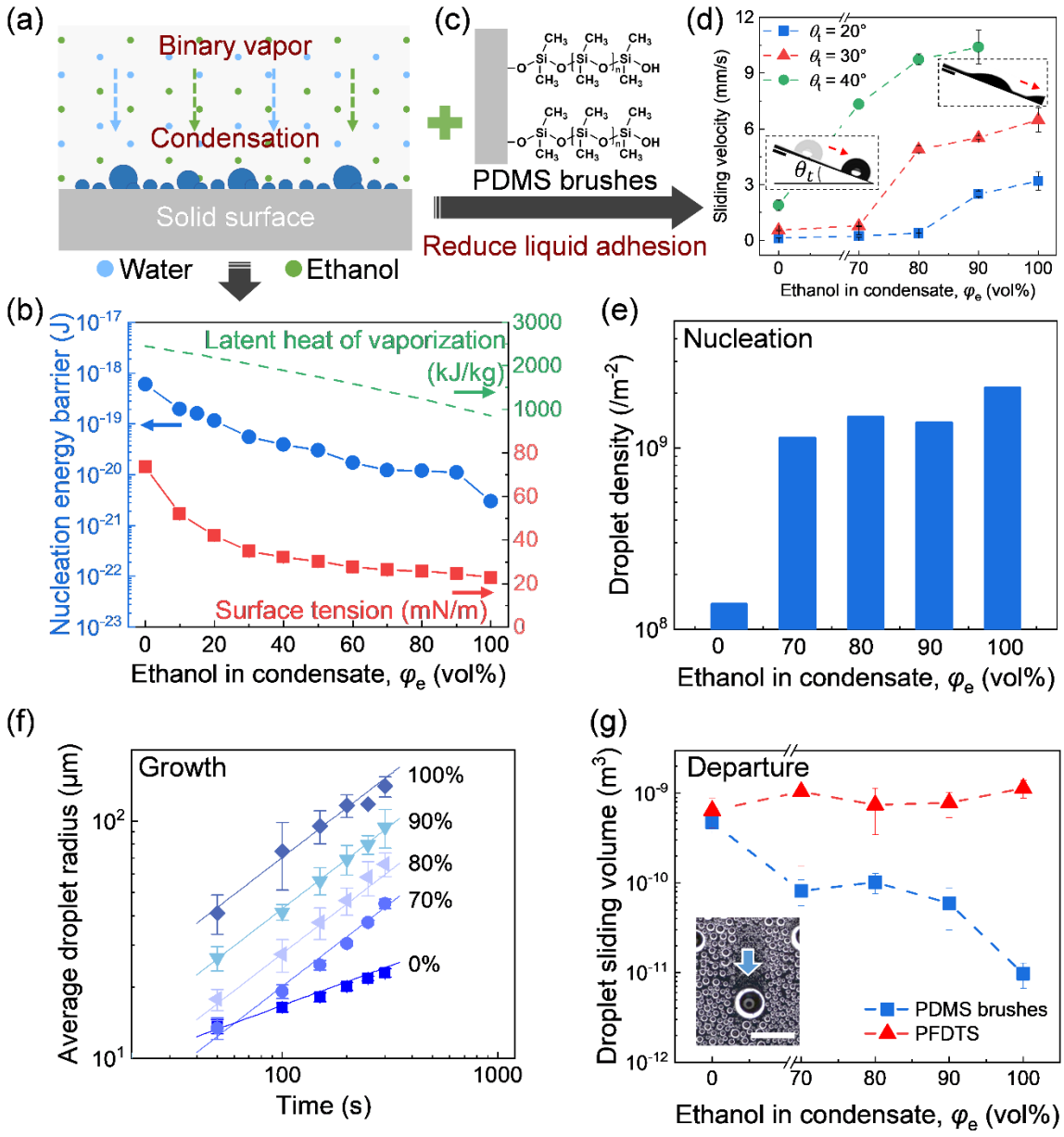

Figure 5.2 Condensation characterization. (a) Schematic of the binary condensation. (b) Nucleation energy barrier, surface tension and latent heat of vaporization of ethanol-water mixtures as a function of ethanol concentration. Nucleation energy barrier was calculated based on the classical nucleation equation. (c) Schematic of the chemical structure of PDMS brushes. (d) Sliding velocity of droplets of ethanol-water mixtures on tilted (θ_t = 20°, 30°, 40°) PDMS brushes. Water: 5 μL, others: 3 μL. Room humidity: 30%. Inset: Sliding photographs of water and

binary liquids (φ_e = 90%) droplets on tilted (θ_t = 40°) PDMS brushes. Scale bar: 2 mm. θt refers to the tilt angle. (e) Initial nucleation site density of liquids on PDMS brushes. (f) Time evolution of the average droplet radius of various condensed liquids on PDMS brushes. The solid lines denote the droplet growth model $r = \beta \cdot t^{\alpha}$, where the slopes are the power law exponent α (0.3 for water and 0.7 for other low-surface-tension liquids). (g) Droplet departure volumes on the vertical PDMS brushes (blue symbols) and hydrophobic PFDTS surface (red symbols) as a function of ethanol concentration. Departure droplet sizes were estimated by comparing sequential images before and after departure during the condensation process. Insert: Image showing the departure of a water droplet on PDMS brushes. (Scale bar: 2 mm)

To accurately determine the heat transfer performance of binary condensation at a steady state, we tested the omniphobic PDMS brushes and the hydrophobic PFDTS surface in a custom-built condensation chamber, as shown in **Figure 5.3a** and **Figure S5.8**. The sample was vertically mounted on a cooling stage to ensure continuous droplet sliding by gravity, and the surface temperature was controlled by circulating cooling water. Before the experiment, the chamber was evacuated to a pressure below 10 Pa to eliminate the influence of non-condensable gases on the condensation heat transfer. [26, 112] The vapor of binary liquids was generated in a boiler and then introduced into the chamber. The vapor and surface temperatures in the chamber were measured with Pt100 RTD sensors to determine the subcooling of the surface. The flow rates and temperatures of cooling water at the inlet and outlet of the cooling stage were measured to calculate the overall heat flux and condensation heat transfer coefficient on the surface. [114, 303, 304] Through the viewport of condensation chamber, the droplet morphology and departure rate were recorded via camera with a macro lens.

The experimentally determined condensation heat transfer coefficient on the PDMS brushes and PFDTS surfaces is plotted as a function of φ_e in **Figure 5.3b**. Compared to pure water and ethanol, the condensation of binary liquids substantially enhances the heat transfer performance. BL-90

demonstrated the highest condensation heat transfer coefficient h ≈ 57 $kW \cdot m^2 \cdot K^{-1}$ on the PDMS brushes. It was more than 1800% higher when compared to the filmwise condensation of ethanol (the green square and dashed line in **Figure 5.3c**, h ≈ 3 $kW \cdot m^2 \cdot K^{-1}$) and 250 % higher than that of water (h ≈ 16 $kW \cdot m^2 \cdot K^{-1}$). For comparison, in a recent study Nenad et al. [202] achieved 200% enhancement in condensation heat transfer coefficient with stable dropwise condensation of ethanol; they used tubes and impregnated their hydrophobic surfaces with Krytox 1525. Due to inefficient droplet shedding, the hydrophobic PFDTS surface showed a ≈35% lower heat transfer coefficient than the omniphobic PDMS brushes in the same condensation environment. Nevertheless, the heat transfer coefficient of binary condensation on the hydrophobic surface was still ≈200% higher than that of ethanol. These results confirmed that the introduction of a small amount of water into ethanol could, in fact, be a general strategy to improve the overall heat transfer performance during the condensation process.

We also investigated the effect of subcooling on condensation morphology to provide further insight into the optimal binary condensation heat transfer performance. **Figure 5.3c** demonstrates the variation of condensation heat flux for BL-90 with the increasing surface subcooling. We observed that dropwise condensation only prevailed when the condensation heat flux was below a critical value (**Figure 5.3d, S5.8-9**). The PDMS brushes sustained the dropwise binary condensation when the heat flux was below ≈130 $kW \cdot m^{-2}$. Once the heat flux exceeded the threshold, the condensate transitioned from the droplet morphology to a liquid film with an irregular shape (**Figure 5.3d**). When the heat flux increased to 150 $kW \cdot m^{-2}$, the liquid film expanded further and eventually merged to cover the whole surface. Accordingly, the condensation heat transfer coefficient decreased with increasing subcooling when filmwise condensation dominated (**Figure 5.3c**). The PDMS brushes demonstrated a significantly higher critical heat flux than the hydrophobic PFDTS surface in the same condensation environment. For BL-90, the critical heat flux on PDMS brushes was 60% higher than that on the PFDTS surface

(≈80 kW·m^{-2}). Such enhanced critical heat flux on the PDMS brushes was also applicable to other binary liquids, e.g., BL-70 and BL-80 (see **Figure S5.11** for more experimental data). These results demonstrate that the dropwise condensation morphology depends not only on the static contact angle of binary liquids but also on the other wetting characteristics and condensation rate on the surface.

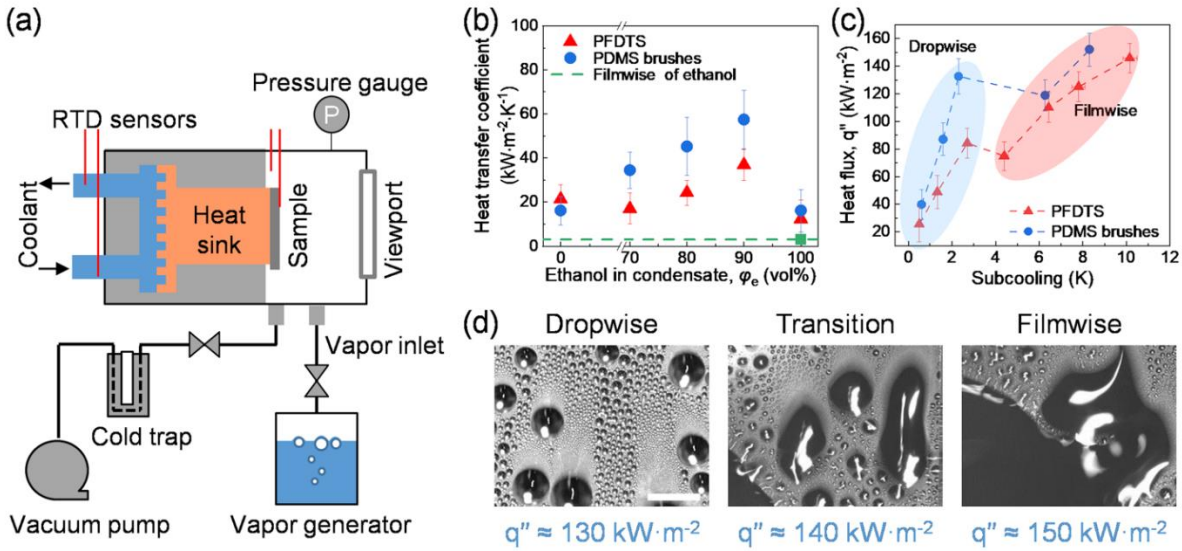

Figure 5.3 Enhanced heat transfer of binary condensation. (a) Schematic of the experimental setup for thermal characterization of binary condensation. (b) Condensation heat transfer coefficient of binary liquids on PDMS brushes and on the hydrophobic PFDTS surface at a subcooling of ≈2K. The green square and the dashed line denote the theoretical value of heat transfer coefficient for filmwise ethanol condensation. (c) Condensation heat flux of binary liquids BL-90 as a function of subcooling on different surfaces. The areas shaded in red and blue denote the dropwise and filmwise condensation regimes. (d) Images showing the dropwise condensation, the transition from dropwise to filmwise condensation, and the filmwise condensation of BL-90 on PDMS brushes under different heat fluxes. Error bars were calculated from the uncertainties of specific heat capacity and density of water, temperature, flow rate, and surface area via error propagation (see **Appendix III** for details).

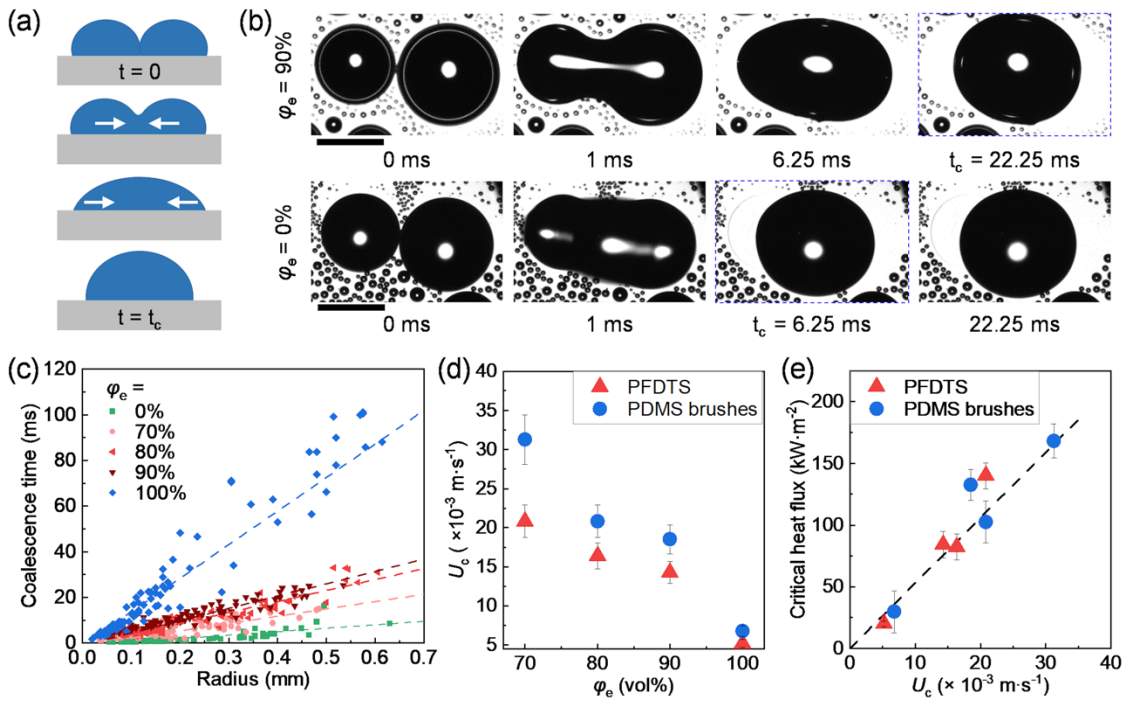

Figure 5.4 Droplet coalescence and critical heat flux during binary condensation. (a) Schematic showing the droplet coalescence process during condensation. t_c refers to the time scale of droplet coalescence, which is defined as the time period from the instant of two droplets getting into contact (t = 0) to the stabilization of coalesced droplet ($t = t_c$). (b) Time-lapsed images showing the droplet coalescence of water and BL-90 (φ_e = 90%) on PDMS brushes. Red rectangles highlight the time ($t = t_c$) when the droplets finish the coalescence processes. (Scale bar: 0.5 mm) (c) Coalescence time t_c as a function of droplet radius for different liquids on PDMS brushes. (d) The values of U_c (coalescence velocity) on PDMS brushes and hydrophobic surface as a function of ethanol concentration. (e) Experimental critical heat flux as a function of U_c on PDMS brushes and on a fluorinated surface.

The transition from dropwise to filmwise condensation for binary liquids can be understood as an incomplete relaxation of a coalesced droplet due to the increased coalescence frequency under high heat flux. [305, 306] As shown in **Figure 5.4a**, when two droplets contact each other by growth, it takes some time for the droplet to revert to a more spherical shape driven by the liquid surface tension. The time required for the coalesced droplet to relax to the equilibrium state was defined as the coalescence time, t_c. [307] If the coalescence frequency becomes so high that droplets do

not have time to revert to their new equilibrium shape, the condensate would appear as a continuous liquid film rather than as discrete droplets on the surface.

To explore the effect of φ_e on the droplet coalescence hydrodynamics, we experimentally measured t_c for different condensing liquids on PDMS brushes by using a high-speed camera. As shown in **Figure 5.4b**, the binary liquids showed slower coalescence when compared to pure water. For the coalescence of two droplets with r = 0.85 mm on the PDMS brushes, the coalescence time t_c was 6 ms for water, and 22 ms for BL-90, respectively. The low surface tension of binary liquids reduces the driving force for coalescence, thus slowing down the relaxation of the coalescing droplet.

When plotting the droplet coalescence time t_c for the binary liquids against the droplet radius r, we obtained a linear relationship between t_c and r for all liquids (**Figure 5.4c**). Based on the experimental results, a characteristic velocity U_c can be defined to characterize the coalescence velocity for different condensing liquids:

$$U_c = r / t_c. \qquad \text{(Equation 5.2)}$$

Figure 5.4d shows the experimentally determined U_c of the condensing droplets with different φ_e on the PDMS brushes and the hydrophobic PFDTS surfaces. Our measurement of characteristic velocity for water droplet coalescence is faster than that reported by Beysens, [307] but agrees well with later observations. [308, 309] The measured U_c of binary liquids decreased with the increasing φ_e, which showed the opposite trend compared to the sliding velocity (**Figure 5.1d**). A substantial increase in droplet coalescence velocity U_c was observed when a small portion of water was added to ethanol. For BL-90, the corresponding $U_c \approx 1.9\times10^{-2}$ m·s^{-1} was ≈170% higher than that of pure ethanol on the PDMS brushes (≈7×10^{-3} m·s^{-1}), therefore resulting in a much more stable dropwise condensation state as demonstrated by the experimental results (**Figure 5.3d**).

Droplet coalescence velocity U_c on the PDMS brushes was consistently higher than that on the hydrophobic PFDTS surface, with the difference up to 50% when φ_e = 70% (**Figure 5.4d**). The rapid droplet coalescence indicated that the liquid contact line moved with less resistance on the PDMS brushes due to the lower droplet lateral adhesion force. Since the rapid droplet coalescence creates more surface area available for nucleation, we obtain a positive correlation between the critical condensation heat flux q_{cr}'' and the coalescence velocity U_c (**Figure 5.4e**). Note that this positive correlation reveals no statistical difference between the PDMS brushes and the PFDTS surface, which underscores that it is the droplet coalescence hydrodynamics on the surface rather than the droplet departure ability that plays a defining role in stabilizing the dropwise condensation under high heat flux.

Our exploration of critical heat flux reveals that efficient binary condensation is due to the synergy of optimized liquid thermophysical properties and liquid/solid interaction. The low contact angle hysteresis on PDMS brushes leads to rapid droplet sliding and high coalescence velocity of binary liquids, thus achieving a high heat transfer coefficient. Note that the enhanced heat transfer by binary condensation is not limited to the ethanol-water mixture. We anticipate that other binary liquids, e.g., water/isopropanol, water/glycol, etc., can also promote heat transfer when the latent heat and liquid surface tension are carefully adjusted. Future development could go a step further by implementing this strategy to the condensing surfaces with textures or gradient wettabilities, [115, 310-313] which may break the limit of heat transfer performance. Meanwhile, although the PDMS brushes shows good durability after ultrasonic washing, the durability for sustaining dropwise condensation in the long-term is still needed to be considered in the future. Additional techniques can be combined, e.g. micro/nano structures or inorganic coatings, in order to advance the approach to real life applications. [314]

5.4 Conclusions

In summary, this study successfully enhanced the condensation heat transfer by adding driblets of water during the phase-change process of ethanol. The condensation of binary liquids exhibited a high nucleation and growth rate, while allowing for the rapid droplet departure. As a result, the binary condensation on the omniphobic PDMS brushes increased the heat transfer coefficient by more than 1800% compared to the filmwise ethanol condensation. Moreover, the binary liquids accelerated the droplet coalescence, thus effectively avoiding the filmwise condensation of low-surface-tension liquids under high heat flux. These results can help to fundamentally improve the phase-change heat transfer of liquids in a wide range of applications such as power generation, thermal management, and waste heat recovery.

5.5 Appendix III

Dropwise condensation heat transfer: The dropwise condensation heat transfer is calculated from individual droplet heat transfer and droplets distribution on surface in equilibrium stage. The heat transfer through an individual droplet was calculated from the numerical solution given by Sadhal and Martin[297, 315] ($\theta_a \leq 90°$) and Nenad Miljkovic[74] ($\theta_a > 90°$). Specifically, the individual droplet heat transfer is characterized by the droplet Nusselt number (*Nu*), where *Nu* is a function of Biot number (*Bi*) and advancing contact angle (θ_a). *Nu* and *Bi* are defined as following:

$$\mathrm{Nu} = \frac{Q}{k_l r_b (T_{sat} - T_s)} \qquad \text{Equation S5.1}$$

$$\mathrm{Bi} = \frac{h_i r_b}{k_l} \qquad \text{Equation S5.2}$$

Where Q is the total heat flux through the single droplet, k_l is the liquid thermal conductivity, r_b is the base radius of droplet, T_{sat} and T_s are the temperature of vapor and surface, respectively, and h_i refers to interfacial liquid-vapor heat transfer coefficient.

Droplets distribution theory is utilized to account for the fraction of droplets in different radius. For small droplets ($r \le r_e$) on hydrophobic ($\theta_a > 90°$) surface, droplets distribution n(r) is determined by

$$n(r) = \frac{1}{3\pi r_e^3 r_{max}} \left(\frac{r_e}{r_{max}}\right)^{-\frac{2}{3}} \frac{r(r_e - r_{min})}{r - r_{min}} \frac{A_2 r + A_3}{A_2 r_e + A_3} e^{B_1 + B_2} \qquad \text{Equation S5.3}$$

Where r_{max} is departure droplet radius, r_e is the radius after which droplets begin to coalesce and growth is then dominated by coalescence (r_e can be obtained from Equation below), r_{min} is the minimum droplet radius (critical nucleation radius).

$$r_e = \frac{1}{\sqrt{4N_s}} \qquad \text{Equation S5.4}$$

Where N_s is initial nucleation density.

The value of A_1, A_2, A_3, B_1, B_2 are presented below:

$$A_1 = \frac{\Delta T}{h_{fg}\rho_l(1-\cos\theta)^2(2+\cos\theta)} \qquad \text{Equation S5.5}$$

Where $\Delta T = (T_{sat} - T_s)$ is subcooling, ρ_l is density of liquid, and θ is contact angle of droplet on surface, usually either static contact angle or advancing contact angle is chosen.

$$A_2 = \frac{\theta}{4k_l \sin\theta} \qquad \text{Equation S5.6}$$

$$A_3 = \frac{1}{2h_i(1-\cos\theta)} + \frac{1}{k_c sin^2\theta}\ \frac{k_p\phi}{\delta_c k_p + hk_c} + \frac{k_p(1-\phi)}{\delta_c k_l + hk_c}\Bigg]^{-1} \qquad \text{Equation S5.7}$$

If on surfaces with structures;

$$A_3 = \frac{1}{2h_i(1-\cos\theta)} \qquad \text{Equation S5.8}$$

If on smooth surfaces.

$$B_1 = \frac{A_3}{\tau A_1}\ \frac{r_e^2 - r^2}{2} + r_{min}(r_e - r) - r_{min}^2 \ln\left(\frac{r - r_{min}}{r_e - r_{min}}\right)\Bigg] \qquad \text{Equation S5.9}$$

$$B_2 = \frac{A_3}{\tau A_1}\ r_e - r - r_{min} \ln\left(\frac{r - r_{min}}{r_e - r_{min}}\right)\Bigg] \qquad \text{Equation S5.10}$$

$$\tau = \frac{3r_e^2(A_2R_e + A_3)^2}{A_1\left(11A_2R_e^2 - 14R_eR_{min} + 8A_3R_e - 11A_3R_{min}\right)} \qquad \text{Equation S5.11}$$

For large droplets ($r > r_e$) on hydrophobic surfaces, droplets distribution ($N(r)$) is determined from

$$N(r) = \frac{1}{3\pi r_e^2 r_{max}}\left(\frac{r_e}{r_d}\right)^{-\frac{2}{3}} \qquad \text{Equation S5.12}$$

For droplets on hydrophilic ($\theta_a \leq 90^\circ$) surface, droplets distribution $n(r)$ and $N(r)$ are determined by

$$\mathrm{n(r)} = \frac{1}{3\pi r_e^3 r_{max}(\sin\theta_e)^3}\left(\frac{r_e}{r_d}\right)^{-\frac{2}{3}}\frac{r(r_e - r_{min})}{r - r_{min}}\frac{A_2 r + A_3}{A_2 r_e + A_3}e^{B_1+B_2} \qquad \text{Equation S5.13}$$

$$\mathrm{N(r)} = \frac{1}{3\pi r_e^2 r_{max}(\sin\theta_e)^3}\left(\frac{r_e}{r_d}\right)^{-\frac{2}{3}} \qquad \text{Equation S5.14}$$

Finally, the condensation heat flux is obtained from Equation below:

$$q'' = \int_{r_{min}}^{r_e} Qn(r)dr + \int_{r_e}^{r_{max}} QN(r)dr \qquad \text{Equation S5.15}$$

Then the condensation heat transfer coefficient h is obtained from

$$h = \frac{q''}{\Delta T} \qquad \text{Equation S5.16}$$

Surface tension of binary fluids: The surface tension of binary fluids were measured by using a Dataphysics Tensiometer (DCAT 11EC). The fluids were collected from condensation of vapor mixtures in a custom made device and then put in the glass beaker inside the chamber. After cleaned with a fire, a plate was placed inside the chamber on top of binary fluids. The surface tension was then measured by the Wilhelmy plate method. Each measurements was repeated for more than 5 times.

Nucleation energy barrier of ethanol-water binary liquids: The nucleation energy barrier is estimated based on the classical nucleation theory, [111, 293]

$$\Delta G = \frac{\pi \sigma_{lv} r_{min}^2 (2 - 3\cos\theta + cos^3\,\theta)}{3}, \qquad \text{Equation S5.17}$$

where σ_{lv} is the liquid surface tension, θ is the contact angle, r_{min} is the droplet nucleation radius.

$$r_{min} = \frac{2\sigma_{lv} T}{\rho h_{fg} \Delta T}, \qquad \text{Equation S5.18}$$

where T is the temperature. The relationship between nucleation rate (J) and nucleation energy barrier is expressed as

$$J = Kexp(-\frac{\Delta G}{kT}), \qquad \text{Equation S5.19}$$

where K is a kinetic prefactor (*18*), k is the Boltzmann constant.

Uncertainty Analysis: The error propagation theory is used to analyze the experimental errors. The experimental results heat flux (q, W·m^{-2}), heat transfer coefficient (h, kW·m^{-2}·K^{-1}) and subcooling (ΔT, K) can be expressed as follows:

$$q = \frac{c_p (T_{out} - T_{in}) \rho U_{water}}{A} \qquad \text{Equation S5.20}$$

$$h = \frac{q}{\Delta_{sub}} \qquad \text{Equation S5.21}$$

$$\Delta T = T_v - T_s \qquad \text{Equation S5.22}$$

where c_p is specific heat capacity of water (J·kg^{-1}·K^{-1}), T_{out} and T_{in} are temperature of the inlet and outlet of cooling water near the condensation chamber (K), ρ is density of water (kg·m^{-3}), U_{water} is the flow rate through the tube (m^3·s^{-1}), A is surface area of the sample (m^2), T_v and T_s are temperature of vapor and surface, respectively.

Based on error propagation theory, the uncertainty (σ) of q, Δ_{sub}, and h can be expressed as follows:

$$\sigma(q) = \sqrt{\left[\frac{\partial q}{\partial c_p}\sigma(c_p)\right]^2 + \left[\frac{\partial q}{\partial T_{in}}\sigma(T_{in})\right]^2 + \left[\frac{\partial q}{\partial T_{out}}\sigma(T_{out})\right]^2 + \left[\frac{\partial q}{\partial \rho}\sigma(\rho)\right]^2 + \left[\frac{\partial q}{\partial U_{water}}\sigma(U_{water})\right]^2 + \left[\frac{\partial q}{\partial A}\sigma(A)\right]^2}$$

Equation S5.23

$$\sigma(\Delta_{sub}) = \sqrt{\left[\frac{\partial \Delta_{sub}}{\partial T_v}\sigma(T_v)\right]^2 + \left[\frac{\partial \Delta_{sub}}{\partial T_s}\sigma(T_s)\right]^2}$$

Equation S5.24

$$\sigma(h) = \sqrt{\left[\frac{\partial \sigma(h)}{\partial q}\sigma(q)\right]^2 + \left[\frac{\partial \sigma(h)}{\partial \Delta_{sub}}\sigma(\Delta_{sub})\right]^2}$$

Equation S5.25

Filmwise condensation heat transfer: The classical Nusselt model[112, 115, 316] was employed to estimate the filmwise condensation heat transfer.

$$h = 0.943\left[\frac{k_l^3 \rho_l(\rho_l - \rho_v) g h_{fg}}{\mu_l L \Delta T}\right]^{0.25}$$

Equation S5.26

Where g is the gravitational acceleration ($g = 9.81\ m \bullet s^{-2}$), μ_l is dynamics viscosity of liquid ($\mu_l = 7 \times 10^{-3}\ N \bullet S \bullet m^{-2}$), L is characteristic condensation length ($L = 0.04\ m$), $h_{fg}$is latent heat of vaporization of the condensate.

Filmwise condensation heat flux can be calculated from

$$q'' = h \bullet \Delta T$$

Equation S5.27

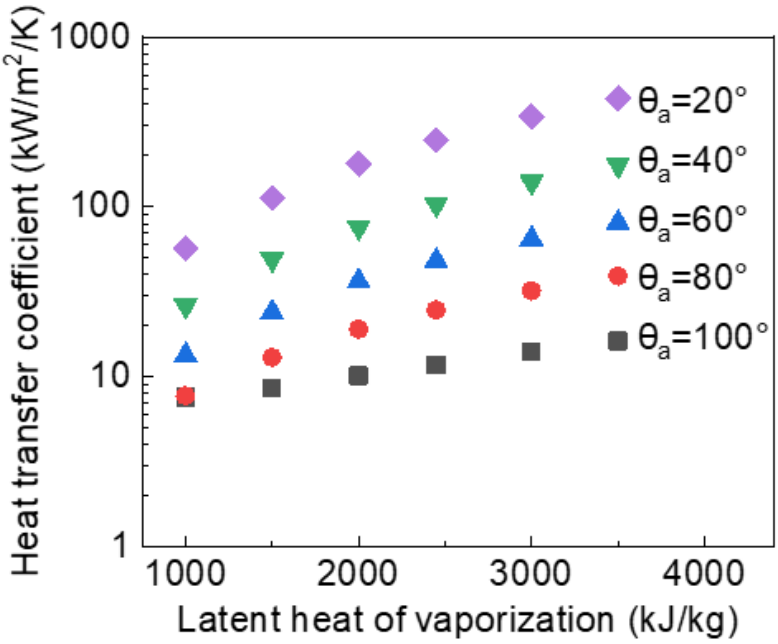

Figure S5.1 Model results. Model results of heat transfer coefficient as a function of latent heat of vaporization of liquids for varying advancing contact angle. Contact angle hysteresis = 10°, departure droplets radius r_{max} = 0.5 mm.

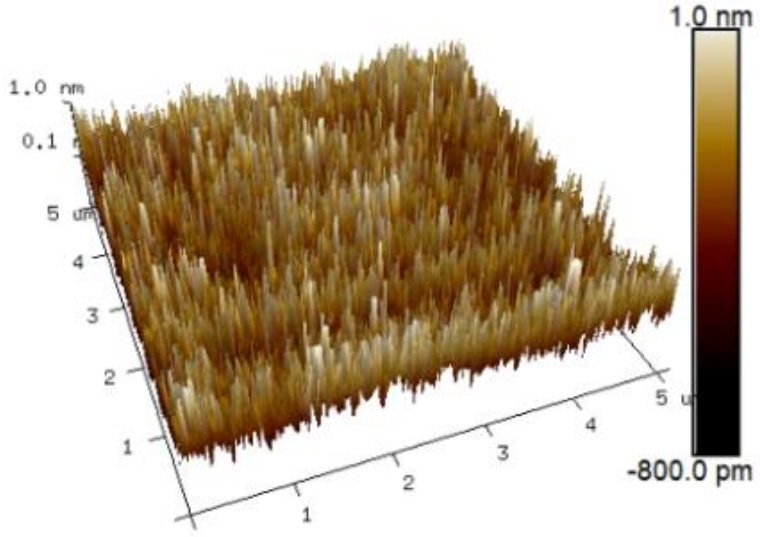

Figure S5.2 AFM image depicting the topography of PDMS brush surface with root mean square roughness, $R_a \approx 1$ nm.

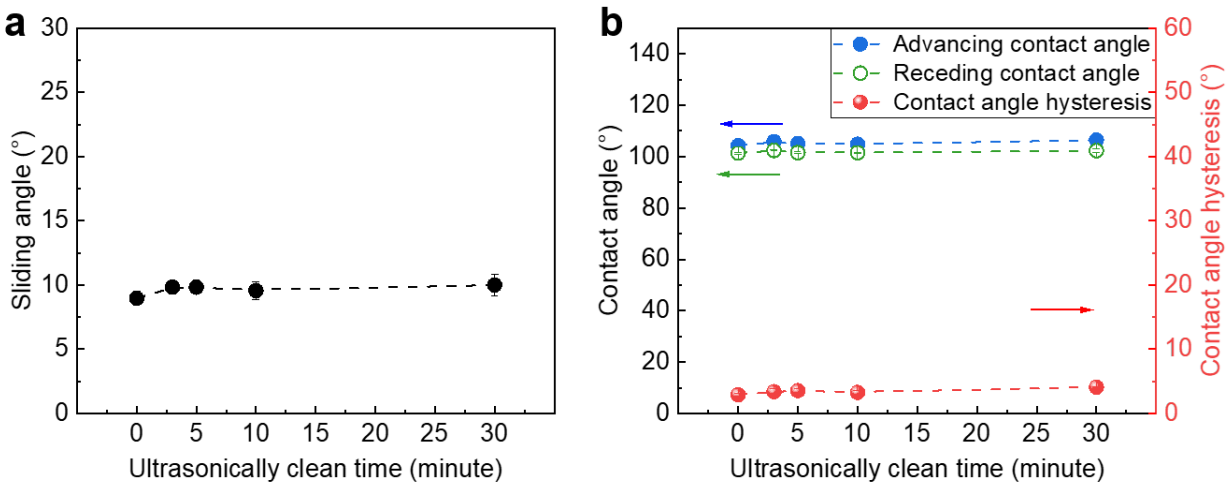

Figure S5.3 Sliding angle (a) and contact angles (b) of water on PDMS brushes after ultrasonically clean in toluene for different times: 3, 5, 10, 30 minutes.

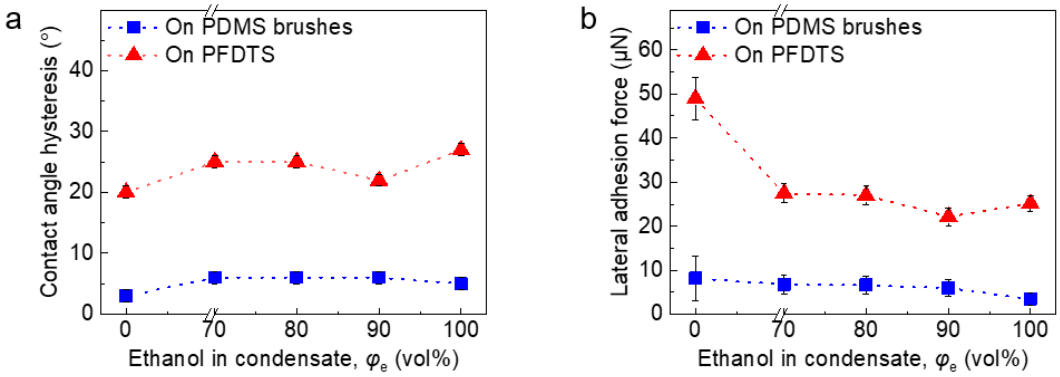

Figure S5.4 Contact angle hysteresis (a) and calculated lateral adhesion force (b) of binary liquids (φ_e = 0%, 70%, 80%, 90% and 100%) on the PDMS brushes and on PFDTS surface. All experiments were carried out at ≈22°C.

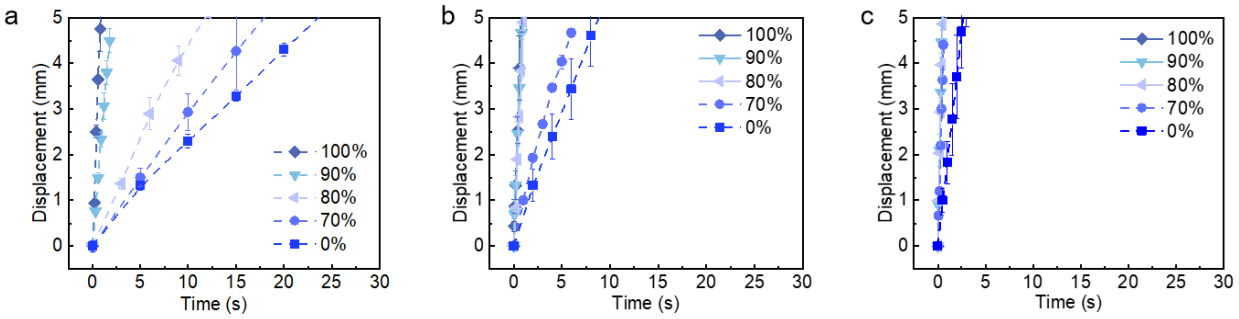

Figure S5.5 Ethanol-water mixtures droplets motion on tilted PDMS brushes. Sliding angle: 20°(left), 30°(mid), 40°(right). (Water: 5 μL, others: 3 μL)

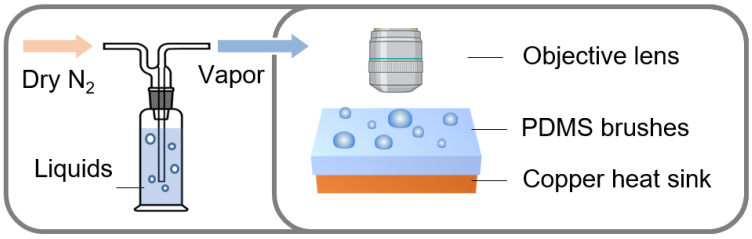

Figure S5.6 Schematic of the condensation setup.

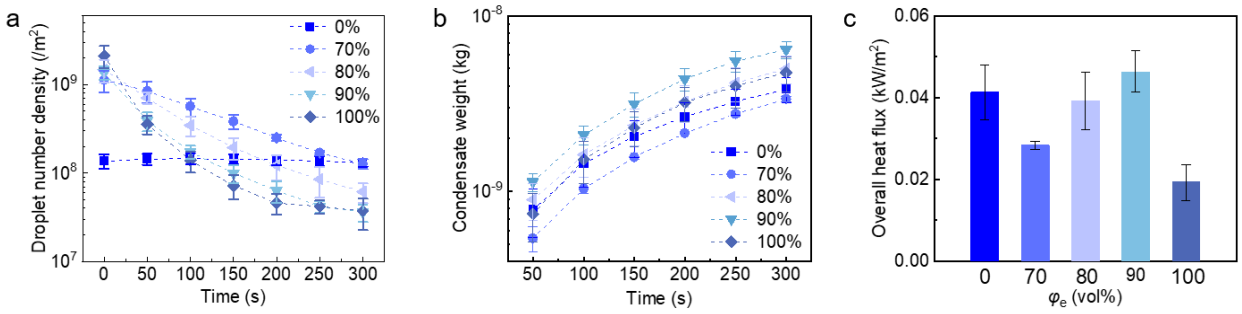

Figure S5.7 (a) Condensed droplet site density of various liquids on PDMS brushes as a function of condensing time. (b) Weight of condensed droplets on PDMS brushes as a function of condensation time for liquids with different φ_e. (c) Overall condensation heat flux of water, binary liquids, and ethanol on PDMS brushes in the 300 s experiment. The results were obtained from condensation transfer rate, latent heat of vaporization, and condensing surface area.

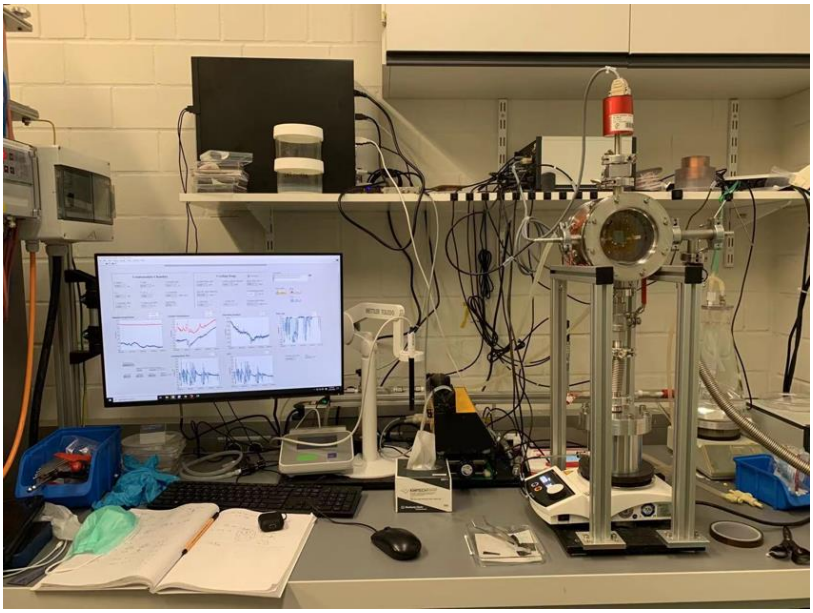

Figure S5.8 Photograph of the experimental setup for heat transfer performance.

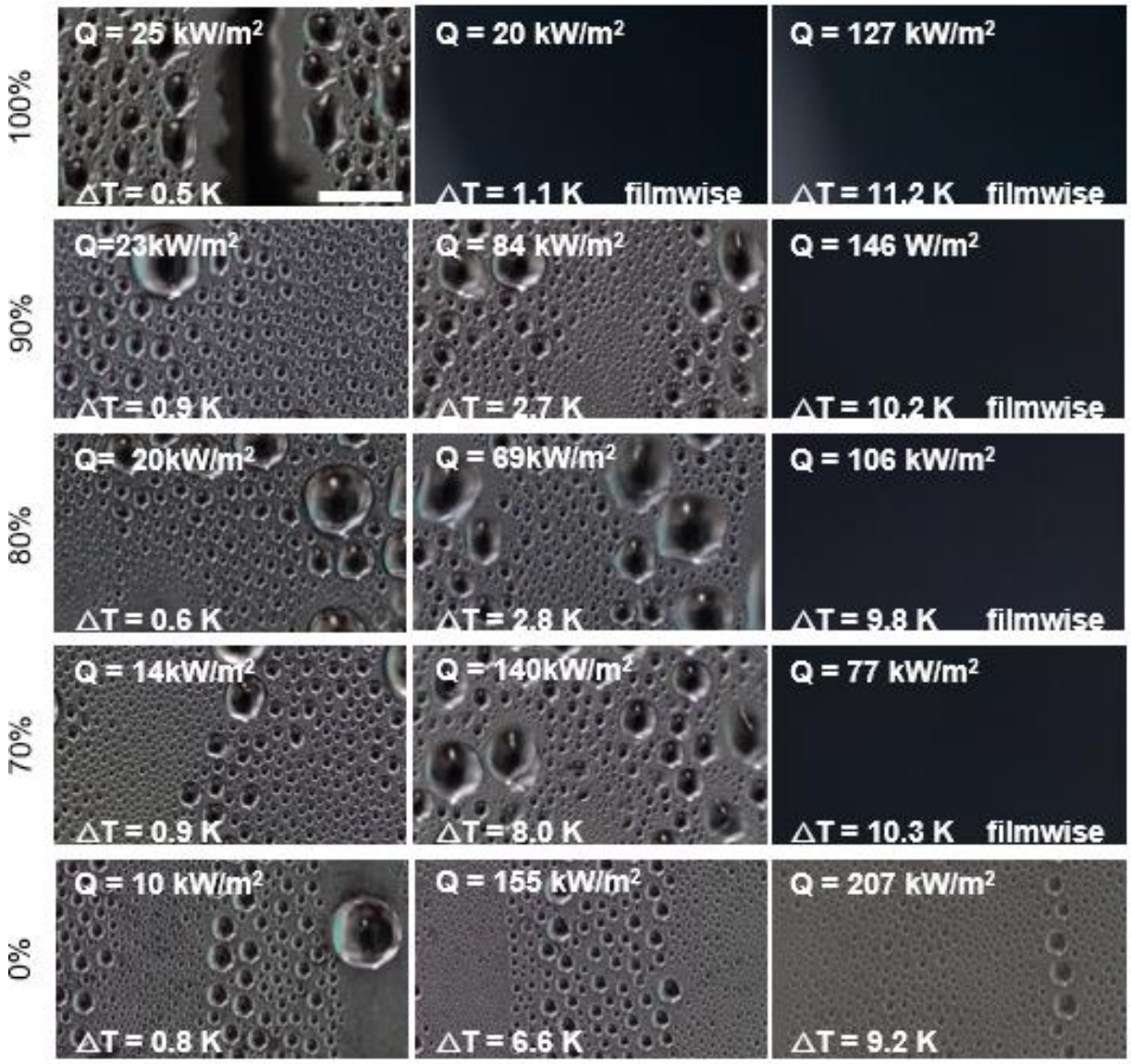

Figure S5.9 Condensation on fluorinated surface. (Scale bar: 2 mm)

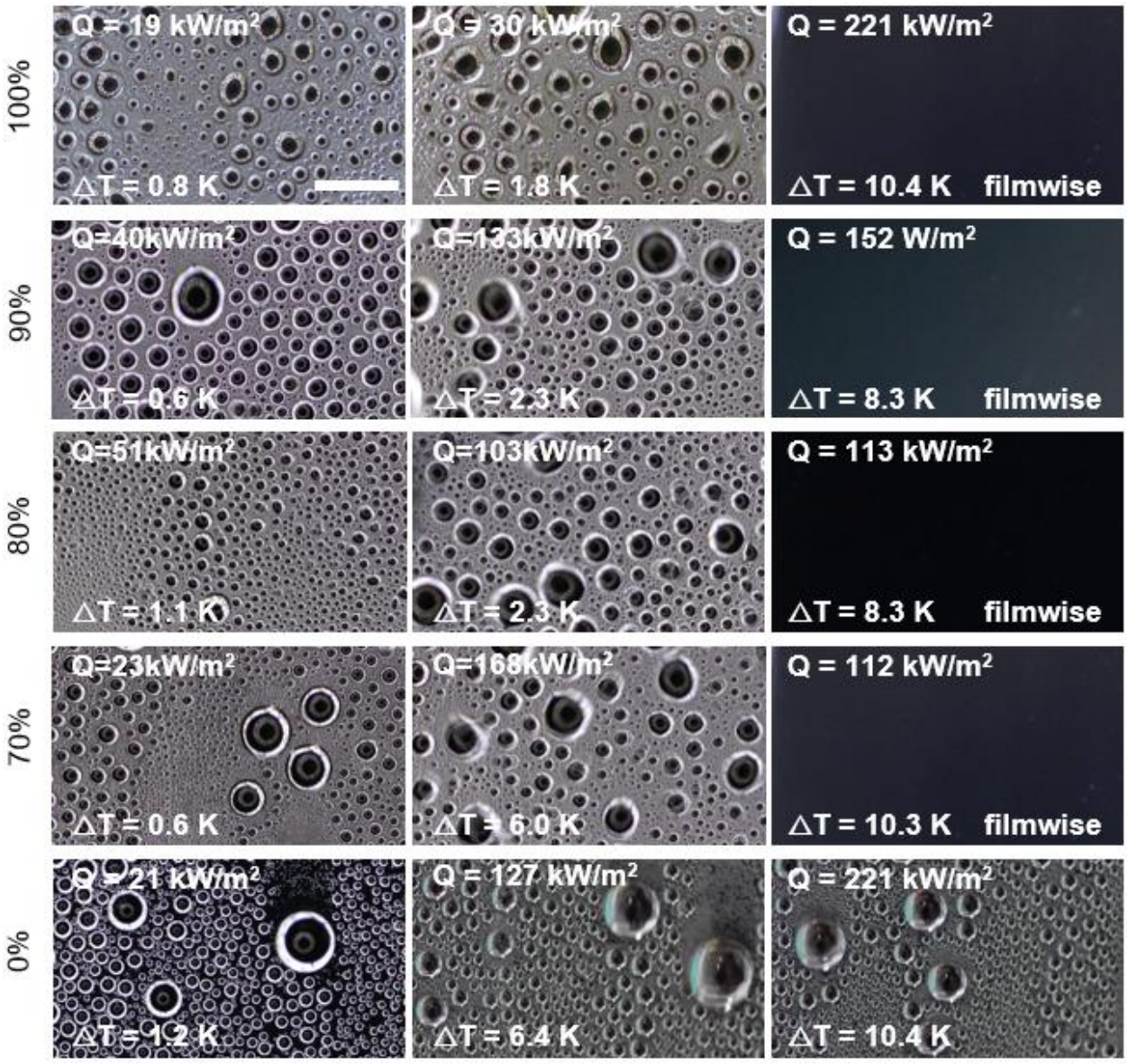

Figure S5.10 Condensation on PDMS brushes. (Scale bar: 2 mm)

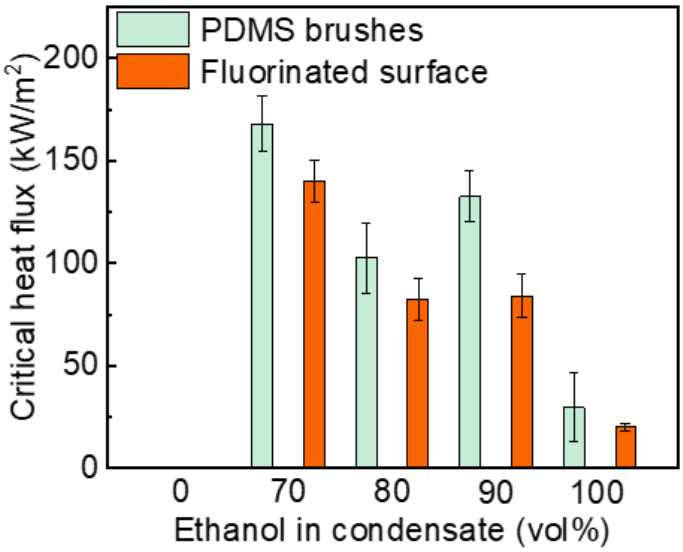

Figure S5.11 Critical heat flux of ethanol-water mixtures on the fluorinated surface and PDMS brushes.

Table S5.1 Advancing contact angle and receding contact angle of binary liquids on fluorinated surface.

Ethanol in condensate, φ_e (vol%)	0	70	80	90	100
Advancing Contact angle (°)	116±1	71±1	68±1	64±1	62±2
Receding Contact angle (°)	95±1	46±1	44±1	42±1	35±2

Table S5.2 Summarizes uncertainties of measured parameters.

Parameters	c_p	T	ρ	U_{water}	A
Uncertainty	± 1 %	± 0.03 K	±1 %	± 5*10^{-7} %	±10^{-6}

6. Spontaneous Charging of Drops on Lubricant-Infused PDMS Brushes§

When a drop of a polar liquid slides over a hydrophobic surface, it acquires a charge. As a result, the surface charges oppositely. For applications such as the generation of electric energy, lubricant-infused surfaces may be important because they show a low friction for drops. However, slide electrification on lubricant-infused surfaces has not been studied yet. Here, slide electrification on lubricant-infused surfaces was studied by measuring the charge generated by series of water drops sliding down inclined surfaces. As lubricant-infused surfaces we used PDMS-coated glass with micrometer thick silicone oil films on top. For PDMS-coated glass without lubricant, the charge for the first drop is highest. Then it decreases and saturates at a steady state. With lubricant, the drop charge starts from 0, then it increases and reaches a maximum charge per drop. Afterwards, it decreases again before reaching its steady state value. This dependency is not a unique phenomenon for lubricant-infused PDMS, it also occurs on lubricant-infused micropillar surfaces. We attribute this dependency of charge on drop numbers to a change in surface conductivity and depletion of lubricant. These findings are helpful for understanding the charge process and optimizing solid-liquid nanogenerator devices in applications.

---

§ This chapter is a slightly modified version of the following article: [317]

Li, S., Bista, P., Weber, S., Kappl, M., and Butt, H.-J., Spontaneous Charging of Drops on Lubricant-Infused Surfaces. Langmuir. **2022**, 38(41): 12610-12616. Copyright © 2022 The Authors. Published by American Chemical Society.

Author Contributions: Li, S., and Butt, H.-J. designed the experiments, analyzed the data, and prepared the manuscript. Li, S. fabricated the surfaces and carried out the experiments. Bista, P. assisted with the charge experiments. Kappl, M. assisted with the confocal microscope measurements. Li, S. and Butt, H.-J. planned and wrote the manuscript. All authors reviewed and approved the manuscript.

6.1 Introduction

Slide electrification[261, 318-322] is the spontaneous charging of hydrophobic, insulating surface by sliding liquid drops. It is generally accepted that drops of polar liquids, such as water, moving down inclined, low-energy and low-conductivity surfaces acquire a charge. Usually they charge up positively, while the negative countercharge is deposited on the free solid surface. This may be attributed to ion transfer to the solid surface, e.g. OH^-.[323-325] Despite being ubiquitous and despite potential applications in generation of electric energy or manipulating drop movement, [253, 326-328] we have little fundamental understanding of slide electrification. There is no clear picture of the underlying microscopic processes nor a first principles predictive model. With respect to solid tribocharging, [329-331] one fundamental difference is that in slide electrification no huge shear stresses can occur, not even locally. In solid tribocharging, protrusions on the microscale typically experience huge shear stresses. They can break covalent bonds and generate locally enough energy to bring electric charges to the free solid surface. Such a high shear stress cannot be generated by liquid drops.

To better understand the underlying principles of slide electrification, we study charge separation on lubricant-infused surfaces. In that case, the wetted surface is liquid rather than solid. Usually, lubricant-infused surfaces consist of a structured surface that is impregnated with a lubricant. [22, 41, 42, 125, 332, 333] These surfaces have attracted lots of attention because they provide low siding angles. Water drops start sliding down inclined lubricant-infused surfaces even at low tilt angle. However, these surfaces usually suffer from depletion problem, which may affect the electrification efficiency. [334] To better understand the slide electrification on lubricant-infused surfaces, we measured the drop charge of the sliding deionized water drops on lubricant-infused PDMS with different oil content, as well as those conventional ones that using a structured surface.

With respect to slide electrification lubricant-infused surfaces are interesting for three reasons. From the fundamental point of view, they reduce shear at the substrate-liquid interfaces. Second,

they allow drops to slide at low tilt angle which for electric energy generation may be important. Third, as it will turn out, charge measurements provide an easy method to detect depletion of lubricant-infused surfaces.

6.2 Experimental

Preparation of Lubricant-infused Surfaces.

Cleaning and Activation of Glass Substrates. Glass substrates (2 mm thick) were washed ultrasonically for 15 minutes in toluene, ethanol, water, respectively before blow-drying by nitrogen. Then the substrates were treated with an oxygen-plasma (Diener Electronic Femto, 120W, 6 cm^3 min^{-1} oxygen flow rate) for 5 min.

Preparation of PDMS surfaces. To prepare polydimethylsiloxane (PDMS) surfaces, [188] the substrates were immersed in 40 mL toluene (with saturated water) mixed with 1.4 mL dimethyldichlorosilane. After reacting for 0.5 h, the substrates were rinsed with toluene to remove the residues and dried with nitrogen. The PDMS coating was ca. 4 nm with a surface roughness of ca. 1 nm, which were measured using Atomic Force Microscopes.

Preparation of SU8 Surfaces. To prepare SU8 pillars, [43, 335] SU8 photoresist was spin-coated on the substrates first. Then the SU8 film was cured into a structured array pattern of micropillars (pillar diameter: 5 µm; center to center distance: 10 µm; height: 10 µm), utilizing photolithography. After UV-exposure (8 s) using a photomask and baking cycles at 65 °C (30 min), 95 °C (3 min) and 65 °C (30 min), the uncured SU-8 was dissolved in a developer solution and washed in propanol. The SU8 was then coated with silica by treatment with an O_2 plasma for 30 s, followed by immersion in a solution of tetraethoxysilane (1.82 mL) and ammonium hydroxide (28% in water, 4.2 mL) in ethanol (50 mL) for 2–3 h. After 1 h of oxygen plasma, the filament was coated on the SU8 pillar by immersing the substrate to a solution which contains 0.4 mL trichloromethylsilane and 100 mL toluene (with 150 ppm water). Finally, PFOTS was coated on the SU8 surfaces by

placing the glass substrates into a desiccator, where 20 µL trichloro(1H,1H,2H,2H-perfluoro-octyl)silane (PFOTS) was deposited inside. The chamber was then evacuated to 50 mbar and the reaction was allowed to proceed for 3 hours.

Preparation of Lubricant-infused Surfaces. To prepare lubricant-infused surfaces, [168, 174] 200 µL drop of silicone oil (Fisher Scientific UK, 100 cSt) were deposited on the substrate. Then the substrates were put vertically in a glass staining tank with a naturally tilted angle of 90° ± 2°. The lubricant content/thickness was controlled by the tilt time. Afterwards, the substrates were put horizontally in the sample box before further measurements.

Surface characterization

Thickness Measurement. The thickness of the lubricant on the PDMS was measured by confocal laser scanning microscopy (Leica SP8). Lumogen red (F300 BASF) was used to dye the lubricant (concentration: 0.1 mg/mL). [336] The microscope was equipped with a C-Apochromat 40/1.2 W water-immersion objective to visualize the thickness of the lubricant. For excitation, an argon laser fiber-coupled to the microscope were used (633 nm). Each measurement was conducted on more than 10 positions.

Contact angles. Advancing and receding contact angles were measured using an OCA 35 contact angle goniometer (Dataphysics, Germany) in the sessile drop configuration. The water volume was gradually (1 $\mu L \cdot s^{-1}$) increased from 10 µL to 20 µL and then decreased from 10 µL to 20 µL, respectively. On surfaces without lubricant, the contour of the drop was easily detected by the software. On lubricant-infused surfaces, wetting ridge formed immediately after the water drop was deposited on the surface. To extract the apparent contact angles, the interface between water drop and the surface was defined to be the position which is a bit above the meniscus, to ignore the distortion effect of wetting ridge. [337]

Charge Measurement. Slide electrification experiments were conducted in a custom build device (**Figure 6.2a**) using deionized water. The system mainly consists of a Faraday cage, a water

pump, a current amplifier, and a LabVIEW program. [320] The Faraday cage was electrically grounded, and inside there are a tilted stage, a flat-tipped syringe needle, a laser and its detector, and an ionizing air blower. The surfaces were mounted on the tilted stage at 50°, and the needle (drop volume: 45 µL) was mounted 5 mm above the surface. The deionized water drops (Sartorius Arium Pro VF, 18.2 MΩcm resistivity, Germany) were generated regularly at a rate of 30 drops/minutes by the water pump (Gilson Minipuls 3, Wisconson, USA). The drops were deposited on the top area of the tilted surfaces. As drops slid down the surface, they contacted two electrodes and a laser beam. The first electrode grounded the drop to make sure it starts electrically neutral. The second electrode measured the drop current by a low noise current amplifier (response time: 5 µs, FEMTO DLPCA-200, Berlin, Germany). By integrating the current signal over the peak (**Figure S6.1**, 0-2ms), drop charge was obtained. The laser beam was used to trigger the data collection and a National Instruments data acquisition card (NI USB-6366 X-Series) was used to record of the discharge current by the LabVIEW program. Before every new experiment, an ionizing air stream (Simco-Ion, Pennsylvania, USA) was blown over the surface for 5 minutes in order to neutralize the surface. Drops then run over the surfaces, and for every drop, a current spike was recorded when it touched the second electrode. Current signals were integrated for every drop to quantify the drop charge.

Velocity Measurement. To measure the drop velocity on the surfaces another custom built setup was used. A high speed camera (FASTCAM MINI UX100, Photron with a Titan TL telecentric lens, 0.268×, 1'' C-Mount, Edmund Optics) with a frame rate of 500 FPS was used to record the sliding drops on the tilted surfaces. A MATLAB program (DSAfM) was adopted to analyze the video. To obtain the drop velocity images were further analyzing, first, they were corrected by subtracting the background from the original images. Afterwards, the edge position of the drops were identified and finally the velocities were calculated from the edge positions in each frame (for details see[261]).

6.3 Results and Discussion

Surface Characterization

To control the thickness of the lubricant layer, the glass plates were placed vertically (**Figure 6.1a** and **S5.2**) for 15, 30, 60 or 600 minutes, resulting in a lubricant thickness of ca. D = 20, 15, 10, 5 µm, respectively (**Figure 6.1b,c**). The lubricant thickness was obtained by plotting the intensity curve of the lubricant (**Figure S6.3**). The results in **Figure 6.1c** show that the lubricant thickness was relatively homogeneous all over the surface within a small error. For convenient description here, PDMS-x are used to denote the PDMS surface with the lubricant of x µm. For example, PDMS-20 represents the PDMS surface with lubricant thickness of 20 µm.

Because of the flexible polymer chains, PDMS-0 showed a contact angle hysteresis with water of 15° ± 2° (**Table 6.1**) and a sliding angle of 15° ± 1° (**Figure 6.1d**). When adding lubricant, the contact angle hysteresis further decreased and water drops started to move at even lower tilt angles. For PDMS-20, the contact angle hysteresis and sliding angle for water was 2° ± 1° and 1° ± 1°, respectively. The low contact angle hysteresis on PDMS surfaces also lead to a low adhesion force for water drops. The lateral adhesion force can be calculated by[295, 296, 338]

$$F = w\gamma_L k(\cos\theta_r - \cos\theta_a) \qquad \text{(Equation 6.1)}$$

where, $k \approx 1$, w, γ , θ_r, θ_a are the dimensionless factor, droplet contact width, surface tension of the liquid, receding and advancing contact angle, respectively. As shown in **Figure 6.1d**, without lubricant, a 45 µL water drop showed a lateral adhesion force of 97 µN ± 12 µN. When adding lubricant, the lateral adhesion force decreased to below 40 µN. All the results above illustrate the high mobility of water drops on lubricant-infused PDMS surfaces.

For comparison, we also studied a model lubricant-infused array of micropillars (**Figure S6.4** for schematic and SEM images of the SU8 pillars). The contact angle hysteresis for water on SU8 with and without lubricant were 8° ± 1° and 3° ± 1°, respectively (**Table 6.1**).

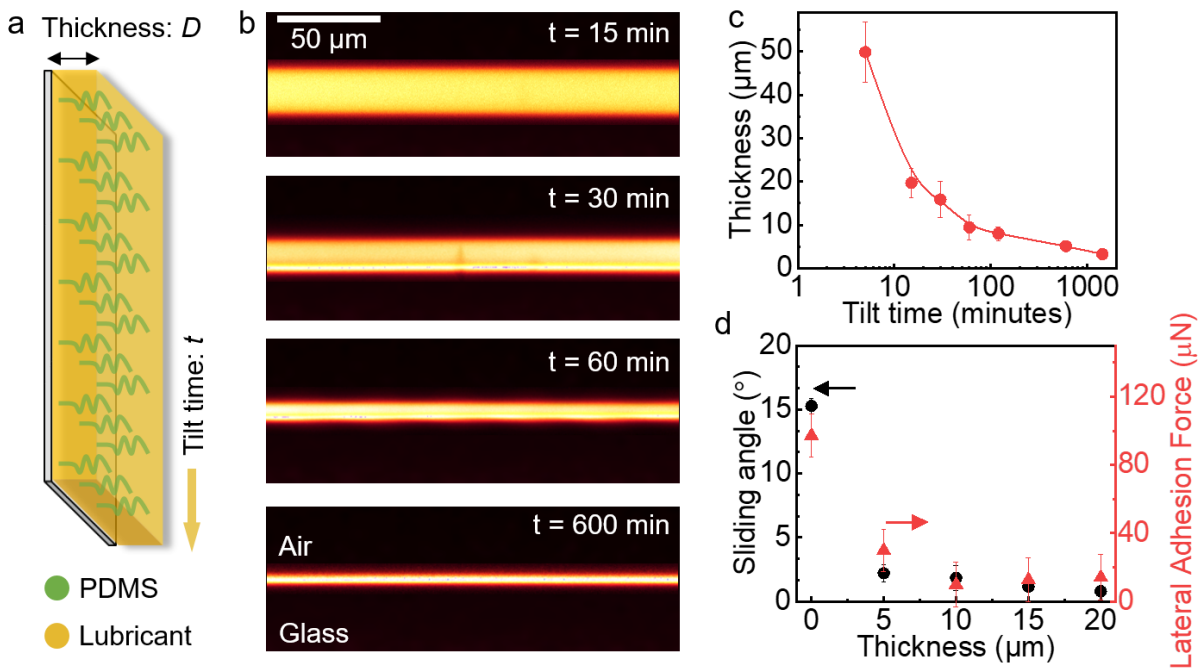

Figure 6.1 Surface characterization. (a) Schematic of lubricant-infused PDMS surfaces. After depositing a dyed lubricant on the PDMS surfaces, the samples were tilted vertically for different time t to remove the residual lubricant. After that, the samples were stored carefully before further measurements. (b) Confocal microscope images (vertical cross-sections) of PDMS surfaces with lubricant after different tilt times t. The images represent vertical cuts and are used to measure the lubricant film thickness. (c) Lubricant thickness as a function of tilt time. (d) Sliding angle and calculated lateral adhesion force of a 45 µL water drop on PDMS surfaces with different lubricant thickness.

Table 6.1 Contact angle of water on lubricant-infused surfaces.

Surface	Advancing contact angle θ_a (°)	Receding contact angle θ_r (°)	Contact angle hysteresis $\Delta\theta$ (°)
PDMS-0	108 ± 1	92 ± 1	15 ± 2
PDMS-5	103 ± 1	98 ± 2	5 ± 2
PDMS-10	98 ± 2	96 ± 2	2 ± 1
PDMS-15	98 ± 1	96 ± 1	2 ± 1
PDMS-20	96 ± 1	94 ± 2	2 ± 1
SU8	144 ± 2	136 ± 3	8 ± 1
Lubricant-infused SU8	97 ± 1	95 ± 1	3 ± 1

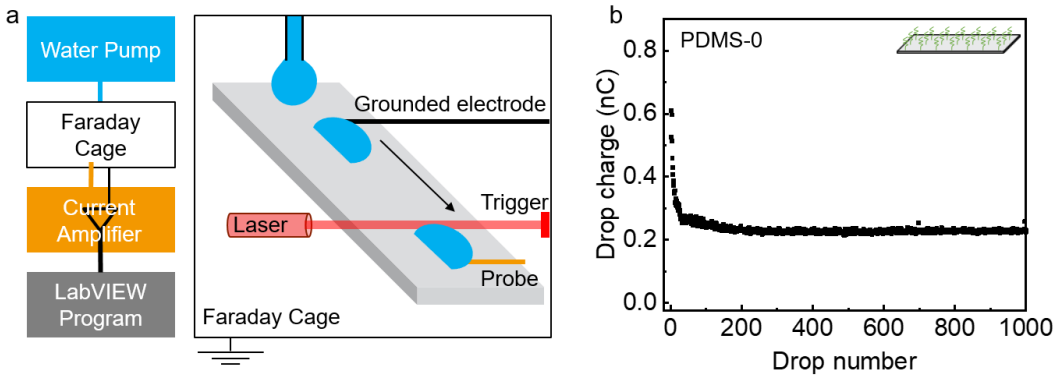

Figure 6.2 Slide electrification. (a) Schematic of the device for charge measurement. Its main components are a water pump, a Faraday cage, a current amplifier, and a LabVIEW program for analysis. The drop current is measured by an electrode, which is then amplified for analysis. (b) Drop charge versus drop number on PDMS-0. The drop charge is obtained by integrating the current over the first 2 ms.

Slide Electrification

Slide electrification experiments were conducted in a custom build device (**Figure 6.2a**) using deionized water. **Figure 6.2b** shows one representative charge curve on a PDMS surface (charge per drop versus drop number, *Q*-vs-*n*). The first drop carried the highest charge of ca. 0.61 nC. After the first drop, the charge of successive drops decreased. After ca. 40 drops, it reached a steady-state value of 0.23 nC ± 0.01 nC. This is consistent with previous study on hydrophobic surface. [320, 339] Because surface is neutral in the beginning, the first drop slides over the surface and has the highest charge value. After the first drop leave, the surface discharges within a characteristic time τ. Since the surface is not fully neutralized before the following drop slide on the surface, the next drop accumulates less charge. So the charge value per drop is influenced by two processes, charge neutralization process and accumulation process. When the two processes reach a dynamic equilibrium state, the charge is saturated at a steady state, e.g. in **Figure 6.2b**, from 200 to 1000 drops.

Charge on Lubricant-infused Surfaces

In contrast to PDMS surfaces, on lubricant-infused PDMS the first drops carried no detectable charge (**Figure 6.3a,b**). Whether no charge separation occurs at all (e.g. due to the different flow profiles near the contact line) or if charges on the lubricant are so mobile that they recombine with charge in the drop is not clear. For low drop numbers (n < 100) any charge deposited on the fluid lubricant layer is mobile and could immediately recombine. As a result, water drops do not charge at all. With increasing drop number, the drop charge on lubricant-infused PDMS increased first, showed a maximum and finally decreased to reach a saturation value. In the examples shown in **Figure 6.3a,b**, the maximum charge was 0.60 nC for PDMS-10 and 0.80 nC on PDMS-20. After 1000 and 2000 drops, it saturated at 0.38 nC ± 0.02 nC and 0.28 nC ± 0.01 nC, respectively. On PDMS-5 and PDMS-15 (**Figure S6.5**), they showed a close maximum charge of 0.70 nC ± 0.03 nC, and a similar saturated charge of 0.25 nC ± 0.03 nC. On lubricant-infused SU8, the drop charge also started from ca. 0 nC. Afterwards, it underwent increase, decrease, and saturation (**Figure 6.3c**). For the SU8 surfaces without lubricant, the drop charge (starting from ca. 0.03 nC) showed the same trend as that on pristine PDMS surfaces (**Figure S6.6**).

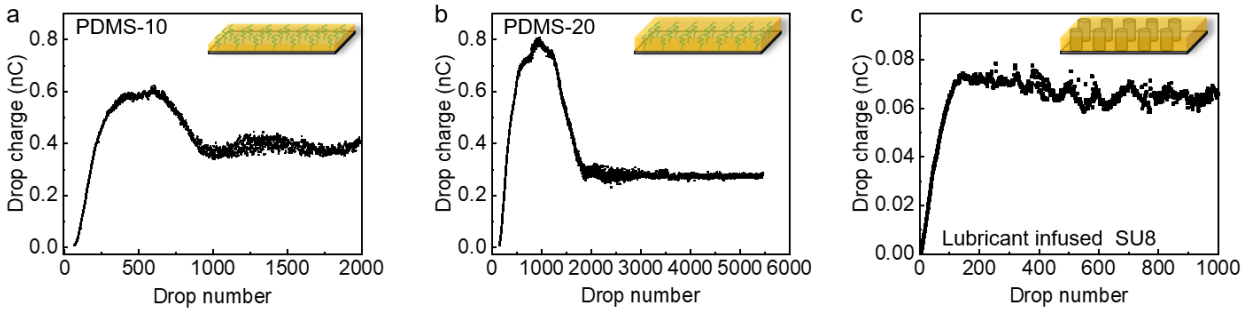

Figure 6.3 Slide electrification on lubricant-infused surfaces. Drop charge as a function of drop number on (a) PDMS-10, (b) PDMS-20, and (c) lubricant-infused SU8. Inset: schematic of (a) PDMS-10, (b) PDMS-20, (c) lubricant-infused SU8. Surface tilted angle: 50°. Water drop volume: 45 µL.

We explain this dependence of drop charge-versus-drop number by a depletion of lubricant and a resulting change of ion mobility; see below. For this reason, we first analyze the depletion of

lubricant. **Figure 6.4** shows the drop number, at which charge saturation is reached, as a function of lubricant thickness. The drop number at saturation increased with the increasing lubricant thickness. This indicates that the charge process is associated with the lubricant depletion on the PDMS surfaces. We further calculated the depletion speed by dividing the depleted lubricant volume by the drop number at saturation. The total volume of depleted lubricant was estimated by *LwD*, where *L* is the slide length, w the width of the drop contact area and *D* the initial film thickness. It shows a constant depletion speed of 1.4 nL/drop ± 0.3 nL/drop. As schematically shown in **Figure 6.4b**, an annular wetting ridge and a cloaking layer are always formed when water drops slide on the lubricant-infused surfaces. [125, 219, 340] Therefore, the lubricant-depletion may be caused by the cloaking layer and meniscus.

To put the 1.4 nL/drop into perspective, we considered the case that the whole lubricant is removed as a cloaking layer, neglecting the meniscus. We assumed that the whole volume of 1.4 nL is contained in a homogeneous layer of thickness *d* on the drop surface. At an apparent contact angle of 98° ± 2° and a drop volume of V = 45 µL the free surface area was A = 61 mm^2 leading to $d = V/A$ = 23 nm ± 5 nm. Thus, we estimate that every drop takes a layer of 23 nm away. On the time scale of drops sliding down the sample of ≈0.2 s such a layer can easily form driven by surface tension gradients (Marangoni effect).

We conclude that on an intact lubricant layer no charge is separated. With increasing drop number and decreasing thickness of the lubricant, surface conductivity also decreases. The drops get a chance to keep their drop charge and charging increases. Behind the drops, however, conductivity is still high enough to allow the surface to neutralize before the next drops comes. This fast neutralization of the surfaces allows subsequent drops to acquire a high charge because they are not limited by the surface charges deposited by previous drops. Eventually, for n > 1000, surface conductivity is so low that charges deposited by previous drops are still present and limit charging.

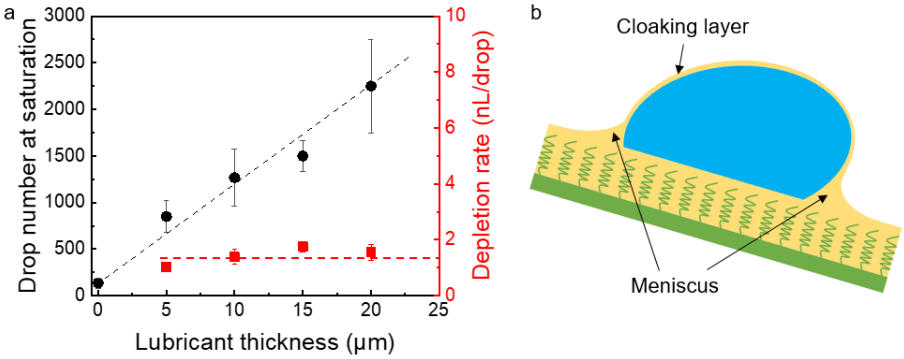

Figure 6.4 Lubricant depletion. (a) Drop number at saturation and depletion rate on different surfaces. Drop number at saturation means, after that drop number, the drop charge starts to be saturated. (b): Schematic showing the cloaking layer and meniscus.

Quantitatively this is described by the model in our previous work. [320] The charge acquired by a drop in steady state under steady state conditions is

$$Q_\infty = -\sigma_S w\lambda \quad 1 - e^{-\frac{L}{\lambda}\left(1-e^{-\Delta t/\tau}\right)} \quad = -\sigma_S w\lambda \quad 1 - e^{-\frac{L}{\lambda}} e^{\frac{L}{\lambda}e^{-\Delta t/\tau}} \qquad \text{(Equation 6.2)}$$

Here, σ_S is the surface charge density deposited by the first drop to the substrate at the beginning of its path, w is the width of the contact area of the drop, λ is a characteristic decay length of typically 1 cm, L is the slide length of the drop, Δt is the interval between subsequent drops and τ is the relaxation time for surface charge neutralization. The message of the equation is: Drop charge is maximal if the surface has a chance to discharge between two subsequent drops. For drop number above n = 300-1000 the opposite happens. Surface conductivity decreases, τ increases above Δt = 2 s and the steady state charge decreases to a value as for the pristine PDMS surface.

In addition, the meniscus of lubricant formed around the drop periphery may change the flow profile of water near the contact line. Since charge separation is attributed to the flow driving away the counterions in the electric double layer, a changed flow profile near the contact line may change charge separation.

Drop Velocity on Lubricant-infused Surfaces

To further verify the depletion process, we measured the sliding velocity of continuous drops on lubricant-infused surfaces (**Figure 6.5**). Similar with the charge results, the velocity of drops on lubricant-infused surfaces was different from that on pristine PDMS. On PDMS-0, the drop reached a velocity of 0.40 m/s ± 0.01 m/s after sliding 4 cm at a tilt angle of 50°. On all lubricant-infused PDMS surfaces, the drop velocity of the first 1000 drops only reached 0.24 m/s ± 0.04 m/s after 4 cm. We attribute the lower velocity of water drops on lubricant-infused surfaces to viscous dissipation caused by meniscus formation and movement of the meniscus. [160, 341, 342] In addition, a Marangoni effect caused by the flow in the sliding drop and a resulting variation in the thickness of the PDMS cloaking layer may lead to an increased friction of drops. Such a Marangoni effect is largely independent on clocking layer thickens, this is constant with our experimental results (**Figure S6.7**). Meanwhile, it has been demonstrated before that even tiny gradients in the surface tension of the liquid can induce substantial changes in dynamic contact angles and thus drop motion.[39] After 1000 drops, the drop velocity started to increase, and finally, it reached a velocity of 0.39 m/s ± 0.03 m/s after 4cm, which is close to that on PDMS-0. This verifies that the continuous drop sliding on the surface removes lubricant. After enough drops, the lubricant would be consumed, and the surface would turn back to pristine PDMS. For comparison, we also studied lubricant-infused SU8 micropillar arrays (**Figure 6.5d**). The velocity of water drops started from 0.16 m/s ± 0.01 m/s for the first drop, and increased to 0.25 m/s ± 0.03 m/s after 1000 drops. This is consistent with that on lubricant-infused PDMS.

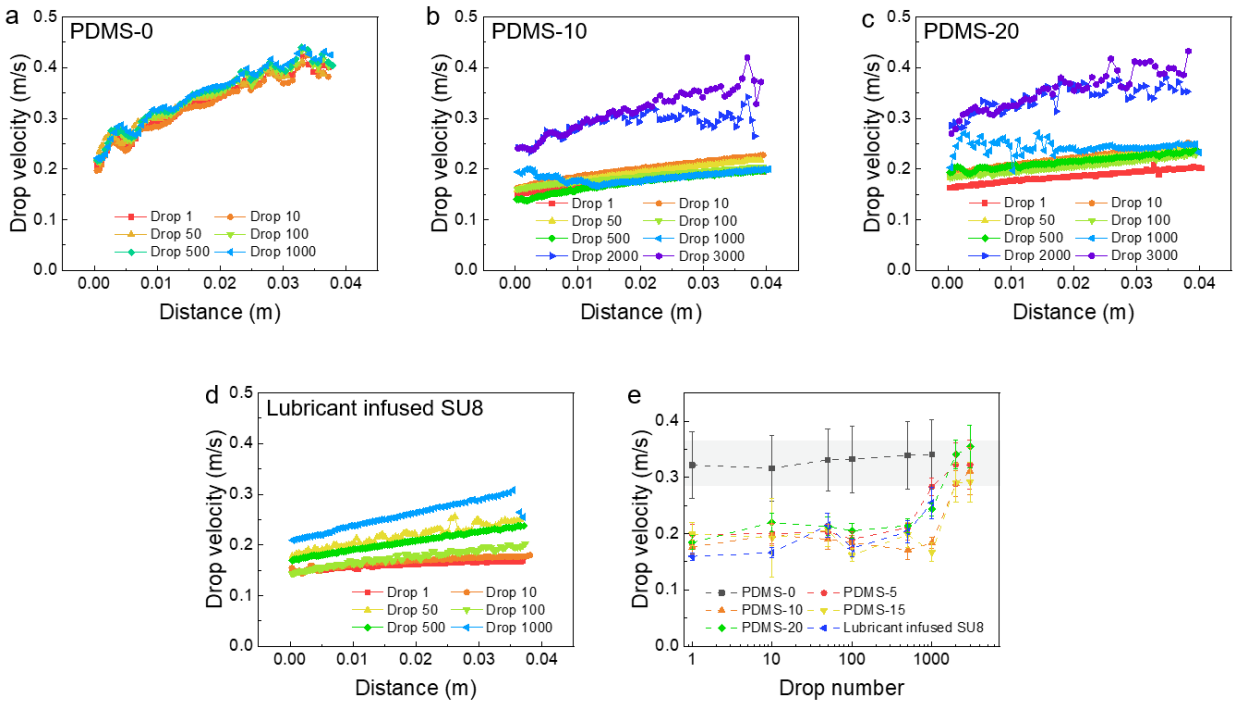

Figure 6.5 Drop Sliding Velocity on Surfaces. Drop velocities on (a) PDMS-0, (b) PDMS-10, (c) PDMS-20, and (d) lubricant-infused SU8. (e) Concluded average drop velocity as a function of drop number on lubricant-infused surfaces. Surface tilted angle: 50°. Water drop volume: 45 µL.

6.4 Conclusions

Spontaneous charging of water drops sliding over lubricant-infused surfaces shows a characteristic dependence on drop number. The first drops in a series (n < 100) are not or only little charged. We attribute this weak charging to a high mobility of charges on a lubricant layer, which effectively prevents charge separation. Then lubricant is depleted. In parallel, the charge per drop goes through a maximum. This maximum is reached when the mobility of ions is low enough to allow for spontaneous charging but high enough to discharge between subsequent drops. Finally, the charge per drop decreases until it saturates. The saturated charge per drop is similar as that on non-lubricant hydrophobic surfaces. The investigations here not only provide a fundamental understanding of drop charge on lubricant-infused surfaces, it may also depict a

guideline (e.g. by adjusting surface conductivity) to optimize the devices for more efficient electrification.

6.5 Appendix IV

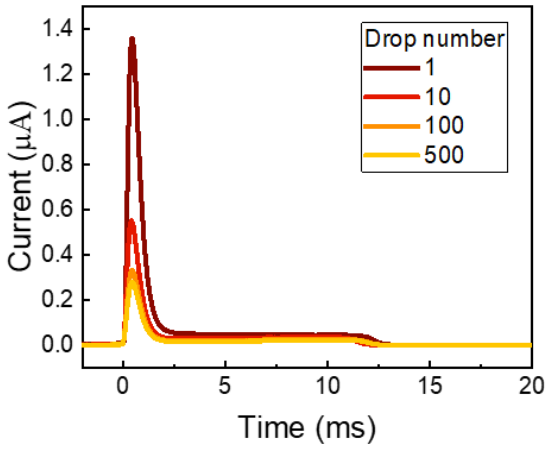

Figure S6.1 Measured drop current versus time for drop 1, 10, 100, and 500 on PDMS surface.

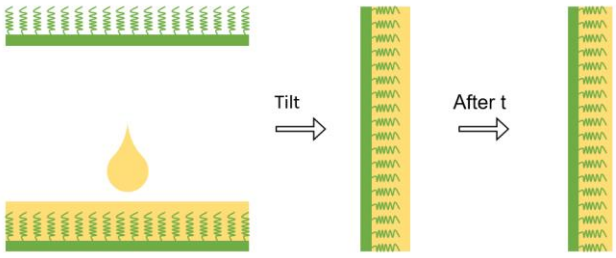

Figure S6.2 Preparation of lubricant infused PDMS.

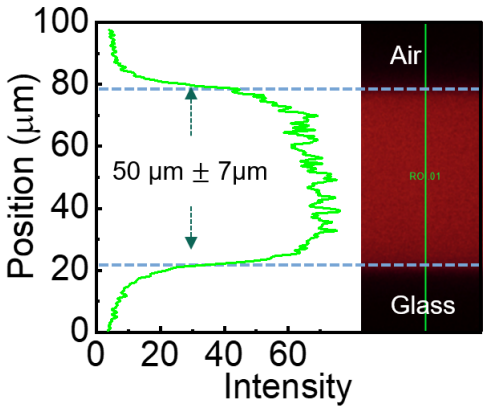

Figure S6.3 Intensity curve of the lubricant in z direction of surface PDMS-50.

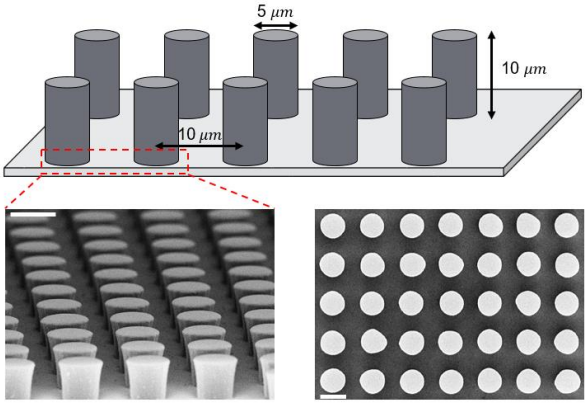

Figure S6.4 Schematic of SU8 and its SEM images. Scale bar: 10 μm.

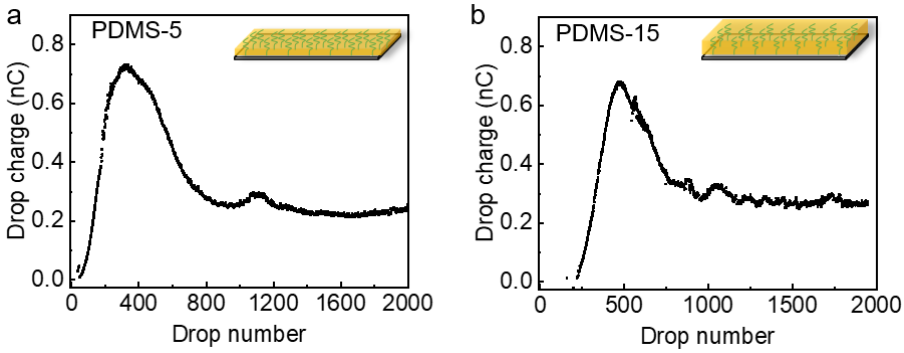

Figure S6.5 Charge of water drop on PDMS-5 and PDMS-15.

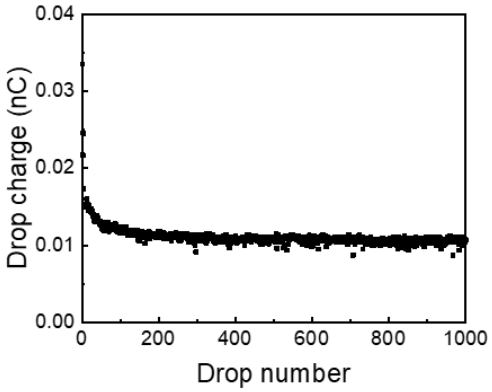

Figure S6.6 Charge of water drop on SU8 without lubricant.

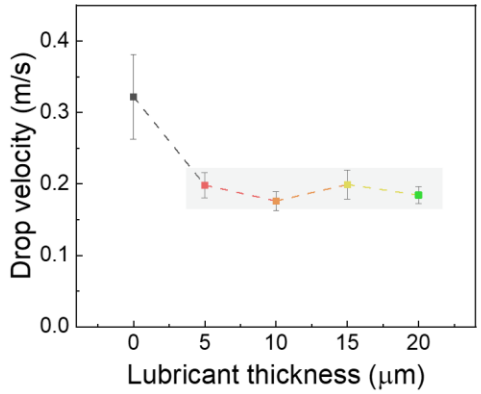

Figure S6.7 Water drop velocity on surfaces with different lubricant thickness.

7. Conclusion

This thesis focuses on the droplet dynamics on PDMS brushes and its development, characterization, and applications. PDMS brushes is adopted to be used in many applications, e.g. water harvesting, condensation heat transfer, and slide electrification. The first project deals with the vapor lubricated PDMS brushes for enhancing the mobility of water drops; the second project deals with the contact angle variation on PDMS brushes in different vapors; the third project deals with the enhanced condensation heat transfer by binary liquids on PDMS brushes; the forth project deals with the slide electrification of lubricant-infused PDMS brushes.

The first project demonstrated how the later adhesion of water and ice on PDMS brushes can be reduced in the presence of organic vapors, e.g. toluene or hexane vapor. I obtained the direct evidence using atomic force microscopy that PDMS brushes can adsorb toluene vapor molecules, be swelled and form a lubricating layer. With vapor adsorption, the sliding angle for water drops was reduced, the sliding velocity of water drops increased, leading to its wide potential applications. For example, in the presence of toluene vapor, the departure volume of water drops was reduced by an order of magnitude, the water collection rate was increased by 65%, when compared to that in air. Furthermore, vapor lubrication showed its potential in drop manipulation and anti-icing applications (lateral adhesion of ice was significantly reduced). The project here may help to solve the freezing-induced block of natural gas pipelines in cold areas.

In the second project, I investigated how and why the contact angles change on hydrophobic surfaces in the presence of different vapors. Water advancing and receding contact angles did not change significantly for water-immiscible vapors. In water-soluble vapors, a substantial decreased contact angles were detected. This decrease are explained well by Young’s equation. The decreased contact angle hysteresis on PDMS cannot be explained by Young’s equation. I attribute it to an uptake of vapor by the PDMS and the formation of a lubricating layer. The project

here helps people to better understand the contact angle phenomenon and contributes to various applications, e.g. water collection, heat transfer, and power generation.

In the third project, I studied the condensation heat transfer performance of ethanol-water mixtures on PDMS brushes. The condensation of binary liquids exhibited a high nucleation and growth rate, while allowing for the rapid droplet departure on our PDMS brushes. By balancing the nucleation energy barrier and the latent heat of vaporization of the condensate, the heat transfer coefficient of binary condensation on PDMS brushes was increased by more than 1800% as compared to the filmwise condensation of ethanol. Moreover, the binary liquids can substantially accelerate the droplet coalescence, thus preventing the dropwise-to-filmwise transition of condensed droplets under high heat flux conditions. My exploration of condensation dynamics for the binary liquids can help to fundamentally improve the interfacial phase change processes in a wide range of applications such as power generation and thermal management, which are important to increase global energy efficiency and reduce carbon emissions.

In the last project, I investigated the slide electrification of water drops on lubricant-infused PDMS brushes. Spontaneous charging of water drops sliding over lubricant-infused PDMS brushes shows a characteristic dependence on drop number, which is different from that on conventional hydrophobic surfaces. The first drops in a series ($n < 100$) are not or only little charged. I attribute this weak charging to a high mobility of charges on a lubricant layer, which effectively prevents charge separation. Afterwards, the charge per drop increases and goes through a maximum, due to the lubricant depletion. This maximum is reached when the mobility of ions is low enough to allow for spontaneous charging but high enough to discharge between subsequent drops. Finally, the charge per drop decreases until it saturates, where the value is similar with that on PDMS brushes without lubricant. The investigations here not only provide a fundamental understanding of drop charge on lubricant-infused surfaces, it may also depict a guideline (e.g. by adjusting surface conductivity) to optimize the devices for more efficient electrification.

The surface property that interact with matter, e.g. PDMS brushes towards kinds of liquids, are essential in many aspects. These four parts of my PhD project deals with droplet dynamics on PDMS brushes and successfully proves the strong potential of PDMS brushes to be used in various applications. Further steps can be taken to characterize PDMS brushes in industrial level or bring it to other related applications.

References

1. Young, T., III. An essay on the cohesion of fluids*. Philosophical Transactions of the Royal Society of London*, **1805**. 95: 65-87.

2. Wenzel, R.N., Resistance of solid surfaces to wetting by water*. Industrial & Engineering Chemistry*, **1936**. 28(8): 988-994.

3. Wenzel, R.N., Surface roughness and contact angle*. The Journal of Physical and Colloid Chemistry*, **1949**. 53(9): 1466-1467.

4. Cassie, A.B.D. and Baxter, S., Wettability of porous surfaces*. Transactions of the Faraday Society*, **1944**. 40: 546-551.

5. Cassie, A., Contact angles*. Discussions of the Faraday Society*, **1948**. 3: 11-16.

6. Pierce, E., Carmona, F.J., and Amirfazli, A., Understanding of sliding and contact angle results in tilted plate experiments*. Colloids and Surfaces A: Physicochemical and Engineering Aspects*, **2008**. 323(1): 73-82.

7. Schellenberger, F., Encinas, N., Vollmer, D., et al., How water advances on superhydrophobic surfaces*. Physical Review Letters*, **2016**. 116(9): 096101.

8. Butt, H.-J., Liu, J., Koynov, K., et al., Contact angle hysteresis*. Current Opinion in Colloid & Interface Science*, **2022**. 59: 101574.

9. Korhonen, J.T., Huhtamäki, T., Ikkala, O., et al., Reliable measurement of the receding contact angle*. Langmuir*, **2013**. 29(12): 3858-3863.

10. Gaudin, A., Witt, A., and Decker, T., Contact angle hysteresis-Principles and application of measurement methods*. Transactions of the Society of Mining Engineers of AIME*, **1963**. 226(1): 107-112.

11. Timmons, C.O. and Zisman, W.A., The effect of liquid structure on contact angle hysteresis*. Journal of Colloid and Interface Science*, **1966**. 22(2): 165-171.

12. Holly, F.J. and Refojo, M.F., Wettability of hydrogels I. Poly(2-hydroxyethyl methacrylate)*. Journal of Biomedical Materials Research*, **1975**. 9(3): 315-326.

13. Yasuda, H., Sharma, A.K., and Yasuda, T., Effect of orientation and mobility of polymer molecules at surfaces on contact angle and its hysteresis*. Journal of Polymer Science: Polymer Physics Edition*, **1981**. 19(9): 1285-1291.

14. Macdougall, G., Ockrent, C., and Kendall, J.P., Surface energy relations in liquid/solid systems I. The adhesion of liquids to solids and a new method of determining the surface tension

of liquids*. Proceedings of the Royal Society of London. Series A. Mathematical and Physical Sciences*, **1942**. 180(981): 151-173.

15. Kawasaki, K., Study of wettability of polymers by sliding of water drop*. Journal of Colloid Science*, **1960**. 15(5): 402-407.

16. Le Grand, N., Daerr, A., and Limat, L., Shape and motion of drops sliding down an inclined plane*. Journal of Fluid Mechanics*, **2005**. 541: 293-315.

17. Yilbas, B.S., Al-Sharafi, A., Ali, H., et al., Dynamics of a water droplet on a hydrophobic inclined surface: influence of droplet size and surface inclination angle on droplet rolling*. RSC Advances*, **2017**. 7(77): 48806-48818.

18. Guo, Z., Liu, W., and Su, B.-L., Superhydrophobic surfaces: From natural to biomimetic to functional*. Journal of Colloid and Interface Science*, **2011**. 353(2): 335-355.

19. Ma, M. and Hill, R.M., Superhydrophobic surfaces*. Current Opinion in Colloid & Interface Science*, **2006**. 11(4): 193-202.

20. Sun, T., Feng, L., Gao, X., et al., Bioinspired surfaces with special wettability*. Accounts of Chemical Research*, **2005**. 38(8): 644-652.

21. Wong, T.S., Kang, S.H., Tang, S.K., et al., Bioinspired self-repairing slippery surfaces with pressure-stable omniphobicity*. Nature*, **2011**. 477(7365): 443-7.

22. Lafuma, A. and Quéré, D., Slippery pre-suffused surfaces*. Europhysics Letters*, **2011**. 96(5): 56001.

23. Smith, J.D., Dhiman, R., and Varanasi, K. Liquid-encapsulating surfaces: overcoming the limitations of superhydrophobic surfaces for robust non-wetting and anti-icing surfaces. in *APS division of fluid dynamics meeting abstracts*. **2011**.

24. Lv, J., Song, Y., Jiang, L., et al., Bio-inspired strategies for anti-icing*. ACS Nano*, **2014**. 8(4): 3152-3169.

25. Tu, Y., Wang, R., Zhang, Y., et al., Progress and expectation of atmospheric water harvesting*. Joule*, **2018**. 2(8): 1452-1475.

26. Cho, H.J., Preston, D.J., Zhu, Y., et al., Nanoengineered materials for liquid–vapour phase-change heat transfer*. Nature Reviews Materials*, **2016**. 2(2): 16092.

27. Banerjee, I., Pangule, R.C., and Kane, R.S., Antifouling coatings: Recent developments in the design of surfaces that prevent fouling by proteins, bacteria, and marine organisms*. Advanced Materials*, **2011**. 23(6): 690-718.

28. Buddingh, J.V., Hozumi, A., and Liu, G., Liquid and liquid-like surfaces/coatings that readily slide fluids*. Progress in Polymer Science*, **2021**. 123: 101468.

29. Wooh, S. and Vollmer, D., Silicone brushes: omniphobic surfaces with low sliding angles. *Angewandte Chemie International Edition*, **2016**. 55(24): 6822-6824.

30. Khatir, B. and Golovin, K., Vapor alteration alone reduces water droplet adhesion. *Advanced Materials*, **2023**: 2208783.

31. Feng, X.J. and Jiang, L., Design and creation of superwetting/antiwetting surfaces. *Advanced Materials*, **2006**. 18(23): 3063-3078.

32. Lafuma, A. and Quéré, D., Superhydrophobic states. *Nature Materials*, **2003**. 2(7): 457-460.

33. Leidenfrost, J.G., On the fixation of water in diverse fire. *International Journal of Heat and Mass Transfer*, **1966**. 9(11): 1153-1166.

34. Leidenfrost, J.G., De aquae communis nonnullis qualitatibus tractatus. **1756**, Duisburg: Ovenius.

35. Schutzius, T.M., Jung, S., Maitra, T., et al., Spontaneous droplet trampolining on rigid superhydrophobic surfaces. *Nature*, **2015**. 527(7576): 82-5.

36. Papadopoulos, P., Mammen, L., Deng, X., et al., How superhydrophobicity breaks down. *Proceedings of the National Academy of Sciences*, **2013**. 110(9): 3254-3258.

37. Kusumaatmaja, H., Blow, M.L., Dupuis, A., et al., The collapse transition on superhydrophobic surfaces. *Europhysics Letters*, **2008**. 81(3): 36003.

38. Bormashenko, E., Pogreb, R., Whyman, G., et al., Cassie-Wenzel wetting transition in vibrating drops deposited on rough surfaces: Is the dynamic Cassie-Wenzel wetting transition a 2d or 1d affair? *Langmuir*, **2007**. 23(12): 6501-6503.

39. Bartolo, D., Bouamrirene, F., Verneuil, É., et al., Bouncing or sticky droplets: Impalement transitions on superhydrophobic micropatterned surfaces. *Europhysics Letters*, **2006**. 74(2): 299-305.

40. Reyssat, M., Yeomans, J.M., and Quéré, D., Impalement of fakir drops. *Europhysics Letters*, **2007**. 81(2): 26006.

41. Wong, T.S., Kang, S.H., Tang, S.K., et al., Bioinspired self-repairing slippery surfaces with pressure-stable omniphobicity. *Nature*, **2011**. 477(7365): 443-447.

42. Smith, J.D., Dhiman, R., Anand, S., et al., Droplet mobility on lubricant-impregnated surfaces. *Soft Matter*, **2013**. 9(6): 1772-1780.

43. Schellenberger, F., Xie, J., Encinas, N., et al., Direct observation of drops on slippery lubricant-infused surfaces. *Soft Matter*, **2015**. 11(38): 7617-7626.

44. Semprebon, C., McHale, G., and Kusumaatmaja, H., Apparent contact angle and contact angle hysteresis on liquid infused surfaces. *Soft Matter*, **2017**. 13(1): 101-110.

45. Lam, C.N.C., Wu, R., Li, D., et al., Study of the advancing and receding contact angles: liquid sorption as a cause of contact angle hysteresis*. Advances in Colloid and Interface Science*, **2002**. 96(1): 169-191.

46. He, B., Lee, J., and Patankar, N.A., Contact angle hysteresis on rough hydrophobic surfaces*. Colloids and Surfaces A: Physicochemical and Engineering Aspects*, **2004**. 248(1): 101-104.

47. Gao, L. and McCarthy, T.J., Contact angle hysteresis explained*. Langmuir*, **2006**. 22(14): 6234-6237.

48. Extrand, C.W. and Kumagai, Y., An experimental study of contact angle hysteresis*. Journal of Colloid and Interface Science*, **1997**. 191(2): 378-383.

49. Eral, H.B., Mannetje, D.J.C.M., and Oh, J.M., Contact angle hysteresis: a review of fundamentals and applications*. Colloid and Polymer Science*, **2013**. 291(2): 247-260.

50. Harkins, W.D. and Brown, F.E., The determination of surface tension (free surface energy), and the weight of falling drops: The surface tension of water and benzene by the capillary height method*. Journal of the American Chemical Society*, **1919**. 41(4): 499-524.

51. Bartell, F.E. and Wooley, A.D., Solid—liquid—air contact angles and their dependence upon the surface condition of the solid*. Journal of the American Chemical Society*, **1933**. 55(9): 3518-3527.

52. Schäffer, E. and Wong, P.-z., Contact line dynamics near the pinning threshold: A capillary rise and fall experiment*. Physical Review E*, **2000**. 61(5): 5257-5277.

53. Johnson, R.E., Dettre, R.H., and Brandreth, D.A., Dynamic contact angles and contact angle hysteresis*. Journal of Colloid and Interface Science*, **1977**. 62(2): 205-212.

54. Johnson, R., Wettability and contact angles. *Surface and Colloid Science*, ed. M. E. Vol. 2. **1969**, New York: Wiley. 85-153.

55. Vergelati, C., Perwuelz, A., Vovelle, L., et al., Poly(ethylene terephthalate) surface dynamics in air and water studied by tensiometry and molecular modelling*. Polymer*, **1994**. 35(2): 262-270.

56. Tretinnikov, O.N. and Ikada, Y., Dynamic wetting and contact angle hysteresis of polymer surfaces studied with the modified wilhelmy balance method*. Langmuir*, **1994**. 10: 1606-1614.

57. Rolley, E. and Guthmann, C., Dynamics and hysteresis of the contact line between liquid hydrogen and cesium substrates*. Physical Review Letters*, **2007**. 98(16): 166105.

58. Perrin, H., Lhermerout, R., Davitt, K., et al., Thermally activated motion of a contact line over defects*. Soft Matter*, **2018**. 14(9): 1581-1595.

59. Kim, J.-H., Kavehpour, H.P., and Rothstein, J.P., Dynamic contact angle measurements on superhydrophobic surfaces*. Physics of Fluids*, **2015**. 27(3): 032107.

60. Blake, T.D. and Shikhmurzaev, Y.D., Dynamic wetting by liquids of different viscosity. *Journal of Colloid and Interface Science*, **2002**. 253(1): 196-202.
61. Petrov, J.G., Ralston, J., Schneemilch, M., et al., Dynamics of partial wetting and dewetting in well-defined systems. *The Journal of Physical Chemistry B*, **2003**. 107(7): 1634-1645.
62. Vega, M.J., Gouttière, C., Seveno, D., et al., Experimental investigation of the link between static and dynamic wetting by forced wetting of Nylon filament. *Langmuir*, **2007**. 23(21): 10628-10634.
63. Extrand, C.W. and Kumagai, Y., Liquid drops on an inclined plane: The relation between contact angles, drop shape, and retentive force. *Journal of Colloid and Interface Science*, **1995**. 170(2): 515-521.
64. Furmidge, C., Studies at phase interfaces. I. The sliding of liquid drops on solid surfaces and a theory for spray retention. *Journal of colloid science*, **1962**. 17(4): 309-324.
65. Cao, L., Jones, A.K., Sikka, V.K., et al., Anti-icing superhydrophobic coatings. *Langmuir*, **2009**. 25(21): 12444-12448.
66. Farhadi, S., Farzaneh, M., and Kulinich, S.A., Anti-icing performance of superhydrophobic surfaces. *Applied Surface Science*, **2011**. 257(14): 6264-6269.
67. Kreder, M.J., Alvarenga, J., Kim, P., et al., Design of anti-icing surfaces: smooth, textured or slippery? *Nature Reviews Materials*, **2016**. 1(1): 1-15.
68. Guo, P., Zheng, Y., Wen, M., et al., Icephobic/anti-icing properties of micro/nanostructured surfaces. *Advanced Materials*, **2012**. 24(19): 2642-8.
69. Park, H., Choi, C.-H., and Kim, C.-J., Superhydrophobic drag reduction in turbulent flows: a critical review. *Experiments in Fluids*, **2021**. 62(11): 229.
70. Daniello, R.J., Waterhouse, N.E., and Rothstein, J.P., Drag reduction in turbulent flows over superhydrophobic surfaces. *Physics of Fluids*, **2009**. 21(8): 085103.
71. Park, H., Sun, G., and Kim, C.-J.C., Superhydrophobic turbulent drag reduction as a function of surface grating parameters. *Journal of Fluid Mechanics*, **2014**. 747: 722-734.
72. Tuo, Y., Zhang, H., Rong, W., et al., Drag reduction of anisotropic superhydrophobic surfaces prepared by laser etching. *Langmuir*, **2019**. 35(34): 11016-11022.
73. Tian, X., Verho, T., and Ras, R.H.A., Moving superhydrophobic surfaces toward real-world applications. *Science*, **2016**. 352(6282): 142-143.
74. Chavan, S., Cha, H., Orejon, D., et al., Heat transfer through a condensate droplet on hydrophobic and nanostructured superhydrophobic surfaces. *Langmuir*, **2016**. 32(31): 7774-7787.
75. Miljkovic, N. and Wang, E.N., Condensation heat transfer on superhydrophobic surfaces. *MRS Bulletin*, **2013**. 38(5): 397-406.

76. Enright, R., Miljkovic, N., Al-Obeidi, A., et al., Condensation on superhydrophobic surfaces: the role of local energy barriers and structure length scale*. Langmuir*, **2012**. 28(40): 14424-144232.

77. Guo, Z. and Liu, W., Biomimic from the superhydrophobic plant leaves in nature: Binary structure and unitary structure*. Plant Science*, **2007**. 172(6): 1103-1112.

78. Barthlott, W. and Neinhuis, C., Purity of the sacred lotus, or escape from contamination in biological surfaces*. Planta*, **1997**. 202(1): 1-8.

79. Solga, A., Cerman, Z., Striffler, B.F., et al., The dream of staying clean: Lotus and biomimetic surfaces*. Bioinspiration & Biomimetics*, **2007**. 2(4): 126-134.

80. Dettre, R. and Johnson, R., Contact angle hysteresis-porous surfaces*. SCI Monograph*, **1967**. 25: 144-163.

81. Onda, T., Shibuichi, S., Satoh, N., et al., Super-water-repellent fractal surfaces*. Langmuir*, **1996**. 12(9): 2125-2127.

82. Wang, S., Feng, L., and Jiang, L., One-step solution-immersion process for the fabrication of stable bionic superhydrophobic surfaces*. Advanced Materials*, **2006**. 18(6): 767-770.

83. Feng, X., Feng, L., Jin, M., et al., Reversible super-hydrophobicity to super-hydrophilicity transition of aligned zno nanorod films*. Journal of the American Chemical Society*, **2004**. 126(1): 62-63.

84. Qu, M., Zhang, B., Song, S., et al., Fabrication of superhydrophobic surfaces on engineering materials by a solution-immersion process*. Advanced Functional Materials*, **2007**. 17(4): 593-596.

85. Geyer, F., D'Acunzi, M., Yang, C.-Y., et al., How to coat the inside of narrow and long tubes with a super-liquid-repellent layer—A promising candidate for antibacterial catheters*. Advanced Materials*, **2019**. 31(2): 1801324.

86. Wang, D., Guo, Z., Chen, Y., et al., In situ hydrothermal synthesis of nanolamellate $CaTiO_3$ with controllable structures and wettability*. Inorganic Chemistry*, **2007**. 46(19): 7707-7709.

87. Shiu, J.-Y., Kuo, C.-W., Chen, P., et al., Fabrication of tunable superhydrophobic surfaces by nanosphere lithography*. Chemistry of Materials*, **2004**. 16(4): 561-564.

88. Öner, D. and McCarthy, T.J., Ultrahydrophobic surfaces. Effects of topography length scales on wettability*. Langmuir*, **2000**. 16(20): 7777-7782.

89. Callies, M., Chen, Y., Marty, F., et al., Microfabricated textured surfaces for super-hydrophobicity investigations*. Microelectronic Engineering*, **2005**. 78-79: 100-105.

90. Xia, Y. and Whitesides, G.M., Soft lithography*. Angewandte Chemie International Edition*, **1998**. 37(5): 550-575.

91. Xia, Y., McClelland, J.J., Gupta, R., et al., Replica molding using polymeric materials: A practical step toward nanomanufacturing. *Advanced Materials*, **1997**. 9(2): 147-149.
92. Ma, M., Mao, Y., Gupta, M., et al., Superhydrophobic fabrics produced by electrospinning and chemical vapor deposition. *Macromolecules*, **2005**. 38(23): 9742-9748.
93. Artus, G.R.J., Jung, S., Zimmermann, J., et al., Silicone nanofilaments and their application as superhydrophobic coatings. *Advanced Materials*, **2006**. 18(20): 2758-2762.
94. Zhang, J. and Seeger, S., Superoleophobic coatings with ultralow sliding angles based on silicone nanofilaments. *Angewandte Chemie International Edition*, **2011**. 50(29): 6652-6656.
95. Deng, X., Mammen, L., Butt, H.-J., et al., Candle soot as a template for a transparent robust superamphiphobic coating. *Science*, **2012**. 335(6064): 67-70.
96. Teisala, H., Geyer, F., Haapanen, J., et al., Ultrafast processing of hierarchical nanotexture for a transparent superamphiphobic coating with extremely low roll-off angle and high impalement pressure. *Advanced Materials*, **2018**. 30(14): 1706529.
97. Jafari, R., Asadollahi, S., and Farzaneh, M., Applications of plasma technology in development of superhydrophobic surfaces. *Plasma Chemistry and Plasma Processing*, **2013**. 33(1): 177-200.
98. Lu, X., Zhang, C., and Han, Y., Low-density polyethylene superhydrophobic surface by control of its crystallization behavior. *Macromolecular Rapid Communications*, **2004**. 25(18): 1606-1610.
99. García, N., Benito, E., Guzmán, J., et al., Use of p-toluenesulfonic acid for the controlled grafting of alkoxysilanes onto silanol containing surfaces: Preparation of tunable hydrophilic, hydrophobic, and super-hydrophobic silica. *Journal of the American Chemical Society*, **2007**. 129(16): 5052-5060.
100. Bravo, J., Zhai, L., Wu, Z., et al., Transparent superhydrophobic films based on silica nanoparticles. *Langmuir*, **2007**. 23(13): 7293-7298.
101. Larmour, I.A., Bell, S.E.J., and Saunders, G.C., Remarkably simple fabrication of superhydrophobic surfaces using electroless galvanic deposition. *Angewandte Chemie International Edition*, **2007**. 46(10): 1710-1712.
102. Wang, D., Sun, Q., Hokkanen, M.J., et al., Design of robust superhydrophobic surfaces. *Nature*, **2020**. 582(7810): 55-59.
103. Tourkine, P., Le Merrer, M., and Quéré, D., Delayed freezing on water repellent materials. *Langmuir*, **2009**. 25(13): 7214-7216.
104. Mishchenko, L., Hatton, B., Bahadur, V., et al., Design of ice-free nanostructured surfaces based on repulsion of impacting water droplets. *ACS Nano*, **2010**. 4(12): 7699-707.

105. Ruan, M., Li, W., Wang, B., et al., Preparation and anti-icing behavior of superhydrophobic surfaces on aluminum alloy substrates*. Langmuir*, **2013**. 29(27): 8482-8491.

106. Bahadur, V., Mishchenko, L., Hatton, B., et al., Predictive model for ice formation on superhydrophobic surfaces*. Langmuir*, **2011**. 27(23): 14143-14150.

107. Alizadeh, A., Yamada, M., Li, R., et al., Dynamics of ice nucleation on water repellent surfaces*. Langmuir*, **2012**. 28(6): 3180-3186.

108. Eberle, P., Tiwari, M.K., Maitra, T., et al., Rational nanostructuring of surfaces for extraordinary icephobicity*. Nanoscale*, **2014**. 6(9): 4874-4881.

109. Wang, Y., Xue, J., Wang, Q., et al., Verification of icephobic/anti-icing properties of a superhydrophobic surface*. ACS Applied Materials & Interfaces*, **2013**. 5(8): 3370-3381.

110. Kulinich, S.A. and Farzaneh, M., How wetting hysteresis influences ice adhesion strength on superhydrophobic surfaces*. Langmuir*, **2009**. 25(16): 8854-8856.

111. Wen, R., Ma, X., Lee, Y., et al., Liquid-vapor phase-change heat transfer on functionalized nanowired surfaces and beyond*. Joule*, **2018**. 2(11): 2307-2347.

112. Miljkovic, N., Enright, R., Nam, Y., et al., Jumping-droplet-enhanced condensation on scalable superhydrophobic nanostructured surfaces*. Nano Letters*, **2013**. 13(1): 179-187.

113. Enright, R., Miljkovic, N., Sprittles, J., et al., How coalescing droplets jump*. ACS Nano*, **2014**. 8(10): 10352-10362.

114. Wen, R., Xu, S., Ma, X., et al., Three-dimensional superhydrophobic nanowire networks for enhancing condensation heat transfer*. Joule*, **2018**. 2(2): 269-279.

115. Lo, C., Chu, Y., Yen, M., et al., Enhancing condensation heat transfer on three-dimensional hybrid surfaces*. Joule*, **2019**. 3(11): 2806-2823.

116. Kwon, H.-M., Paxson, A.T., Varanasi, K.K., et al., Rapid deceleration-driven wetting transition during pendant drop deposition on superhydrophobic surfaces*. Physical Review Letters*, **2011**. 106(3): 036102.

117. Manukyan, G., Oh, J.M., van den Ende, D., et al., Electrical switching of wetting states on superhydrophobic surfaces: A route towards reversible Cassie-to-Wenzel transitions*. Physical Review Letters*, **2011**. 106(1): 014501.

118. McHale, G., Aqil, S., Shirtcliffe, N.J., et al., Analysis of droplet evaporation on a superhydrophobic surface*. Langmuir*, **2005**. 21(24): 11053-11060.

119. Bohn, H.F. and Federle, W., Insect aquaplaning: Nepenthes pitcher plants capture prey with the peristome, a fully wettable water-lubricated anisotropic surface*. Proceedings of the National Academy of Sciences*, **2004**. 101(39): 14138-14143.

120. Bauer, U., Paulin, M., Robert, D., et al., Mechanism for rapid passive-dynamic prey capture in a pitcher plant. *Proceedings of the National Academy of Sciences*, **2015**. 112(43): 13384-13389.
121. Sunny, S., Vogel, N., Howell, C., et al., Lubricant-infused nanoparticulate coatings assembled by layer-by-layer deposition. *Advanced Functional Materials*, **2014**. 24(42): 6658-6667.
122. Peppou-Chapman, S., Hong, J.K., Waterhouse, A., et al., Life and death of liquid-infused surfaces: a review on the choice, analysis and fate of the infused liquid layer. *Chemical Society Reviews*, **2020**. 49(11): 3688-3715.
123. Chen, X., Wen, G., and Guo, Z., What are the design principles, from the choice of lubricants and structures to the preparation method, for a stable slippery lubricant-infused porous surface? *Materials Horizons*, **2020**. 7(7): 1697-1726.
124. Li, J., Ueda, E., Paulssen, D., et al., Slippery lubricant-infused surfaces: Properties and emerging applications. *Advanced Functional Materials*, **2019**. 29(4): 1802317.
125. Baumli, P., D'Acunzi, M., Hegner, K.I., et al., The challenge of lubricant-replenishment on lubricant-impregnated surfaces. *Advances in Colloid and Interface Science*, **2021**. 287: 102329.
126. Rosca, D.A., Wright, J.A., Hughes, D.L., et al., Gold peroxide complexes and the conversion of hydroperoxides into gold hydrides by successive oxygen-transfer reactions. *Nature Communications*, **2013**. 4: 2167.
127. Wang, P., Zhang, D., Lu, Z., et al., Fabrication of slippery lubricant-infused porous surface for inhibition of microbially influenced corrosion. *ACS Applied Materials & Interfaces*, **2016**. 8(2): 1120-7.
128. Weisensee, P.B., Wang, Y., Qian, H., et al., Condensate droplet size distribution on lubricant-infused surfaces. *International Journal of Heat and Mass Transfer*, **2017**. 109: 187-199.
129. Wang, J., Kato, K., Blois, A.P., et al., Bioinspired omniphobic coatings with a thermal self-repair function on industrial materials. *ACS Applied Materials & Interfaces*, **2016**. 8(12): 8265-71.
130. Kim, P., Wong, T.S., Alvarenga, J., et al., Liquid-infused nanostructured surfaces with extreme anti-ice and anti-frost performance. *ACS Nano*, **2012**. 6(8): 6569-77.
131. Sirohia, G.K. and Dai, X., Designing air-independent slippery rough surfaces for condensation. *International Journal of Heat and Mass Transfer*, **2019**. 140: 777-785.
132. Dai, X.M., Sun, N., Nielsen, S.O., et al., Hydrophilic directional slippery rough surfaces for water harvesting. *Science Advances*, **2018**. 4(3): eaaq0919.
133. Sun, J. and Weisensee, P.B., Microdroplet self-propulsion during dropwise condensation on lubricant-infused surfaces. *Soft Matter*, **2019**. 15(24): 4808-4817.

134. Dong, Z., Schumann, M.F., Hokkanen, M.J., et al., Superoleophobic slippery lubricant-infused surfaces: Combining two extremes in the same surface. *Advanced Materials*, **2018**. 30(45): 1803890.

135. Guo, J., Wang, D., Sun, Q., et al., Omni-liquid droplet manipulation platform. *Advanced Materials Interfaces*, **2019**. 6(16): 1900653.

136. Hao, C., Li, J., Liu, Y., et al., Superhydrophobic-like tunable droplet bouncing on slippery liquid interfaces. *Nature Communications*, **2015**. 6(1): 7986.

137. Lei, W., Bruchmann, J., Rüping, J.L., et al., Biofilm bridges forming structural networks on patterned lubricant-infused surfaces. *Advanced Science*, **2019**. 6(13): 1900519.

138. Zhang, B.J., Kim, K.J., and Lee, C.Y., Behavior of an evaporating water droplet on lubricant-impregnated nano-structured surface. *Experimental Thermal and Fluid Science*, **2018**. 96: 216-223.

139. Anand, S., Paxson, A.T., Dhiman, R., et al., Enhanced condensation on lubricant-impregnated nanotextured surfaces. *ACS Nano*, **2012**. 6(11): 10122-9.

140. Rykaczewski, K., Anand, S., Subramanyam, S.B., et al., Mechanism of frost formation on lubricant-impregnated surfaces. *Langmuir*, **2013**. 29(17): 5230-8.

141. Rykaczewski, K., Paxson, A.T., Staymates, M., et al., Dropwise condensation of low surface tension fluids on omniphobic surfaces. *Scientific Reports*, **2014**. 4: 4158.

142. Tsuruki, Y., Sakai, M., Isobe, T., et al., Static and dynamic hydrophobicity of alumina-based porous ceramics impregnated with fluorinated oil. *Journal of Materials Research*, **2014**. 29(14): 1546-1555.

143. Charpentier, T.V.J., Neville, A., Baudin, S., et al., Liquid infused porous surfaces for mineral fouling mitigation. *Journal of Colloid and Interface Science*, **2015**. 444: 81-86.

144. Wei, Q., Schlaich, C., Prévost, S., et al., Supramolecular polymers as surface coatings: Rapid fabrication of healable superhydrophobic and slippery surfaces. *Advanced Materials*, **2014**. 26(43): 7358-7364.

145. Rowthu, S., Balic, E.E., and Hoffmann, P., Molecular dimensions and surface diffusion assisted mechanically robust slippery perfluoropolyether impregnated mesoporous alumina interfaces. *Nanotechnology*, **2017**. 28(50): 505605.

146. Chen, J., Howell, C., Haller, C.A., et al., An immobilized liquid interface prevents device associated bacterial infection in vivo. *Biomaterials*, **2017**. 113: 80-92.

147. Waterhouse, A., Leslie, D.C., Lightbown, K., et al., Rapid coating process generates omniphobic dentures in minutes to reduce C. albicans biofouling. *ACS Biomaterials Science & Engineering*, **2019**. 5(2): 420-424.

148. Chang, C.-C., Wu, C.-J., Sheng, Y.-J., et al., Anti-smudge behavior of facilely fabricated liquid-infused surfaces with extremely low contact angle hysteresis property. *RSC Advances*, **2016**. 6(23): 19214-19222.

149. Zhang, J., Gu, C., and Tu, J., Robust slippery coating with superior corrosion resistance and anti-icing performance for AZ31B MG alloy protection. *ACS Applied Materials & Interfaces*, **2017**. 9(12): 11247-11257.

150. Wang, Y., Zhao, W., Wu, W., et al., Fabricating bionic ultraslippery surface on titanium alloys with excellent fouling-resistant performance. *ACS Applied Bio Materials*, **2019**. 2(1): 155-162.

151. Galvan, Y., Phillips, K.R., Haumann, M., et al., Ionic-liquid-infused nanostructures as repellent surfaces. *Langmuir*, **2018**. 34(23): 6894-6902.

152. Wang, X.Q., Gu, C.D., Wang, L.Y., et al., Ionic liquids-infused slippery surfaces for condensation and hot water repellency. *Chemical Engineering Journal*, **2018**. 343: 561-571.

153. Kajiya, T., Schellenberger, F., Papadopoulos, P., et al., 3D imaging of water-drop condensation on hydrophobic and hydrophilic lubricant-impregnated surfaces. *Scientific Reports*, **2016**. 6(1): 23687.

154. Miranda, D.F., Urata, C., Masheder, B., et al., Physically and chemically stable ionic liquid-infused textured surfaces showing excellent dynamic omniphobicity. *APL Materials*, **2014**. 2(5): 056108.

155. Sotiri, I., Tajik, A., Lai, Y., et al., Tunability of liquid-infused silicone materials for biointerfaces. *Biointerphases*, **2018**. 13(6): 06D401.

156. Eifert, A., Paulssen, D., Varanakkottu, S.N., et al., Simple fabrication of robust water-repellent surfaces with low contact-angle hysteresis based on impregnation. *Advanced Materials Interfaces*, **2014**. 1(3): 1300138.

157. Liu, H., Zhang, P., Liu, M., et al., Organogel-based thin films for self-cleaning on various surfaces. *Advanced Materials*, **2013**. 25(32): 4477-4481.

158. Barthwal, S., Lee, B., and Lim, S.-H., Fabrication of robust and durable slippery anti-icing coating on textured superhydrophobic aluminum surfaces with infused silicone oil. *Applied Surface Science*, **2019**. 496: 143677.

159. Yeong, Y.H., Wang, C., Wynne, K.J., et al., Oil-infused superhydrophobic silicone material for low ice adhesion with long-term infusion stability. *ACS Applied Materials & Interfaces*, **2016**. 8(46): 32050-32059.

160. Keiser, A., Keiser, L., Clanet, C., et al., Drop friction on liquid-infused materials. *Soft Matter*, **2017**. 13(39): 6981-6987.

161. Gao, A., Liu, J., Ye, L., et al., Control of droplet evaporation on oil-coated surfaces for the synthesis of asymmetric supraparticles. *Langmuir*, **2019**. 35(43): 14042-14048.
162. Manna, U. and Lynn, D.M., Fabrication of liquid-infused surfaces using reactive polymer multilayers: Principles for manipulating the behaviors and mobilities of aqueous fluids on slippery liquid interfaces. *Advanced Materials*, **2015**. 27(19): 3007-3012.
163. Awad, T.S., Asker, D., and Hatton, B.D., Food-safe modification of stainless steel food-processing surfaces to reduce bacterial biofilms. *ACS Applied Materials & Interfaces*, **2018**. 10(27): 22902-22912.
164. Manabe, K., Kyung, K.-H., and Shiratori, S., Biocompatible slippery fluid-infused films composed of chitosan and alginate via layer-by-layer self-assembly and their antithrombogenicity. *ACS Applied Materials & Interfaces*, **2015**. 7(8): 4763-4771.
165. Wu, D., Ma, L., Zhang, F., et al., Durable deicing lubricant-infused surface with photothermally switchable hydrophobic/slippery property. *Materials & Design*, **2020**. 185: 108236.
166. Mukherjee, R., Habibi, M., Rashed, Z.T., et al., Oil-impregnated hydrocarbon-based polymer films. *Scientific Reports*, **2018**. 8(1): 11698.
167. Wang, D., Guo, Z., and Liu, W., Bioinspired edible lubricant-infused surface with liquid residue reduction properties. *Research*, **2019**. 2019.
168. Leslie, D.C., Waterhouse, A., Berthet, J.B., et al., A bioinspired omniphobic surface coating on medical devices prevents thrombosis and biofouling. *Nature Biotechnology*, **2014**. 32(11): 1134-1140.
169. Badv, M., Jaffer, I.H., Weitz, J.I., et al., An omniphobic lubricant-infused coating produced by chemical vapor deposition of hydrophobic organosilanes attenuates clotting on catheter surfaces. *Scientific reports*, **2017**. 7(1): 11639.
170. Zhang, C., Xia, Y., Zhang, H., et al., Surface functionalization for a nontextured liquid-infused surface with enhanced lifetime. *ACS Applied Materials & Interfaces*, **2018**. 10(6): 5892-5901.
171. Tenjimbayashi, M., Togasawa, R., Manabe, K., et al., Liquid-infused smooth coating with transparency, super-durability, and extraordinary hydrophobicity. *Advanced Functional Materials*, **2016**. 26(37): 6693-6702.
172. Togasawa, R., Tenjimbayashi, M., Matsubayashi, T., et al., A fluorine-free slippery surface with hot water repellency and improved stability against boiling. *ACS Applied Materials & Interfaces*, **2018**. 10(4): 4198-4205.
173. Manabe, K., Nakano, M., Hibi, Y., et al., Self-supplying liquidity oil-adsorbed slippery smooth surface for both liquid and solid repellency. *Advanced Materials Interfaces*, **2020**. 7(3): 1901818.

174. Chen, L., Park, S., Yoo, J., et al., One-step fabrication of universal slippery lubricated surfaces. *Advanced Materials Interfaces*, **2020**. 7(18): 2000305.
175. Subramanyam, S.B., Rykaczewski, K., and Varanasi, K.K., Ice adhesion on lubricant-impregnated textured surfaces. *Langmuir*, **2013**. 29(44): 13414-13418.
176. Liu, Z. and Preston, D.J., Enhanced condensation for improved energy efficiency. *Joule*, **2019**. 3(5): 1182-1184.
177. Smith, C.A. and Corripio, A.B., Principles and practices of automatic process control. **2005**: John Wiley & Sons.
178. Hung, T.C., Shai, T.Y., and Wang, S.K., A review of organic rankine cycles (ORCs) for the recovery of low-grade waste heat. *Energy*, **1997**. 22(7): 661-667.
179. Preston, D.J., Lu, Z., Song, Y., et al., Heat transfer enhancement during water and hydrocarbon condensation on lubricant infused surfaces. *Scientific Reports*, **2018**. 8(1): 540.
180. Sett, S., Sokalski, P., Boyina, K., et al., Stable dropwise condensation of ethanol and hexane on rationally designed ultrascalable nanostructured lubricant-infused surfaces. *Nano letters*, **2019**. 19(8): 5287-5296.
181. Chen, L., Huang, S., Ras, R.H.A., et al., Omniphobic liquid-like surfaces. *Nature Reviews Chemistry*, **2023**. 7(2): 123-137.
182. Wooh, S., Encinas, N., Vollmer, D., et al., Stable hydrophobic metal-oxide photocatalysts via grafting polydimethylsiloxane brush. *Advanced Materials*, **2017**. 29(16): 1604637.
183. Wooh, S. and Butt, H.-J., A photocatalytically active lubricant-impregnated surface. *Angewandte Chemie International Edition*, **2017**. 56(18): 4965-4969.
184. Teisala, H., Baumli, P., Weber, S.A.L., et al., Grafting silicone at room temperature-a transparent, scratch-resistant nonstick molecular coating. *Langmuir*, **2020**. 36(16): 4416-4431.
185. Sheparovych, R., Motornov, M., and Minko, S., Adapting low-adhesive thin films from mixed polymer brushes. *Langmuir*, **2008**. 24(24): 13828-13832.
186. Yu, M., Liu, M., Hou, Y., et al., Covalently grafted liquids for transparent and omniphobic surfaces via thiol-ene click chemistry. *Journal of Materials Science*, **2020**. 55(27): 12811-12825.
187. Liu, P., Zhang, H., He, W., et al., Development of “liquid-like” copolymer nanocoatings for reactive oil-repellent surface. *ACS Nano*, **2017**. 11(2): 2248-2256.
188. Liu, J., Sun, Y., Zhou, X., et al., One-step synthesis of a durable and liquid-repellent poly(dimethylsiloxane) coating. *Advanced Materials*, **2021**. 33(23): e2100237.
189. Zhao, X., Khandoker, M.A.R., and Golovin, K., Non-fluorinated omniphobic paper with ultralow contact angle hysteresis. *ACS Applied Materials & Interfaces*, **2020**. 12(13): 15748-15756.

190. Zhang, L., Guo, Z., Sarma, J., et al., Passive removal of highly wetting liquids and ice on quasi-liquid surfaces*. ACS Applied Materials & Interfaces*, **2020**. 12(17): 20084-20095.
191. Khatir, B., Shabanian, S., and Golovin, K., Design and high-resolution characterization of silicon wafer-like omniphobic liquid layers applicable to any substrate*. ACS Applied Materials & Interfaces*, **2020**. 12(28): 31933-31939.
192. Wang, Y., Yan, W., Frey, M., et al., Liquid-like SiO_2-g-PDMS coatings on wood surfaces with underwater durability, antifouling, antismudge, and self-healing properties*. Advanced Sustainable Systems*, **2019**. 3(1): 1800070.
193. Wang, L. and McCarthy, T.J., Covalently attached liquids: instant omniphobic surfaces with unprecedented repellency*. Angewandte Chemie International Edition*, **2016**. 55(1): 244-248.
194. Cheng, D.F., Urata, C., Masheder, B., et al., A physical approach to specifically improve the mobility of alkane liquid drops*. Journal of the American Chemical Society*, **2012**. 134(24): 10191-9.
195. Rabnawaz, M., Liu, G., and Hu, H., Fluorine-free anti-smudge polyurethane coatings*. Angewandte Chemie*, **2015**. 127(43): 12913-12918.
196. Hu, H., Liu, G., and Wang, J., Clear and durable epoxy coatings that exhibit dynamic omniphobicity*. Advanced Materials Interfaces*, **2016**. 3(14): 1600001.
197. Gao, P., Wang, Y., Wang, J., et al., Rational design of durable anti-fouling coatings with high transparency, hardness, and flexibility*. ACS Applied Materials & Interfaces*, **2022**. 14(25): 29156-29166.
198. Zhong, X., Lv, L., Hu, H., et al., Bio-based coatings with liquid repellency for various applications*. Chemical Engineering Journal*, **2020**. 382: 123042.
199. Yang, C., Wu, Q., Zhong, L., et al., Liquid-like polymer-based self-cleaning coating for effective prevention of liquid foods contaminations*. Journal of Colloid and Interface Science*, **2021**. 589: 327-335.
200. Zheng, C., Liu, G., and Hu, H., UV-curable antismudge coatings*. ACS Applied Materials & Interfaces*, **2017**. 9(30): 25623-25630.
201. Lei, L., Buddingh, J., Wang, J., et al., Transparent omniphobic polyurethane coatings containing partially acetylated β–cyclodextrin as the polyol*. Chemical Engineering Journal*, **2020**. 380: 122554.
202. Fazle Rabbi, K., Ho, J.Y., Yan, X., et al., Polydimethylsiloxane-silane synergy enables dropwise condensation of low surface tension liquids*. Advanced Functional Materials*, **2022**. 32(19): 2112837.

203. Zhang, L., Guo, Z., Sarma, J., et al., Gradient quasi-liquid surface enabled self-propulsion of highly wetting liquids*. Advanced Functional Materials*, **2021**. 31(13): 2008614.
204. Soltani, M. and Golovin, K., Lossless, passive transportation of low surface tension liquids induced by patterned omniphobic liquidlike polymer brushes*. Advanced Functional Materials*, **2022**. 32(1): 2107465.
205. Wu, Q., Yang, C., Su, C., et al., Slippery liquid-attached surface for robust biofouling resistance*. ACS Biomaterials Science & Engineering*, **2020**. 6(1): 358-366.
206. Zhao, X., Khatir, B., Mirshahidi, K., et al., Macroscopic evidence of the liquidlike nature of nanoscale polydimethylsiloxane brushes*. ACS Nano*, **2021**. 15(8): 13559-13567.
207. Zhao, H., Deshpande, C.A., Li, L., et al., Extreme antiscaling performance of slippery omniphobic covalently attached liquids*. ACS Applied Materials & Interfaces*, **2020**. 12(10): 12054-12067.
208. Chen, Y., Yu, X., Chen, L., et al., Dynamic poly(dimethylsiloxane) brush coating shows even better antiscaling capability than the low-surface-energy fluorocarbon counterpart*. Environmental Science & Technology*, **2021**. 55(13): 8839-8847.
209. Li, S., Hou, Y., Kappl, M., et al., Vapor lubrication for reducing water and ice adhesion on poly(dimethylsiloxane) brushes*. Advanced Materials*, **2022**. 34(34): 2203242.
210. Wang, X., Zeng, J., Li, J., et al., Beetle and cactus-inspired surface endows continuous and directional droplet jumping for efficient water harvesting*. Journal of Materials Chemistry A*, **2021**. 9(3): 1507-1516.
211. Hou, Y., Yu, M., Chen, X.W., Zuankai , et al., Recurrent filmwise and dropwise condensation on a beetle mimetic surface*. ACS Nano*, **2015**. 9(1): 71-87.
212. Donati, M., Lam, C.W.E., Milionis, A., et al., Sprayable thin and robust carbon nanofiber composite coating for extreme jumping dropwise condensation performance*. Advanced Materials Interfaces*, **2020**. 8(1): 2001176.
213. Wong, W.S.Y., Hegner, K.I., Donadei, V., et al., Capillary balancing: designing frost-resistant lubricant-infused surfaces*. Nano letters*, **2020**. 20(12): 8508-8515.
214. Irajizad, P., Hasnain, M., Farokhnia, N., et al., Magnetic slippery extreme icephobic surfaces*. Nature Communications*, **2016**. 7: 13395.
215. Bormashenko, E.Y., Wetting of real surfaces. *Gruyter Studies in Mathematical Physics*. **2013**: De Gruyter.
216. Li, X., Yang, J., Lv, K., et al., Salvinia-like slippery surface with stable and mobile water/air contact line*. National Science Review*, **2021**. 8(5): nwaa153.
217. Quéré, D., Non-sticking drops*. Reports on Progress in Physics*, **2005**. 68(11): 2495-2532.

218. Laney, S.K., Michalska, M., Li, T., et al., Delayed lubricant depletion of slippery liquid infused porous surfaces using precision nanostructures*. Langmuir*, **2021**. 37(33): 10071-10078.
219. Adera, S., Alvarenga, J., Shneidman, A.V., et al., Depletion of lubricant from nanostructured oil-infused surfaces by pendant condensate droplets*. ACS Nano*, **2020**. 14(7): 8024-8035.
220. Deloche, B., Beltzung, M., and Herz, J., Segmental order in a uniaxially constrained polydimethylsiloxane network : a deuterium magnetic resonance study*. Journal de Physique Lettres*, **1982**. 43(22): 763-769.
221. Krushev, S., Paul, W., and Smith, G.D., The role of internal rotational barriers in polymer melt chain dynamics*. Macromolecules*, **2002**. 35(10): 4198-4203.
222. Huang, G.-S., Li, Q., and Jiang, L.-X., Structure and damping properties of polydimethylsiloxane and polymethacrylate sequential interpenetrating polymer networks*. Journal of Applied Polymer Science*, **2002**. 85(3): 545-551.
223. Daniel, D., Timonen, J.V.I., Li, R., et al., Origins of extreme liquid repellency on structured, flat, and lubricated hydrophobic surfaces*. Physical Review Letters*, **2018**. 120(24): 244503.
224. Buzágh, A. and Wolfram, E., Bestimmung der Haftfähigkeit von Flüssigkeiten an festen Körpern mit der Abreißwinkelmethode. II*. Kolloid-Zeitschrift*, **1958**. 157(1): 50-53.
225. Neuburger, N. and Eichinger, B., Critical experimental test of the Flory-Rehner theory of swelling*. Macromolecules*, **1988**. 21(10): 3060-3070.
226. Barnette, A.L., Asay, D.B., Kim, D., et al., Experimental and density functional theory study of the tribochemical wear behavior of SiO_2 in humid and alcohol vapor environments*. Langmuir*, **2009**. 25(22): 13052-13061.
227. Barthel, A.J. and Kim, S.H., Lubrication by physisorbed molecules in equilibrium with vapor at ambient condition: Effects of molecular structure and substrate chemistry*. Langmuir*, **2014**. 30(22): 6469-6478.
228. Nguyen, N.N., Berger, R., Kappl, M., et al., Clathrate adhesion induced by quasi-liquid layer*. The Journal of Physical Chemistry C*, **2021**. 125(38): 21293-21300.
229. Mukherjee, R., Berrier, A.S., Murphy, K.R., et al., How surface orientation affects jumping-droplet condensation*. Joule*, **2019**. 3(5): 1360-1376.
230. Lee, J.N., Park, C., and Whitesides, G.M., Solvent compatibility of poly(dimethylsiloxane)-based microfluidic devices*. Analytical Chemistry*, **2003**. 75(23): 6544-6554.
231. Popescu, M.N., Oshanin, G., Dietrich, S., et al., Precursor films in wetting phenomena*. Journal of Physics: Condensed Matter*, **2012**. 24(24): 243102.
232. Chaudhury, M.K. and Whitesides, G.M., Correlation between surface free energy and surface constitution*. Science*, **1992**. 255(5049): 1230-1232.

233. Butt, H.-J., Cappella, B., and Kappl, M., Force measurements with the atomic force microscope: Technique, interpretation and applications. *Surface Science Reports*, **2005**. 59(1-6): 1-152.

234. Zheng, L., Li, H., Huang, W., et al., Light stimuli-responsive superhydrophobic films for electric switches and water-droplet manipulation. *ACS Applied Materials & Interfaces*, **2021**. 13(30): 36621-36631.

235. Nasirimarekani, V., Benito-Lopez, F., and Basabe-Desmonts, L., Tunable superparamagnetic ring (tspring) for droplet manipulation. *Advanced Functional Materials*, **2021**. 31(32): 2100178.

236. Chen, J., Liu, J., He, M., et al., Superhydrophobic surfaces cannot reduce ice adhesion. *Applied Physics Letters*, **2012**. 101(11): 111603.

237. Meuler, A.J., Smith, J.D., Varanasi, K.K., et al., Relationships between Water Wettability and Ice Adhesion. *ACS Applied Materials & Interfaces*, **2010**. 2(11): 3100-3110.

238. Li, S. and Butt, H.-J., Organic vapors influence water contact angles on hydrophobic surfaces. *Advanced Materials*, **2023**: 2301905.

239. Laplace, P.S., Traité de mécanique céleste/par PS Laplace...; tome premier [-quatrieme]. Vol. IV. **1805**, Paris: de l'Imprimerie de Crapelet.

240. Boyd, G. and Livingston, H., Adsorption and the energy changes1 at crystalline solid surfaces. *Journal of the American Chemical Society*, **1942**. 64(10): 2383-2388.

241. Good, R.J., A thermodynamic derivation of wenzel's modification of young's equation for contact angles; together with a theory of Hysteresis1. *Journal of the American Chemical Society*, **1952**. 74(20): 5041-5042.

242. Shuttleworth, R. and Bailey, G., The spreading of a liquid over a rough solid. *Discussions of the Faraday Society*, **1948**. 3: 16-22.

243. Huh, C. and Mason, S., Effects of surface roughness on wetting (theoretical). *Journal of colloid and interface science*, **1977**. 60(1): 11-38.

244. Joanny, J. and De Gennes, P.-G., A model for contact angle hysteresis. *The Journal Of Chemical Physics*, **1984**. 81(1): 552-562.

245. Gilles de Gennes, P., Brochard, P., and Quéré, D., Capillarity and wetting phenomena: drops, bubbles, pearls, waves. **2004**, New York: Springer.

246. Ward, C.A. and Wu, J., Effect of adsorption on the surface tensions of solid−fluid interfaces. *The Journal of Physical Chemistry B*, **2007**. 111(14): 3685-3694.

247. Yekta-Fard, M. and Ponter, A.B., The influences of vapor environment and temperature on the contact angle-drop size relationship*. Journal of Colloid and Interface Science*, **1988**. 126(1): 134-140.

248. Kamusewitz, H., Possart, W., and Paul, D., Measurements of solid-water contact angles in the presence of different vapours*. International Journal of Adhesion and Adhesives*, **1993**. 13(4): 243-249.

249. Fainerman, V.B., Aksenenko, E.V., Kovalchuk, V.I., et al., Surface tension of water and C10EO8 solutions at the interface to hexane vapor saturated air*. Colloids and Surfaces A: Physicochemical and Engineering Aspects*, **2016**. 505: 118-123.

250. Kairaliyeva, T., Fainerman, V.B., Aksenenko, E.V., et al., Adsorption of alkane vapor at water drop surfaces*. Colloids and Surfaces A: Physicochemical and Engineering Aspects*, **2017**. 532: 541-547.

251. Mucic, N., Moradi, N., Javadi, A., et al., Effect of partial vapor pressure on the co-adsorption of surfactants and hexane at the water/hexane vapor interface*. Colloids and Surfaces A: Physicochemical and Engineering Aspects*, **2015**. 480: 79-84.

252. Streitberger, H.-J. and Goldschmidt, A., BASF handbook basics of coating technology. **2018**: European Coatings.

253. Xu, W., Zheng, H., Liu, Y., et al., A droplet-based electricity generator with high instantaneous power density*. Nature*, **2020**. 578(7795): 392-396.

254. Zheng, Y., Bai, H., Huang, Z., et al., Directional water collection on wetted spider silk*. Nature*, **2010**. 463(7281): 640-3.

255. Butt, H.-J., Berger, R., Steffen, W., et al., Adaptive wetting—adaptation in wetting*. Langmuir*, **2018**. 34(38): 11292-11304.

256. Frenkel, Y.I., On the behavior of liquid drops on a solid surface. 1. The sliding of drops on an inclined surface*. arXiv preprint physics/0503051*, **2005**.

257. Ritsema van Eck, G.C., Kiens, E.M., Veldscholte, L.B., et al., Vapor swelling of polymer brushes compared to nongrafted films*. Langmuir*, **2022**. 38(45): 13763-13770.

258. Pethica, B.A. and Glasser, M.L., Lateral intermolecular forces in the physisorbed state: Surface field polarization of benzene and n-hexane at the water/ and mercury/vapor interfaces*. Langmuir*, **2005**. 21(3): 944-949.

259. Kwon, O.-S., Jing, H., Shin, K., et al., Formation of n-alkane layers at the vapor/water interface*. Langmuir*, **2007**. 23(24): 12249-12253.

260. Javadi, A., Moradi, N., Möhwald, H., et al., Adsorption of alkanes from the vapour phase on water drops measured by drop profile analysis tensiometry*. Soft Matter*, **2010**. 6(19): 4710-4714.

261. Li, X., Bista, P., Stetten, A.Z., et al., Spontaneous charging affects the motion of sliding drops. *Nature Physics*, **2022**. 18(6): 713–719.

262. Yang, Y., Miller, D.J., and Hawthorne, S.B., Toluene solubility in water and organic partitioning from gasoline and diesel fuel into water at elevated temperatures and pressures. *Journal of Chemical & Engineering Data*, **1997**. 42(5): 908-913.

263. Verschueren, K., Handbook of environmental data on organic chemicals: Vol. 1. **2001**, New York: John Wiley and Sons, Inc.

264. Poulson, S., Harrington, R., and Drever, J., The solubility of toluene in aqueous salt solutions. *Talanta*, **1999**. 48(3): 633-641.

265. McAuliffe, C., Solubility in water of paraffin, cycloparaffin, olefin, acetylene, cycloolefin, and aromatic hydrocarbons1. *The Journal of Physical Chemistry*, **1966**. 70(4): 1267-1275.

266. Berry, J.D., Neeson, M.J., Dagastine, R.R., et al., Measurement of surface and interfacial tension using pendant drop tensiometry. *Journal of Colloid and Interface Science*, **2015**. 454: 226-237.

267. Stauffer, C.E., The measurement of surface tension by the pendant drop technique. *The journal of physical chemistry*, **1965**. 69(6): 1933-1938.

268. Daubert, T.E., Physical and thermodynamic properties of pure chemicals: data compilation. *Design Institute for Physacal Property Data (DIPPR)*. **1989**: AIChE.

269. Mantanis, G.I. and Young, R.A., Wetting of wood. *Wood Science and Technology*, **1997**. 31(5): 339-353.

270. Lide, D.R., CRC handbook of chemistry and physics. Vol. 85. **2004**: CRC press.

271. Hansen, C.M., Hansen solubility parameters: a user's handbook. **2007**: CRC press.

272. Liu, H., Zhang, P., Liu, M., et al., Organogel-based thin films for self-cleaning on various surfaces. *Advanced Materials*, **2013**. 25(32): 4477-4481.

273. Sukitpaneenit, P. and Chung, T.-S., Molecular elucidation of morphology and mechanical properties of PVDF hollow fiber membranes from aspects of phase inversion, crystallization, and rheology, *in Hollow Fiber Membranes*. **2021**, Elsevier. 333-360.

274. Su, Q., Zhang, J., and Zhang, L.-Z., Fouling resistance improvement with a new superhydrophobic electrospun PVDF membrane for seawater desalination. *Desalination*, **2020**. 476: 114246.

275. Zhang, W., Zhang, Y., Lu, C., et al., Aerogels from crosslinked cellulose nano/micro-fibrils and their fast shape recovery property in water. *Journal of Materials Chemistry*, **2012**. 22(23): 11642-11650.

276. Machui, F., Langner, S., Zhu, X., et al., Determination of the P3HT: PCBM solubility parameters via a binary solvent gradient method: Impact of solubility on the photovoltaic performance*. Solar Energy Materials and Solar Cells*, **2012**. 100: 138-146.
277. Scott, R.L., The solubility of fluorocarbons1. *Journal of the American Chemical Society*, **1948**. 70(12): 4090-4093.
278. Shi, S., Cui, X., Han, H., et al., A study of the heat transfer performance of a pulsating heat pipe with ethanol-based mixtures*. Applied Thermal Engineering*, **2016**. 102: 1219-1227.
279. Su, Q., Chang, S., Song, M., et al., An experimental study on the heat transfer performance of a loop heat pipe system with ethanol-water mixture as working fluid for aircraft anti-icing*. International Journal of Heat and Mass Transfer*, **2019**. 139: 280-292.
280. Wang, T., Sheng, C., and Nnanna, A.G.A., Experimental investigation of air conditioning system using evaporative cooling condenser*. Energy and Buildings*, **2014**. 81: 435-443.
281. Jin, H., Lin, G., Bai, L., et al., Steam generation in a nanoparticle-based solar receiver*. Nano Energy*, **2016**. 28: 397-406.
282. Sharma, C.S., Stamatopoulos, C., Suter, R., et al., Rationally 3D-textured copper surfaces for laplace pressure imbalance-induced enhancement in dropwise condensation*. ACS Applied Materials & Interfaces*, **2018**. 10(34): 29127-29135.
283. Chen, X., Wu, J., Ma, R., et al., Nanograssed micropyramidal architectures for continuous dropwise condensation*. Advanced Functional Materials*, **2011**. 21(24): 4617-4623.
284. Zhang, N., Innovative heat pipe systems using a new working fluid*. International Communications in Heat and Mass Transfer*, **2001**. 28(8): 1025-1033.
285. Taft, B.S., Williams, A.D., and Drolen, B.L., Review of pulsating heat pipe working fluid selection*. Journal of Thermophysics and Heat Transfer*, **2012**. 26(4): 651-656.
286. Srimuang, W. and Amatachaya, P., A review of the applications of heat pipe heat exchangers for heat recovery*. Renewable and Sustainable Energy Reviews*, **2012**. 16(6): 4303-4315.
287. Rettig, A., Lagler, M., Lamare, T., et al. Application of organic rankine cycles (ORC). in *World Engineers' Convention*. **2011**. Geneva.
288. Lion, S., Michos, C.N., Vlaskos, I., et al., A review of waste heat recovery and organic rankine cycles (ORC) in on-off highway vehicle heavy duty diesel engine applications*. Renewable and Sustainable Energy Reviews*, **2017**. 79: 691-708.
289. Xiao, R., Miljkovic, N., Enright, R., et al., Immersion condensation on oil-infused heterogeneous surfaces for enhanced heat transfer*. Scientific Reports*, **2013**. 3: 1988.
290. Khalil, K., Soto, D., Farnham, T., et al., Grafted nanofilms promote dropwise condensation of low-surface-tension fluids for high-performance heat exchangers*. Joule*, **2019**. 3(5): 1377-1388.

291. Wyslouzil, B.E. and Wolk, J., Overview: Homogeneous nucleation from the vapor phase-The experimental science. *The Journal of Chemical Physics*, **2016**. 145(21): 211702.
292. Turnbull, D., Kinetics of heterogeneous nucleation. *The Journal of Chemical Physics*, **1950**. 18(2): 198-203.
293. Hou, Y., Butt, H.J., and Kappl, M., Water and ice nucleation on solid surfaces, *in Ice Adhesion*. **2020**. 55-85.
294. Gao, N., Geyer, F., Pilat, D.W., et al., How drops start sliding over solid surfaces. *Nature Physics*, **2017**. 14(2): 191-196.
295. Extrand, C.W. and Gent, A.N., Retention of liquid drops by solid surfaces. *Journal of Colloid and Interface Science*, **1990**. 138(2): 431-442.
296. Brown, R.A., Orr, F.M., and Scriven, L.E., Static drop on an inclined plate: Analysis by the finite element method. *Journal of Colloid and Interface Science*, **1980**. 73(1): 76-87.
297. Cha, H., Vahabi, H., Wu, A., et al., Dropwise condensation on solid hydrophilic surfaces. *Science Advances*, **2020**. 6(2): eaax0746.
298. Cheng, Y., Wang, M., Sun, J., et al., Rapid and persistent suction condensation on hydrophilic surfaces for high-efficiency water collection. *Nano Letters*, **2021**. 21(17): 7411-7418.
299. Beysens, D. and Knobler, C.M., Growth of breath figures. *Physical Review Letters*, **1986**. 57(12): 1433-1436.
300. Sharma, C.S., Combe, J., Giger, M., et al., Growth rates and spontaneous navigation of condensate droplets through randomly structured textures. *ACS Nano*, **2017**. 11(2): 1673-1682.
301. Boreyko, J.B. and Chen, C.-H., Self-propelled dropwise condensate on superhydrophobic surfaces. *Physical Review Letters*, **2009**. 103(18): 184501.
302. Miljkovic, N., Enright, R., and Wang, E.N., Effect of droplet morphology on growth dynamics and heat transfer during condensation on superhydrophobic nanostructured surfaces. *ACS Nano*, **2012**. 6(2): 1776-1785.
303. Wen, R., Li, Q., Wu, J., et al., Hydrophobic copper nanowires for enhancing condensation heat transfer. *Nano Energy*, **2017**. 33: 177-183.
304. Wen, R., Xu, S., Zhao, D., et al., Sustaining enhanced condensation on hierarchical mesh-covered surfaces. *National Science Review*, **2018**. 5(6): 878-887.
305. Stylianou, S.A. and Rose, J.W., Drop-to-filmwise condensation transition: Heat transfer measurements for ethanediol. *International Journal of Heat and Mass Transfer*, **1983**. 26(5): 747-760.
306. Rose, J.W., On the mechanism of dropwise condensation. *International Journal of Heat and Mass Transfer*, **1967**. 10(6): 755-762.

307. Narhe, R., Beysens, D., and Nikolayev, V.S., Contact line dynamics in drop coalescence and spreading*. Langmuir*, **2004**. 20(4): 1213-1221.
308. Kapur, N. and Gaskell, P.H., Morphology and dynamics of droplet coalescence on a surface*. Physical review E: Statistical, nonlinear, and soft matter physics*, **2007**. 75(5): 056315.
309. Eddi, A., Winkels, K.G., and Snoeijer, J.H., Influence of droplet geometry on the coalescence of low viscosity drops*. Physical Review Letters*, **2013**. 111(14): 144502.
310. Sharma, C.S., Lam, C.W.E., Milionis, A., et al., Self-sustained cascading coalescence in surface condensation*. ACS Applied Materials & Interfaces*, **2019**. 11(30): 27435-27442.
311. Chu, F., Yan, X., and Miljkovic, N., How superhydrophobic grooves drive single-droplet jumping*. Langmuir*, **2022**. 38(14): 4452-4460.
312. Zhao, G., Zou, G., Wang, W., et al., Competing effects between condensation and self-removal of water droplets determine antifrosting performance of superhydrophobic surfaces*. ACS Applied Materials & Interfaces*, **2020**. 12(6): 7805-7814.
313. Liu, C., Zhao, M., Zheng, Y., et al., Enhancement and guidance of coalescence-induced jumping of droplets on superhydrophobic surfaces with a U-groove*. ACS Applied Materials & Interfaces*, **2021**. 13(27): 32542-32554.
314. Ma, J., Sett, S., Cha, H., et al., Recent developments, challenges, and pathways to stable dropwise condensation: A perspective*. Applied Physics Letters*, **2020**. 116(26): 260501.
315. S.S.Sadhal, W.W.M., Heat transfer through drop condensate using differential inequalitiesTransfert thermique par condensation en gouttes en utilisant des inegalites differentielles*. International Journal of Heat and Mass Transfer*, **1977**. 20(12): 1401-1407.
316. O'Neill, G.A. and Westwater, J.W., Dropwise condensation of steam on electroplated silver surfaces*. International Journal of Heat and Mass Transfer*, **1984**. 27(9): 1539-1549.
317. Li, S., Bista, P., Weber, S.A.L., et al., Spontaneous charging of drops on lubricant-infused surfaces*. Langmuir*, **2022**. 38(41): 12610-12616.
318. Yatsuzuka, K., Mizuno, Y., and Asano, K., Electrification phenomena of pure water droplets dripping and sliding on a polymer surface*. Journal of Electrostatics*, **1994**. 32(2): 157-171.
319. Helseth, L.E. and Guo, X.D., Contact electrification and energy harvesting using periodically contacted and squeezed water droplets*. Langmuir*, **2015**. 31(10): 3269-3276.
320. Stetten, A.Z., Golovko, D.S., Weber, S.A.L., et al., Slide electrification: charging of surfaces by moving water drops*. Soft Matter*, **2019**. 15(43): 8667-8679.
321. Helseth, L.E., A water droplet-powered sensor based on charge transfer to a flow-through front surface electrode*. Nano Energy*, **2020**. 73: 104809.

322. Lin, S., Chen, X., and Wang, Z.L., Contact electrification at the liquid-solid interface. *Chemical Reviews*, **2022**. 122(5): 5209-5232.

323. Kudin, K.N. and Car, R., Why are water−hydrophobic interfaces charged? *Journal of the American Chemical Society*, **2008**. 130(12): 3915-3919.

324. Zimmermann, R., Rein, N., and Werner, C., Water ion adsorption dominates charging at nonpolar polymer surfaces in multivalent electrolytes. *Physical Chemistry Chemical Physics*, **2009**. 11(21): 4360-4364.

325. McCarty, L.S. and Whitesides, G.M., Electrostatic charging due to separation of ions at interfaces: Contact electrification of ionic electrets. *Angewandte Chemie International Edition*, **2008**. 47(12): 2188-2207.

326. Huang, L.-B., Xu, W., Zhao, C., et al., Multifunctional water drop energy harvesting and human motion sensor based on flexible dual-mode nanogenerator incorporated with polymer nanotubes. *ACS Applied Materials & Interfaces*, **2020**. 12(21): 24030-24038.

327. Jin, Y., Xu, W., Zhang, H., et al., Electrostatic tweezer for droplet manipulation. *Proceedings of the National Academy of Sciences*, **2022**. 119(2): e2105459119.

328. Xu, W., Zhou, X., Hao, C., et al., SLIPS-TENG: robust triboelectric nanogenerator with optical and charge transparency using a slippery interface. *National Science Review*, **2019**. 6(3): 540-550.

329. Lowell, J. and Rose-Innes, A.C., Contact electrification. *Advances in Physics*, **1980**. 29(6): 947-1023.

330. Wang, Z.L. and Wang, A.C., On the origin of contact-electrification. *Materials Today*, **2019**. 30: 34-51.

331. Baytekin, H.T., Patashinski, A.Z., Branicki, M., et al., The mosaic of surface charge in contact electrification. *Science*, **2011**. 333(6040): 308-312.

332. Sharma, C.S., Milionis, A., Naga, A., et al., Enhanced condensation on soft materials through bulk lubricant infusion. *Advanced Functional Materials*, **2021**. 32(17): 2109633.

333. Chen, L., Geissler, A., Bonaccurso, E., et al., Transparent slippery surfaces made with sustainable porous cellulose lauroyl ester films. *ACS Applied Materials & Interfaces*, **2014**. 6(9): 6969-6976.

334. Peppou-Chapman, S. and Neto, C., Depletion of the lubricant from lubricant-infused surfaces due to an air/water interface. *Langmuir*, **2021**. 37(10): 3025-3037.

335. Mammen, L., Bley, K., Papadopoulos, P., et al., Functional superhydrophobic surfaces made of Janus micropillars. *Soft Matter*, **2015**. 11(3): 506-515.

336. Hauer, L., Wong, W.S.Y., Donadei, V., et al., How frost forms and grows on lubricated micro- and nanostructured surfaces*. ACS Nano*, **2021**. 15(3): 4658-4668.
337. McHale, G., Orme, B.V., Wells, G.G., et al., Apparent contact angles on lubricant-impregnated surfaces/slips: From superhydrophobicity to electrowetting*. Langmuir*, **2019**. 35(11): 4197-4204.
338. Antonini, C., Carmona, F.J., Pierce, E., et al., General methodology for evaluating the adhesion force of drops and bubbles on solid surfaces*. Langmuir*, **2009**. 25(11): 6143-6154.
339. Wong, W.S.Y., Bista, P., Li, X., et al., Tuning the charge of sliding water drops*. Langmuir*, **2022**. 38(19): 6224-6230.
340. Li, J., Li, W., Tang, X., et al., Lubricant-mediated strong droplet adhesion on lubricant-impregnated surfaces*. Langmuir*, **2021**. 37(28): 8607-8615.
341. Keiser, A., Baumli, P., Vollmer, D., et al., Universality of friction laws on liquid-infused materials*. Physical Review Fluids*, **2020**. 5(1): 014005.
342. Straub, B.B., Schmidt, H., Rostami, P., et al., Flow profiles near receding three-phase contact lines: influence of surfactants*. Soft Matter*, **2021**. 17(44): 10090-10100.

Curriculum Vitae

Shuai Li

Isaac-Fulda-Allee 4A, 55122 Mainz

Tel: +49 (0)15153200463

E-mail: lis2@mpip-mainz.mpg.de

geboren am 28.04.1994

in Shijiazhuang, China

Bildungsweg

Seit 09/2019	*PhD* student in Chemistry
	Max Planck Institute for Polymer Research, Mainz, Germany.
09/2012—07/2016	*M.Eng* in Materials Engineering
	Beijing University of Chemical Technology, Beijing, P.R.China
09/2008—07/2012	*B.Eng*. in Polymer Materials Science and Engineering
	Beijing Technology and Business University, Beijing, P.R.China.

Wissenschaftliche Beiträge

S. Li, Y. Hou, M. Kappl, W. Steffen, J. Liu, H-J. Butt. Vapor lubrication for reducing water and ice adhesion on poly (dimethylsiloxane) brushes. Advanced Materials, 2022: 2203242.

S. Li, H-J. Butt. Organic vapors influence water contact angles on hydrophobic surfaces. Advanced Materials, 2023: 2301905.

S. Li, D. Diaz, M. Kappl, H-J. Butt, J. Liu, Y. Hou. Enhanced condensation heat transfer by water/ethanol binary liquids on polydimethylsiloxane brushes. Droplet, 2022: 1, 214.

S. Li, P. Bista, SAL. Weber, M. Kappl, H-J. Butt. Spontaneous charging of drops on lubricant-infused surfaces. Langmuir, 2022: 2c02085.

J. Song, J. Liu, M. Li, S. Li, M. Kappl, H-J. Butt, Y. Hou, and K-L. Yeung. Hierarchically Branched Siloxane Brushes for Efficient Harvesting of Atmospheric Water. Small, 2023. 2301561.

S. Li, J. Zhang, J. Chen, M. Yao, X. Liu, Z. Jiang. Biodegradable body temperature responsive shape memory polyurethanes with self-healing behavior. Polymer Engineering & Science, 2019: 59, E310.

S. Li, J. Zhang, J. Chen, M. Yao, X. Liu, Z. Jiang. Self-healing polycarbonate-based polyurethane with shape memory behavior. Macromolecular research, 2019: 27, 649.